Common Envelope: The Dynamical Aspects

by

José Luis Avendaño Nandez

A thesis submitted in partial fulfillment of the requirements for the degree of

Doctor of Philosophy

Department of Physics
University of Alberta

Abstract

Interactions between stars are crucial for diverse areas of astrophysics, but they are not yet fully understood. These interactions come in forms as diverse as a direct physical collision, matter transfer from one star to another, and a "common envelope" (CE). The CE phase is a short period of time when the two stellar cores share their outer layers. During a CE phase, the rotating binary shrinks its orbit by transferring the orbital angular momentum and mechanical energy of the stars to the envelope. Depending on the amount of energy deposited in the envelope, the CE phase will lead to either ejection of the envelope and formation of a tight binary or, by merging the binary to form a single, rapidly-rotating star.

During a CE phase, various physical processes take place, each operating on a different time-scale. In this work I consider events occurring on the dynamical time scale of the system and employ smoothed particle hydrodynamics (SPH) to simulate the interactions. This class of numerical methods is a natural choice for simulating interacting binaries without imposing boundary conditions. Compared to grid based codes, SPH also has the advantage of conserving energy and angular momentum of the system during the CE.

Previously, it was expected that during a CE event, the binary will not strongly boost its luminosity compared to its pre-CE state. Combined with the short duration of the event, and the expected CE rates, it was thought that a CE event would not likely ever be observed. However, the recent discovery of a new type of object, the so called Luminous Red Novae (LRNe), gave us an insight that the CE events have already been observed. We proposed that instead of just boosted surface luminosity, a CE event will be accompanied by an outburst powered by a recombination wave in the ejected material, similar to Type II supernovae. The luminosity and the duration of this CE outburst depend on the mass and velocity of the ejected material. This model allows us to match all observed characteristics of LRN light curves. We tested this idea by

modelling in detail the recent transient event, V1309 Sco, famous for being identified as a binary merger.

We continued a detailed study of the outburst of V1309 Sco, reproducing its merger while aiming to constrain the initial conditions. In particular, we attempted to find out whether the companion star was a low-mass main sequence star or a low-mass white dwarf, and whether the subgiant was synchronized with the orbit. We found that the observed orbital period decay of V1309 Sco could be reproduced by a synchronized subgiant donor with a low-mass main sequence star companion.

The formation of a double white dwarf (DWD) binary system is widely accepted to require two mass exchanges, the latter of which has to be a CE event between a low-mass red giant and the first-formed white dwarf. Low-mass red giants have a well-defined relationship between their core masses and radii, which provides the tightest theoretical constraint on the orbital separations prior to a CE event. Not surprisingly, there have been several attempts to model the latter mass exchange with hydrodynamic methods. However, all these attempts have failed to fully eject the envelope of the red giant . Although it has been acknowledged in the past that recombination energy of atoms could help CE ejection, it was unclear whether recombination takes place while this energy can still be used to drive the ejection. We incorporated in our SPH code the equation of state that includes recombination, and found that the red giant's envelope is fully ejected when we take into account recombination. We applied our method to model the system WD 1101+364. We found that for DWD systems, synchronization at the start of the CE event does not play a role. We also discussed the modified energy budget formalism.

Preface

Some of the research conducted for this thesis was done as a part of an international research collaboration, led by Professor Natalia Ivanova at the University of Alberta. The 3D hydrodynamics simulations and their analysis referred in Chapter 2 were done by myself. The simulations and the analytical tools presented in Chapter 3 and Chapter 4 are my original work.

Chapter 2 of this thesis has been published as N. Ivanova, S. Justham; J. L. Avendano Nandez, and J. C. Lombardi Jr., "The identification of long-sought Common-Envelope events," *Science*, vol. 339, issue 6118, 433-435 (2013). I was responsible for the design and conduct of the 3D simulations, analysis of their outcomes as well as production of some graphs for the manuscript. N. Ivanova was the leading author who developed the proposed concept and was the primary author responsible for the manuscript. S. Justham participate in the concept development. J. C. Lombardi Jr. contributed to the analysis of the 3D simulations. All the authors contributed to the manuscript edits.

Chapter 3 of this thesis has been published as J. L. A. Nandez, N. Ivanova, and J. C. Lombardi Jr., "V1309 Sco – Understanding a merger," The Astrophysical Journal, vol. 786, issue 1, article id. 39, 20 pp. (2014). J. C. Lombardi Jr. helped with the analysis of the 3D simulations and contributed to the manuscript editing. N. Ivanova advised with the detailed analysis and the manuscript editing. I made all the analysis and composed the manuscript.

Chapter 4 of this thesis has been published as J. L. A. Nandez, N. Ivanova, and J. C. Lombardi Jr., "Recombination energy in double white dwarf formation," Monthly Notice of the Royal Astronomical Society Letters, vol. 450, issue 1, L39-L43 (2015). J. C. Lombardi Jr. helped with the analysis of the 3D simulations and contributed to the manuscript editing. N. Ivanova advised with the detailed analysis and the manuscript editing. I made all the analysis and composed the manuscript.

Dedications

To Amelia Antonio Tolentino†, my grandmother
To Eva Nandez Antonio, my mother
To Citlalli Avendaño Nandez, my sister
To Jorge Avendaño Nandez, my brother
who are my inspiration and have believed in me.

Acknowledgements

I would like to express my gratitude to my supervisor, Prof. Natalia Ivanova, whose expertise, understanding, patience, and advice added considerably to my graduate experience. I appreciate her knowledge and skills in writing articles, ethics, and interaction with colleagues, which have helped me to improve my writing and communication skills. I would like to thank Prof. James Lombardi for all his comments and useful discussion throughout my whole program. I believe that his expertise was crucial for the developing of this Thesis.

I would like to thank the other members of my committee, Prof. Craig Heinke, Prof. Gregory Sivakoff and Prof. Sharon Morsink for their advice at all levels of my research project. My sincere thanks also goes to the external examiners, Prof. Alison Sills and Prof. Erik Rosolowsky, who gave me useful comments for the improvement of this Thesis.

I would also like to thank my family for their support and in particular, I must acknowledge my best friend and partner Erika, whose love encouraged me to keep going.

I recognize that this research would not have been possible without the financial assistance of the pairing between the *Consejo Nacional de Ciencia y Tecnología, Mexico* and the University of Alberta in the UofAlberta-CONACyT fellowship. I also thank the Department of Physics at the University of Alberta for extra support through the Graduate Teaching and Research Assistantships. Finally, this research was enabled by the use of computing resources provided by WestGrid, SHARCNET and Compute/Calcul Canada.

Table of Contents

List of Tables

List of Figures

Chapter 1

Introduction

Herschel (1802) was one of the first to study and catalog hundreds of visual pairs of stars. He was the first to propose a primitive way to study their orbits, and to realize that the double stars were actually two stars, orbiting around their common center of mass, where Newton's laws applied. Despite the fact that binary systems have been observed for over 200 years, we still lack a comprehensive model for the evolution of binary stellar systems, and even more so for systems of a higher multiplicity, such as tripe systems, or quadruple systems. We know that there are binaries that are so far from each other that they only interact gravitationally. However, if the two stars are close enough to each other, the so called *close binary system*, mass transfer occurs in the course of their evolution.

Kuiper (1941) was the first to recognize the importance of the shape of the effective potential in close binary systems for their evolution. The effective potential in a binary system forms a Roche lobe, which is the region around a star where the material is gravitationally bound to the corresponding star. The mathematical definition of the Roche lobe starts by obtaining the effective gravitational potential of a static particle in the rotating frame, assuming a circular orbit, and a constant angular velocity of the binary,

$$\phi_{\rm eff}(x,y,z) = -\frac{Gm_1}{\sqrt{[x+(m_2/m)a]^2+y^2+z^2}} - \frac{Gm_2}{\sqrt{[x-(m_1/m)a]^2+y^2+z^2}} - \frac{Gm}{2a^3}(x^2+y^2), \qquad (1.1)$$

where G is the gravitational constant, m_1, m_2, and $m = m_1 + m_2$ are the masses of the more massive, less massive, and binary star, respectively. a is the orbital separation, whilst (x,y,z) is a point in the Cartesian coordinate. The centres of mass of the star 1 and star 2 are located at $-(m_2/m)a$, and $(m_1/m)a$, respectfully.

The boundary of the Roche lobe is defined by the critical gravitational equipotential at the inner Lagrangian point L_1 where $\nabla\phi_{\rm eff}(x_{L_1},0,0) \equiv 0$ and x_{L_1} is in the range between $-(m_2/m)a$

and $(m_1/m)a$. Figure 1.1 shows the Roche lobe for a binary composed of $1.4M_\odot$ donor star and $0.32M_\odot$ accretor star with a separation of $60R_\odot$. In this work, we refer to a star as the *donor* if it has filled up its Roche lobe, and as the *accretor* if the star is contained within its Roche Lobe and may accrete material from the donor. Note that rotation of the binary affects the size of Roche lobe in *xy*-plane versus *xz*-plane: the Roche lobe in the *xy*-plane is about 10% and 7% bigger for the donor and accretor, respectively, than their lobes in the *xz*-plane due to the rotation of the binary.

We emphasize that if one star starts filling its Roche lobe then some material can flow through L_1 into the Roche lobe of the other star since the mechanical force at this point is 0. This physical process is called *Roche lobe overflow* (RLOF), and it is the most fundamental way of how mass is transferred from one star to the other.

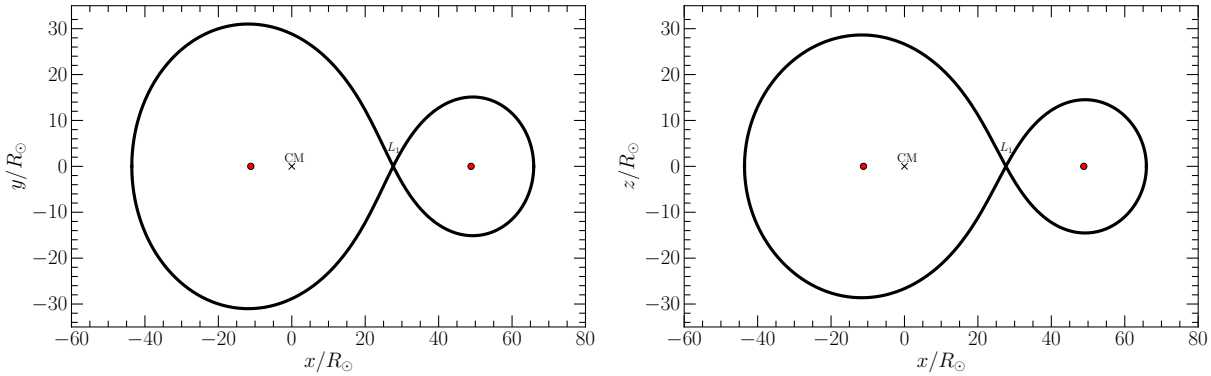

Figure 1.1: Roche lobe in *xy* plane (left panel) and in the *xz* plane (right panel) for a masses of $m_1 = 1.4M_\odot$ and $m_2 = 0.32M_\odot$ with a separation of $60R_\odot$. Solid line shows where the equipotential has the same value as at the L_1 point, the centre of mass of the binary is marked as CM and solid dots show the centres of mass for each stars.

Kopal (1955) classified the close binary systems into three groups, based on how the radii of the stars compare to their Roche lobe radii:

i) Detached Systems — both stars under-fill their Roche lobes, and no mass transfer via RLOF can occur. See the top panel in Figure 1.2.

ii) Semi-detached Systems — only one component fills its Roche lobe, and mass transfer occurs via RLOF. See the middle panel in Figure 1.2.

iii) Contact Systems — both components fill their Roche lobes. The stars are in contact at the inner Lagrangian point L_1, and they may exchange mass at this point. We point out that the mass transfer in these systems is stable. See the bottom panel in Figure 1.2.

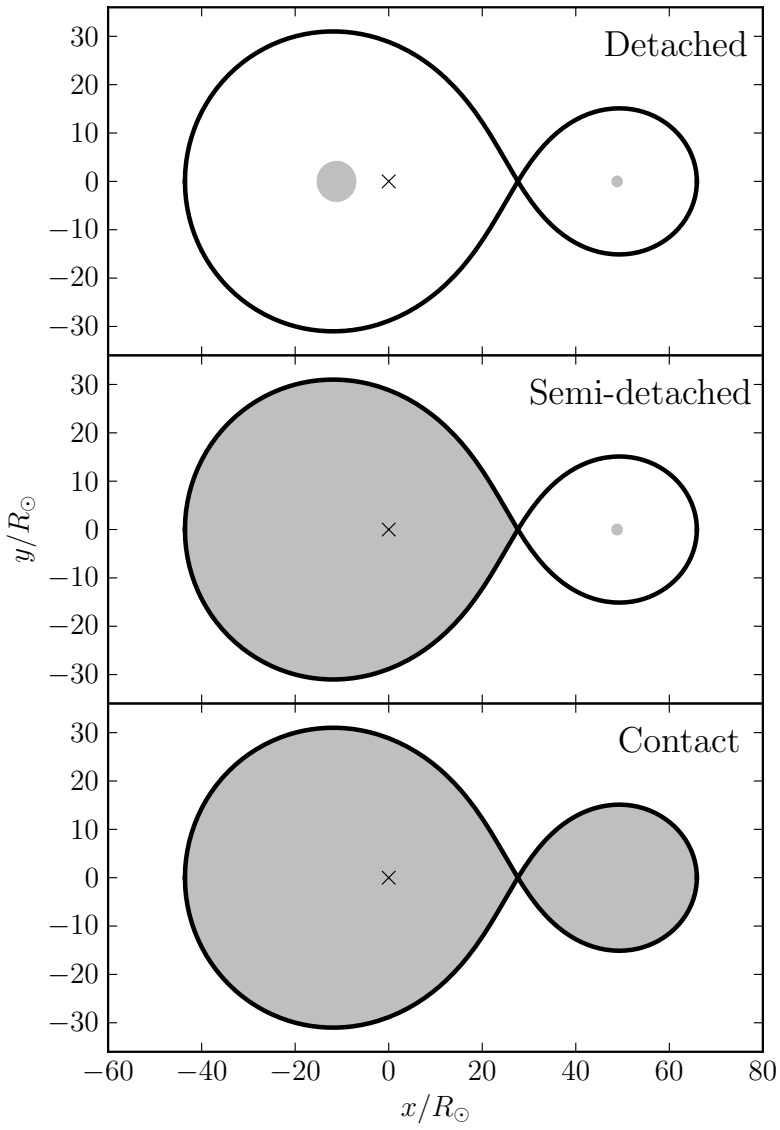

Figure 1.2: The three possible close binary systems, detached (top panel), semi-detached (middle panel), and contact (bottom panel). The Roche lobe corresponds to a $1.4\,M_\odot$ donor (on the left) and $0.32\,M_\odot$ accretor (on the right) in the xy-plane for an orbital separation of $60\,R_\odot$. The crosses indicate the locations of the centre of mass of the binary on each panel.

Now, we can consider the case when the material of a contact binary expands beyond its Roche lobe. The material outside the Roche lobes of both stars remains gravitationally bound to the binary. First, the material would remain within the equipotential that is defined by the outer Lagrangian point L_2. L_2 is defined as $\nabla\phi(x_{L_2},0,0) \equiv 0$ where x_{L_2} is located on the $x-$axis, in the direction of the less-massive star, and is outside of that less-massive star. In this case, the two stars are rotating within a single-shared envelope. Figure 1.3 shows such a common envelope contained within the

L_2 equipotential. If the material keeps expanding, the binary will start losing mass through L_2. Depending on the specific angular momentum and velocity at L_2, this material can remain bound to the binary (and, e.g., fill the equipotential defined by L_3 point, which is similar to L_2 but is located outside of the more-massive companion), or it can leave the binary, changing the binary irreversibly.

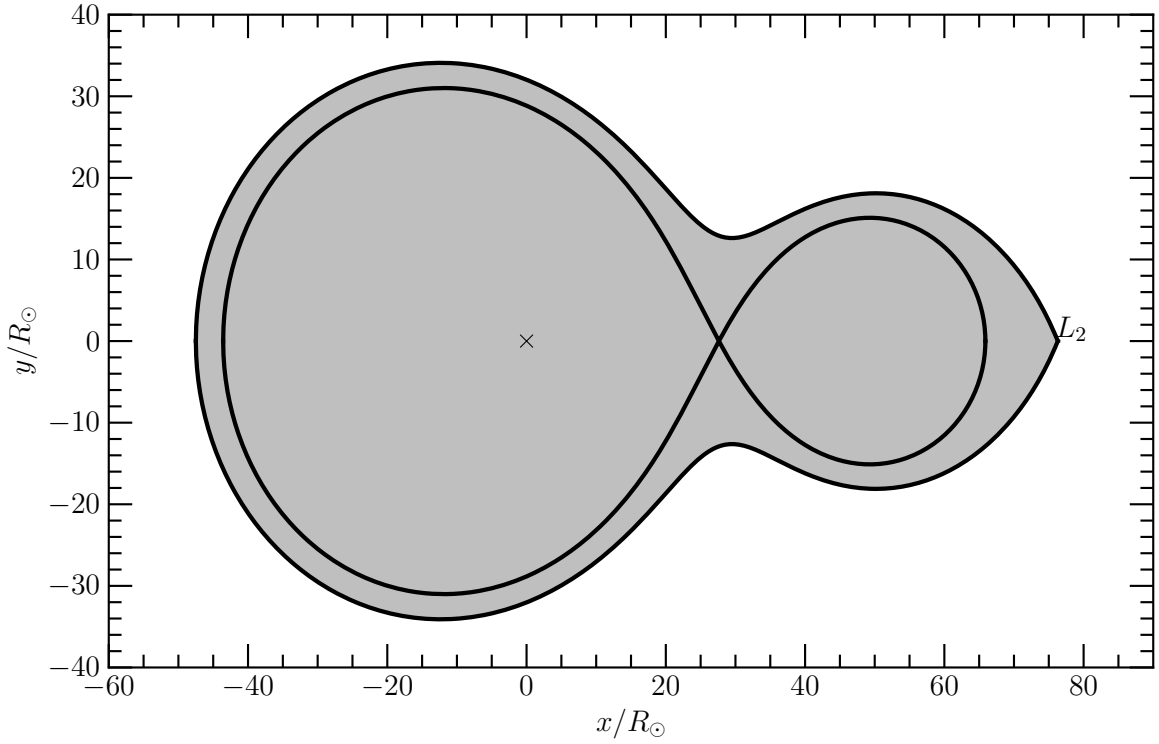

Figure 1.3: The gravitationally bound material within the outer equipotential, defined by the outer Lagrangian point L_2 for a $1.4\,M_\odot$ donor (on the left) and $0.32\,M_\odot$ accretor (on the right) with orbital separation of $60\,R_\odot$ in the equatorial plane.

The physical process described in the previous paragraph was named the common envelope event (CEE), which was first introduced by Paczynski (1976) who had made reference to a private communication with Ostriker in the same year, he also referenced Webbink (1975). Currently, the definition of the CEE is as follows: a short-lived period in the evolution of a binary when the two stars orbit inside of their common envelope (CE). When the two stars orbit inside of their CE, drag forces acts between the CE and the stellar cores, transporting orbital angular momentum and orbital energy from the binary to the envelope. This reduces the binary orbital separation, and if the timescale of the orbital shrinkage is comparable to the orbital period, the process is called *spiral-in*. If the envelope takes in enough orbital energy and orbital angular momentum, the CE gets ejected,

and the system ends up as a binary that is likely more compact than the progenitor binary. However, if the CE does not receive enough energy, a merger between the two stars occurs. We point out that the border line that defines the outcome of a CEE – a merger or a close binary – is still uncertain, see Ivanova et al. (2013b).

Importance of the CEE. The spiral-in process in a CE and the following envelope ejection is the main mechanism by which an initially wide binary is converted into a very close binary or by which two stars merge. Therefore, our understanding of this stellar evolutionary phase forms the foundation of our understanding of the formation of a vast type of close binaries such as the progenitors of Type Ia supernovae (originally two white dwarfs that have merged, or a binary consisting of a white dwarf and a non-degenerate star), X-ray binaries (a binary system that contains one stellar-mass black hole or neutron star as the accreting companion), double degenerate stars (a binary system that only contains white dwarfs, neutron stars, or black holes), and cataclysmic variable stars (a binary system where the white dwarf is the accreting companion).

Despite being crucially important for a vast number of important binary systems, CEE theory is not yet at the level where we can find the CEE outcome for every binary system. Indeed, CEE and the related stellar-hydrodynamic processes arguably constitute the most important unsolved problems in stellar evolution, and are certainly the least-well-constrained processes in binary evolution.

The main problem with the CEE is that it is affected by distinct physical processes acting at different timescales. This complexity is the reason why a complete treatment of the problem does not yet exist.

CEE phases. Podsiadlowski (2001) suggested that it is possible to split the overall CEE problem into individual sub-problems that may be simpler to treat. The sub-problems are as follows:

1.- *The initial phase; loss of corotation*. This is the phase during which the initially stable close binary is transformed into a spiralling-in binary.

This transformation can occur if the donor has reached its Roche lobe, but the initiated mass transfer is dynamically unstable (runaway), either at the start of RLOF or later. For example, if the reaction of the donor on the mass loss is to expand relative to its Roche lobe.

A CEE may also be established due to the Darwin instability (Darwin, 1879). It is possible that the donor and accretor stars are in corotation with the orbit such that both stars are tidally locked to the orbit. When the donor star expands (due to evolution), but it is still contained within its Roche lobe, a stable binary is no longer possible if the orbital angular momentum

is less than or equal to three times the spin angular momentum of the two stars, hence, the two stars plunge into each other.

The initial phase could last from a few dynamical time-scales up to the thermal time-scale of the donor depending on the mass transfer history of the binary before the possible onset of the dynamical instability.

2.- *The plunge-in phase*. Once corotation between the orbit and the donor star is broken, a swift spiral-in phase begins. In this phase, the friction between the stars and the CE generates frictional energy that is deposited in the CE and drives the expansion of the envelope. This stage is fast (dynamical time-scale), lasting between days to a few years. Podsiadlowski (2001) showed that energy transport is not really important during this phase, hence, this stage can be safely modelled with hydrodynamical calculations. If enough energy is deposited to the CE, the stage is terminated by CE dynamical ejection. Otherwise, either a dynamical merge of the two stars occurs, or the next CE phase takes place (see below).

3.- *Self-regulating spiral-in*. If the second phase does not succeed to eject the CE and only expands it significantly, then the spiral-in slows down to a stage where the frictional energy, built-up during the spiral-in phase, can be radiated away at the surface of the CE (see Meyer & Meyer-Hofmeister, 1979; Podsiadlowski, 2001).

It is not yet clear whether this stage can be formed. If it does, then this stage would operate on the thermal time-scale of the envelope.

4.- *Termination of the self-regulating phase*. The self-regulating phase would finish with the ejection of the CE, or when one of the stars overfills its Roche lobe. The latter mass transfer can lead to a dynamical merger of the spiralling-in companion and the core of the donor, or lead to their slow merger (see Ivanova & Podsiadlowski, 2002).

Ivanova et al. (2013b) pointed out that the self-regulated spiral-in phase could be followed by another plunge-in phase if the mechanism supporting the self-regulation suddenly stops. Hence, the plunge-in could be followed by another self-regulating phase and so on.

5.- *Post-CE*. The final orbital parameters would not be in equilibrium after sometime. For instance, the eccentricity of the binary can be changed whilst the shrunken binary finds its equilibrium. The expanding ejected material will attain a terminal velocity after the CEE making the expelled matter expand at the same rate. Hence, a final shape of the planetary nebula could be seen when the outcome is not a merger. In addition, the radius of the merged star could change due to the thermal relaxation of the newly formed star.

Description of the CEE. The standard way to describe the CEE follows the *energy formalism* (Webbink, 1984; Livio & Soker, 1988), in which the orbital energy before and after the event, $\Delta E_{\rm orb}$, is compared with the energy required to eject the envelope to infinity, $E_{\rm bind}$, which has been assumed to be the sum of the potential energy of the envelope and its internal energy without recombination energy. The mathematical description is as follows,

$$E_{\rm bind} = \Delta E_{\rm orb} = E_{\rm orb,ini} - E_{\rm orb,fin} = -\frac{G m_1 m_2}{2 a_{\rm ini}} + \frac{G m_{1,\rm c} m_2}{2 a_{\rm fin}}, \tag{1.2}$$

where m_1, m_2, and $m_{1,\rm c}$ are the mass of the donor, accretor, and final mass of the star that lost its envelope, respectively. G is the gravitational constant, whilst $a_{\rm ini}$ and $a_{\rm fin}$ are the initial and final orbital separation, respectfully.

The binding energy of the envelope, $E_{\rm bind}$, is a more complicated quantity, since it involves the internal energy of the envelope and its gravitational energy. Webbink (1984) introduced this quantity by integrating the gravitational energy combined with the internal energy (without recombination energy) of all the material in the envelope. He introduced a gravitational parametrization of the binding energy instead of using the whole integral,

$$E_{\rm bind} = \frac{G m_1 m_{1,\rm env}}{R_1}, \tag{1.3}$$

where $m_{1,\rm env}$ is the envelope mass of the primary star, and R_1 is its radius. The energy formalism then is written as

$$\frac{m_1 m_{1,\rm env}}{R_1} = -\frac{m_1 m_2}{2 a_{\rm ini}} + \frac{m_{1,\rm c} m_2}{2 a_{\rm fin}}. \tag{1.4}$$

This equation can be used to link the final and the initial orbital binary separation, provided that all the masses are known, as well as the initial radius of the primary star.

Livio & Soker (1988) pointed out that not all available orbital energy can be used for ejecting the envelope, since there are more physical processes happening during the spiral-in. They introduced an efficiency parameter $\alpha_{\rm CE}$,

$$\alpha_{\rm CE} = \frac{E_{\rm bind}}{\Delta E_{\rm orb}}. \tag{1.5}$$

Livio & Soker (1988) argued that the value for $\alpha_{\rm CE}$ should be about 0.3, since they could better explain certain objects, such as Type Ia supernovae in our Galaxy. However, they also realized that this value would not explain Type Ia supernovae in elliptical galaxies.

We note that the binding energy calculated with equation (1.3) is an order of magnitude estimate. Since $E_{\rm bind}$ depends on the detailed structure of the primary's envelope, de Kool (1990) introduced an additional factor λ to account for differences in the envelope structures,

$$E_{\rm bind} = \frac{G m_1 m_{1,\rm env}}{\lambda R_1}. \tag{1.6}$$

Currently the most used energy formalism is by combining equations (1.2), (1.5) and (1.6),

$$\frac{Gm_1 m_{1,\mathrm{env}}}{\lambda R_1} = \alpha_{\mathrm{CE}} \left(-\frac{Gm_1 m_2}{2a_{\mathrm{ini}}} + \frac{Gm_{1,\mathrm{c}} m_2}{2a_{\mathrm{fin}}} \right). \tag{1.7}$$

Note that this formulation allows us to join the two parameters into a single one, $\alpha_{\mathrm{CE}}\lambda$. There are different definitions for λ depending on the problem being treated and the author. Ivanova et al. (2013b) presents a more detailed review about the usage of this parameter.

γ-formalism. The angular momentum, when compared between the binary before the CEE, and the formed post-CEE binary together with the ejected material, should be conserved. Paczyński & Ziółkowski (1967) studied the influence of mass loss on the evolution of a close binary system. They proposed a simple way to characterize the rate of angular momentum loss, defined by a parameter γ[1], as follows:

$$\gamma = \frac{J_{\mathrm{ini}} - J_{\mathrm{fin}}}{\Delta M} \frac{M_{\mathrm{tot}}}{J_{\mathrm{ini}}}, \tag{1.8}$$

where J_{ini} and J_{fin} are the initial and final angular momentum, respectfully. ΔM and M_{tot} are the mass loss and initial mass of the binary, respectively.

More recently, Nelemans et al. (2000) applied this method to the CEE. They found that the CEE outcome can be predicted as follows,

$$\frac{P_{\mathrm{fin}}}{P_{\mathrm{ini}}} = \left(\frac{m_1 m_2}{m_1' m_2'} \right)^3 \left(\frac{m_1' + m_2'}{m_1 + m_2} \right) \left(1 - \gamma \frac{\Delta M}{m_1 + m_2} \right), \tag{1.9}$$

where m_1' and m_2' are the new masses for the primary and secondary, respectively, and P_{fin} and P_{ini} are the final and initial orbital period, respectfully. This method assumes circular binaries before and after the CEE. This formalism has been used in different studies as an alternative to the energy formalism.

In this Thesis, we focus on the dynamical interactions between giants and their more compact companions. Therefore, we have analyzed phase 2 of the CEE, the only phase that operates on a dynamical time-scale of the system.

Objectives. The general objectives of this project are the study of several events or processes during the common-envelope event, where each of them occurs on a dynamical timescale and therefore can be studied by means of a hydrodynamics-three-dimensional code. In particular, we focus on:

[1]Note that the original paper uses g instead of γ.

(i) initial start of the dynamical mass transfer, to understand the role of the tidal interactions and initial corotation;

(ii) energy budget during the dynamical phase, to understand how much of the excess energy is carried away; and

(iii) the role of the recombination energy in the energy budget, to understand how the system is affected by including or not this energy.

Methodology. The best numerical method to simulate interacting binaries without imposing boundary conditions is smoothed particle hydrodynamics (SPH), a Lagrangian method introduced by Lucy (1977) and Gingold & Monaghan (1977). For a review of this method, see Monaghan & Lattanzio (1985) and, more recently, Rosswog (2009), or see the Appendix A for an introduction of the method. The specific code that we have been using for this research is a three-dimensional (3D) SPH code called `StarCrash`, which was developed by Lombardi et al. (2006). The code was updated to run fully parallelized with an integration of a GPU library by Gaburov et al. (2010). The GPU integration computes the $N-$body problem faster than a conventional CPU algorithm. The updated code was described in Lombardi et al. (2011) (the current name of the code is `StarSmasher`). This code has been already used numerous times to study dynamical interactions between the stars [e.g., Ivanova et al. (2005), Gaburov et al. (2010), Antonini et al. (2011)].

The SPH technique is not the only method that could model the CEEs. There is at least another technique that could model them, the Eulerian grid-based technique. The difference between these two techniques is clear, one works on a Lagrangian frame while the other on a Eulerian frame. SPH method is better for tracing the ejected mass of the binary, while the Eulerian grid-based code is better for modelling low-mass flows. For a more detail comparison of these methods, see Boyarchuk et al. (2002) or Ivanova et al. (2013b).

We use SPH-based code `StarSmasher` to model binary interaction between giants and compact companions. In order to use `StarSmasher` for specific stars, it is necessary to have an initial profile of the giant. We use the `TWIN/STARS` stellar code (recent updates described in Glebbeek et al., 2008) to set our initial profile of the stars. The profile is imported in `StarSmasher` in a *relaxation* process that converts the 1D stellar profile to a 3D SPH profile. In the relaxation process, SPH particles are places on a hexagonal close packed lattice with particles extending out to a distance only a few smoothing lengths less than the full stellar radius. After the initial particle parameters have been assigned according to the stellar profile, we allow the SPH particles to evolve into hydrostatic equilibrium by damping the velocity terms.

Afterwards we place this new 3D SPH profile in a binary configuration, where the compact companion is modelled as a point mass (unless specified otherwise), a special particle in SPH that only interacts gravitationally.

The computational resources required to fully resolve one simulation, composed of 100000 particles with at least 10 million iterations, are 4 CPU-year (6-core Intel E5649 with 2 sockets each) and 1 GPU-year (NVIDIA Tesla M2070s) running at the same time. The total allocation time necessary to solve the problems presented in this Thesis was 143.19 CPU-year and 30.91 GPU-year using Compute/Calcul Canada mainly on the Parallel system from WestGrid.

This work began as an investigation into the potential observable characteristics of the CEE. The CEE are short-lived events, and it was predicted that there is a little chance to observe them because of their duration. It was also speculated that they did not release enough energy in the event to be well-distinguished from observations at large distances, so as a result we might not detect them. Nonetheless, a CEE is expected to be accompanied by a rise in luminosity that could be observationally identified as a transient [2] event.

In particular, the objects observationally classified as intermediate luminosity red transients, also called luminous red novae, or intermediate luminosity optical transients, could potentially have undergone a CEE. These objects have luminosities between novae and supernovae, $\sim 10^{45}$ – 10^{47} erg. It is interesting that during their outburst the source is "cold", producing most of its spectra in the "red" visual spectra band. The energy involved in producing these events is comparable to the expected release of the orbital energy during a CEE, which is, by an order of magnitude, similar to the binding energy of the envelope of a giant star.

In Chapter 2 we present a theoretical model that could explain the luminosities and duration of these transient events. We give the physical process – recombination – that is responsible to create the observed outbursts. In order to study the outburst of one particular object, V1309 Sco, we carried out numerical simulations. Based on the results of these simulations and on the proposed theoretical model of the outburst, we reconstructed the light-curve of the V1309 Sco event.

A more detail discussion about the CEE event for V1309 Sco is presented in Chapter 3, where the goal of the study is to constrain the nature of the pre-CE binary and low-mass companion. In that Chapter, we assume that the progenitor of V1309 Sco was a subgiant star with a mass of $1.52\,M_{\odot}$ and a companion star of $0.16\,M_{\odot}$ with an orbital period of ~ 1.44 days. We consider two types of the companion, a main sequence and a degenerate star. The latter is treated as a point mass

[2] A transient event is a short-lived burst of energy in an astronomical object which occurs likely because the object suddenly changes.

in our model, whilst the main sequence star, as well as the subgiant star (in both cases), were treated with gas particles. We varied the initial synchronization of the binary from non-synchronized to fully synchronized. We discussed the possible physical mechanism that could trigger the beginning of the CEE (described as phase 1 above). While considering this particular object, we created numerical tools to study and analyze any dynamical timescale CEE. In particular, these tools can be used to describe when the CEE starts and when it terminates. We also compare qualitatively the orbital period decay of our models with the observations. The final appearance of the object during its post-CE phase is also compared with observations in Chapter 3. We give the possible progenitor for V1309 Sco based on the model that best matches the observations.

The CEE treated in Chapter 2 and 3 leads to stellar mergers. In Chapter 4 we modelled CEEs that lead to the formation of a double white dwarf binary system. Here, the two stars do not merge and produce a new binary in a very tight orbit, as compared to their initial orbital separation. For this study, we consider the last episode of the mass transfer in the pre-CE binary that would have been composed of a giant with the previously formed white dwarf. Observationally, this latter white dwarf would be identified as the older one, in the system that consist of the two white dwarfs. Since the mass of the initial giant is not known, we investigated a parameter space for the mass of the giant ranging between 1.0 to $1.8 M_{\odot}$. We use two equations of state to model the double white dwarf formation: (i) the standard equation of state, which includes ideal gas and radiation contributions, and (ii) a tabulated equation of state, which has contributions of ideal gas, radiation, and recombination energy. The inclusion of the recombination is critically important, as this is essentially an additional consideration of a new physical process. This led to a qualitative change of the CE outcome, when compared to the previously performed hydrodynamical studies of the CEE. We also compare non-synchronized and synchronized binaries. We applied our numerical method to the well-known double white dwarf, WD 1101+364. We present a modified version of equation 1.7, where we include new terms for the recombination energy and for the energy carried away by the ejected material. We give the possible values for α and λ for the classical energy formalism. In addition, we calculate the values for γ [see equation (1.8)]. We predict the progenitor for WD 1101+364 based on the post-CE orbital parameters.

Chapter 2

Identification of the Long-Sought Common-Envelope Events

N. Ivanova,[1,*] S. Justham,[2] J. L. Avendano Nandez,[1] J. C. Lombardi Jr.[3]

[1]Department of Physics, University of Alberta, Edmonton, AB T6G 2E7, Canada. [2]National Astronomical Observatories, The Chinese Academy of Sciences, Beijing 100012, China. [3]Department of Physics, Allegheny College, Meadville, PA 16335, USA.

*To whom correspondence should be addressed. E-mail: nata.ivanova@ualberta.ca

Published 25 January 2013, *Science* **339**, 433 (2013)
DOI:10.1126/science.1225540

ABSTRACT

Common-envelope events (CEEs), during which two stars temporarily orbit within a shared envelope, are believed to be vital for the formation of a wide range of close binaries. For decades, the only evidence that CEEs actually occur has been indirect, based on the existence of systems that could not be otherwise explained. Here we propose a direct observational signature of CEEs arising from a physical model where emission from matter ejected in a CEE is controlled by a recombination front as the matter cools. The natural range of time scales and energies from this model, as well as the expected colors, light-curve shapes, ejection velocities and event rate, match those of a recently recognized class of red transient outbursts.

Many binary star systems, including X-ray binaries, cataclysmic variables, close double-neutron stars, and the potential progenitors of Type Ia supernovae and short-duration γ-ray bursts, are thought to be formed by common-envelope events (CEEs). Because most stellar-mass binary merger sources for gravitational waves have experienced a CEE in their past, improved knowledge of CEEs should decrease the large uncertainty in theoretically predicted merger rates. However, the short time scale expected for CEEs suggested that we would never directly observe them, allowing us only to draw inferences from the systems produced.

A CEE begins when a binary orbit becomes unstable and decays. This might, for example, be driven purely by tidal forces (i.e., the Darwin instability), although CEEs are more commonly imagined as occurring after a period of rapid mass transfer from one star to the other (Ivanova, 2011). In some cases, the rate of transfer is so high that the receiving star is unable to accrete all the matter without forming a shared common envelope (CE) around the binary. This CE causes drag on one or both stars and hence orbital decay, with orbital energy and angular momentum being transferred to the CE. This may end with a stellar merger or — if the CE is ejected — the binary can survive, typically with a much reduced orbital separation, critical to explaining many observed compact binaries.

When a CEE results in formation of a close binary, it is expected that a substantial proportion of the mass is ejected — typically almost the entire envelope of one of the stars. Some mass can also be ejected in the case of a merger. This partial ejection has two causes (see §2.1). First, the orbital energy deposited into the CE early in the merger may exceed the binding energy of the outer layers. Second, angular momentum transport may be too slow for the angular momentum absorbed by the upper layers of the envelope to be redistributed across the envelope as a whole.

Here we consider the behavior of this ejected matter to try to predict the appearance of CEEs. A situation involving similar physics — type IIP supernovae — has been studied previously (e.g, Chugai, 1991; Popov, 1993; Kasen & Woosley, 2009). In that model, as the ejected stellar plasma expands and cools, recombination changes its opacity, leading to the propagation of a photosphere-defining "cooling wave," which moves inwards with respect to the mass variable.

For smooth and spherically symmetric ejecta distributions, the model light curve will have a plateau shape: The area of the photosphere is defined by recombination, and so the emitting surface does not grow with the speed at which the ejected matter itself moves. During this phase, whereas material ejected by the CEE will expand with velocity of the order of magnitude of the initial escape velocity, the photospheric radius should appear almost constant. The luminosity $L_{\rm P}$ of the emission during the plateau (Chugai, 1991; Popov, 1993; Kasen & Woosley, 2009), re-scaled to the likely energy range of CEE, is

$$L_{\rm P} \approx 1.7 \times 10^4 L_\odot \left(\frac{R_{\rm init}}{3.5\,R_\odot}\right)^{2/3} \left(\frac{E_{\rm k}^\infty}{10^{46}\,{\rm erg}}\right)^{5/6} \left(\frac{m_{\rm unb}}{0.03\,M_\odot}\right)^{-1/2} \left(\frac{\kappa}{0.32\,{\rm cm^2\,g^{-1}}}\right)^{-1/3} \left(\frac{T_{\rm rec}}{4500\,{\rm K}}\right)^{4/3}, \tag{2.1}$$

where $R_{\rm init}$ is the initial radius, $E_{\rm k}^\infty$ is the kinetic energy of the unbound mass $m_{\rm unb}$ at late times after escaping the potential well, κ is the opacity of the ionized ejecta, and $T_{\rm rec}$ is the recombination temperature. The duration of the plateau $t_{\rm P}$ with the same assumptions is

$$t_{\rm P} \approx 17\ {\rm days} \left(\frac{R_{\rm init}}{3.5\,R_\odot}\right)^{1/6} \left(\frac{E_{\rm k}^\infty}{10^{46}\,{\rm erg}}\right)^{-1/6} \left(\frac{m_{\rm unb}}{0.03\,M_\odot}\right)^{1/2} \left(\frac{\kappa}{0.32\,{\rm cm^2\,g^{-1}}}\right)^{1/6} \left(\frac{T_{\rm rec}}{4500\,{\rm K}}\right)^{-2/3}. \tag{2.2}$$

This model does not depend on the origin of the energy released during the outburst. For type IIP supernovae, recombination controls the release of the internal energy generated by strong supernova shocks. For CEEs, however, there is no such supernova-provided energy input. Instead, the energy released by recombination itself may dominate the energy budget of many outbursts (Kasen & Ramirez-Ruiz, 2010). The unbound mass $m_{\rm unb}$ could potentially radiate — simply due to recombination — as much energy as

$$E_{\rm recom} \simeq 2.6 \times 10^{46}\,{\rm ergs}\ (X + 1.5 Y f_{\rm He}) \frac{m_{\rm unb}}{M_\odot}. \tag{2.3}$$

Here X is the mass fraction of hydrogen and Y is the mass fraction of helium. Hydrogen would initially be ionized in almost all of the likely ejected material from most stars; however, helium may be fully ionized only in some fraction of it, denoted $f_{\rm He}$. The role of recombination in a CEE has hitherto been debated in the overall energy balance, the controversy arising from whether it can be effectively converted into mechanical energy to help eject the CE (Iben & Livio, 1993; Han et al., 1994; Webbink, 2008). This energy budget for the outburst may be increased by the thermal energy of the ejecta. Much of the pre-CEE thermal energy of the ejecta may be expended on adiabatic cooling (Kasen & Ramirez-Ruiz, 2010). However, the shock heating caused by the CEE could well be substantial in some cases.

To estimate the extent of the parameter space of CEE outbursts, we use the model described above to predict the diversity of real events. We assume that $E_{\rm k}^\infty$ scales with the gravitational potential at the surface of the primary star (§2.1) and use the dimensionless factor ζ to write $E_{\rm k}^\infty = \zeta(G m_1^2 f_{\rm m})/R_{\rm init}$, where $f_{\rm m} = m_{\rm unb}/m_1$ is the fraction of the total primary mass m_1 that becomes unbound. From Eqs. 2.1 and 2.2, this leads to $L_{\rm P} \propto \left(f_{\rm m}^2 m_1^7 R_{\rm init}^{-1} \zeta^5\right)^{1/6}$ and $t_{\rm P} \propto \left(f_{\rm m}^2 m_1 R_{\rm init}^2 \zeta^{-1}\right)^{1/6}$. Two families of events seem likely, one for mergers (i.e., $f_{\rm m} \ll 1$) and one for CE ejection (i.e., $f_{\rm m} \leq 1$) (Fig. 2.1).

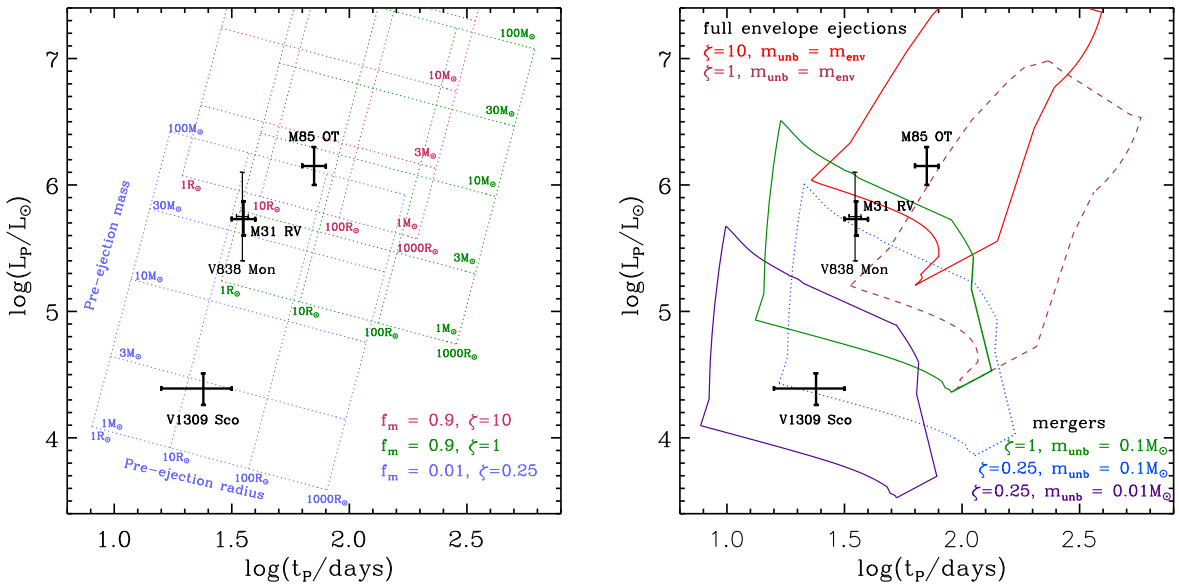

Figure 2.1: **(Left)** Model diversity in the $L_{\rm P}-t_{\rm P}$ parameter space is indicated by lines representing constant primary mass and radius. $f_{\rm m}$ is fractional mass loss and ζ is the kinetic energy at infinity, parametrized as a fraction of the binding energy at the surface of the primary star. Stellar mergers are in a regime of little mass ejection, whereas $f_{\rm m} = 0.9$ approximates full envelope ejection. **(Right)** Estimated ranges of the plateau luminosity $L_{\rm P}$ and duration $t_{\rm P}$ for primary stars with zero-age main sequence (ZAMS) masses from 1 to 150 $M_{\odot}$. $m_{\rm unb}$ is the ejecta mass. It is assumed that mergers can happen anytime during the primary's evolution, whereas full envelope ejection can occur only for post-main-sequence primary stars. We used fitting formulae for stellar evolution (Hurley et al., 2000), at $Z_{\odot}$. In both panels, values for $L_{\rm P}$ and $t_{\rm P}$ are marked for the outbursts from V1309 Sco, M85 OT, M31-RV, and V838 Mon.

In addition to the predicted ranges of outburst energy and duration, this model for CEE outbursts has several noteworthy features. The physics that causes the plateau-shaped light curve should lead to a difference in the photometrically inferred expansion velocity and the actual material velocity (which could be inferred from spectra). The effective photospheric temperature should be $\sim 5000\,$K for thick ejecta (Popov, 1993), and so the outburst color will naturally be red. In addition, once the ejected envelope has fully recombined, the material may suddenly become transparent, unless enough of the ejecta has cooled down sufficiently to produce dust. These characteristics are reminiscent of curious transients with predominantly red spectra that were recently detected in the local universe (e.g., Mould et al., 1990; Martini et al., 1999; Bond et al., 2003; Kulkarni et al., 2007; Pastorello et al., 2007; Bond et al., 2009; Bond, 2011; Kasliwal et al., 2011). This empirical class has been dubbed luminous red novae (LRNe), a subset of the even more ambiguously defined

class of intermediate-luminosity red transients (ILRTs) (§2.1). ILRTs cover a wide range of outburst energies, from 10^{45} to a few 10^{47} ergs (brighter than the brightest novae but still fainter than Type Ia supernovae). They are characterized by spectroscopically inferred expansion velocities of 200-1000 km/s — much lower than would be expected for novae or supernovae and also markedly different from the photometric expansion velocities (Berger et al., 2009). In addition, some could be seen as red giants within a dozen years after the outburst (Bond, 2011; Tylenda et al., 2011).

It was not known what ILRTs are or whether they have a common cause; several ideas have been suggested (§2.1). A model that considered the possibility that LRNe are caused by stellar mergers — a subset of CEEs — has been independently considered several times for different LRN outbursts, though further examinations of outburst features always showed various drawbacks. However, those problematic features do match expectations from our CEE-driven outburst model (§2.1).

A particular feature of the LRN outbursts — as opposed to all ILRTs — is the presence of a plateau in their luminosity curves. We compare well-known LRNe (§2.1) to the expected CEE diversity in Fig. 2.1. The agreement is pronounced, especially given the simplicity of the model and the potential complexities it neglects — e.g., how CEE ejecta deviate from spherical symmetry, or how much ζ for mergers might be different from ζ for full envelope ejection (§2.1).

M85 OT2006-1 is a LRN with well-known peak luminosity and plateau duration. If the luminosity from M85 OT2006-1 was largely from recombination, $\sim 1.5 M_{\odot}$ of plasma would have recombined to provide the observed total energy. This fits with constraints on the progenitor mass ($\leq 2 M_{\odot}$) from the stellar population age (Ofek et al., 2008). Thus, M85 OT2006-1 plausibly ejected the whole envelope of a low-mass giant. This outburst showed a plateau, with luminosity $\approx 1 \times 10^6$ to $2 \times 10^6 L_{\odot}$ (Rau et al., 2007) for ≈60 to 80 days, and had expansion velocities of 350 km/s (Pastorello et al., 2007). Our inferred ejecta mass and that observed expansion velocity indicate a kinetic energy of $\sim 1.8 \times 10^{48}$ erg. Then, $R_{\rm init} = 45 R_{\odot}$, self-consistent with our model, gives $L_P \sim 10^6 L_{\odot}$ and $t_P \sim 70$ days.

Another recent outburst, V1309 Sco, is similar to, but fainter than, most LRNe, as it radiated away only $\sim 3 \times 10^{44}$ erg during a $\sim$ 25-day plateau-shaped maximum in the light-curve (Tylenda et al., 2011). The progenitor was a contact binary with a relatively rapidly decaying orbital period of $\sim$ 1.4 days. After the outburst, the system appeared to be a single star; therefore, this appears to have been a CEE, leading to a merger (Tylenda et al., 2011). However, several features of the V1309 Sco outburst, in particular the plateau in the light curve and sudden transparency, were difficult to reconcile with prior theoretical expectations for the appearance of a CEE (§2.1).

Because the V1309 Sco progenitor was observed in detail, this system is ideal for testing our

model. Beginning with the properties of the premerger contact binary (Stępień, 2011; Tylenda et al., 2011), we calculated the amount of material that became unbound during the V1309 merger using two methods — simple energy balance using a one-dimensional (1D) stellar code and a set of 3D hydrodynamical simulations (§2.1). Both methods predict that a small mass, ~ 0.03 to $0.08\,M_{\odot}$, will become unbound. Complete recombination of this ejected mass would provide enough energy ($\geq 7 \times 10^{44}$ ergs) to explain the total energy output of V1309 Sco. The output of the 3D simulations, combined with Eqs. 2.1 and 2.2, predicts plateau duration from 16 to 25 days, and plateau luminosities of 1.8×10^4 to $2.2 \times 10^4\,L_{\odot}$. These values match the observed luminosity ($L_P \sim 2 \times 10^4\,L_{\odot}$) and plateau duration (about 25 days).

Considering the menagerie of theoretically expected outbursts from CEEs, we note that events in the top right of Fig. 2.1 should be relatively rare [compare with η Car; see §2.1], and those in the bottom left (stellar mergers) comparatively hard to detect in a magnitude-limited survey. Assuming that the peak luminosity of the outburst is about an order of magnitude higher than $L_{\rm P}$, we find that the whole range of $L_{\rm P}$ and $t_{\rm P}$ for stellar masses 1 to $150\,M_{\odot}$ coincides well with the observed domain for luminosities and duration of LRNe suggested in Rau et al. (2009). We can estimate the rate of CEE-originated outbursts that appear as red transients, by considering what fraction of stars in the galaxy undergo a CEE. We estimate 0.024 such events per year per Milky Way–like galaxy (§2.1), of which about half should be more luminous outbursts (results of a CE ejection), and half are lower-luminosity events (powered by stellar mergers). This is consistent with the empirical lower limit for more luminous ILRTs of 0.019 yr^{-1} for the Galaxy (Ofek et al., 2008), because we do not expect that all luminous ILRTs must be powered by a CEE [though some non-LRN ILRTs, like NGC 300-OT or SN2008S, might potentially also be triggered by CEEs (§2.1)].

The question of whether recombination energy can help to unbind a stellar envelope during a CEE is important for understanding the formation and survival of many binary systems (Han et al., 1994; Webbink, 2008). Our model suggests that a large fraction of the energy from recombination is commonly radiated away after a CEE. Such luminosity provides a beacon, which helps to illuminate and identify a CE ejection or merger at large distances. The recombination wave also controls the shape of the plateau-shaped light curve of LRNe. We therefore suggest that detecting and characterizing the population of ILRTs will help us understand CEEs.

2.1 Supplementary text

Here we provide additional information about our hydrodynamical simulations, as well as give more details behind our formulae and arguments from the main text.

2.1.1 Intermediate Luminosity Red Transients

In recent years, observers have identified a new class of transients, with peak luminosities somewhere between that of the brightest novae and Type Ia SNe and with a total energy output anywhere from 10^{45} to a few 10^{47} ergs, e.g., Mould et al. (1990); Martini et al. (1999); Bond et al. (2003); Kulkarni et al. (2007); Pastorello et al. (2007); Bond et al. (2009); Bond (2011); Kasliwal et al. (2011). Because their spectra are predominantly red, completely unlike novae, they have been called intermediate luminosity red transients (ILRTs, Bond et al., 2012). However alternate names are also in common use, either for all of the transients or for particular kinds of events, e.g. Luminous Red Novae (LRNe), intermediate luminosity optical transients, mid infra-red transients, V838 Mon-like events, and supernova impostors. The relative novelty of these classes, and the uncertainty over their physical origins, makes it unsurprising that the use of such terms is not necessarily always consistent between different papers.

It is not known what red transients are or whether they have a common cause: it has been argued that ILRTs could be due to accretion-powered jets (Soker & Kashi, 2012), tidal disruption of planets (Bear et al., 2011), nuclear outbursts (Iben & Tutukov, 1992), electron-capture SNe (Thompson et al., 2009) with shocks propagating through dusty surroundings (Kochanek, 2011), or violent stellar mergers (Soker & Tylenda, 2006). It has also been argued that – despite having similar outburst properties in terms of color and luminosity – ILRTs may have different origins (Bond et al., 2012).

In this work, we consider the particular group of red transients which are most frequently labeled as LRNe. The widely-recognized members of this class of red transients are M31-RV, V838 Mon, and M85 OT2006-1. We note that the recognition of LRNe as a special class of stellar explosion started with the last object in that list, although it was not the first of them to be detected. In this paper we also include V1309 Sco as a possible member of this LRN class, at the low-energy end (Tylenda et al., 2011). Another suggested low-energy end LRN is V4332 Sgr – this transient radiated away a total energy of only 4.5×10^{43} ergs (Tylenda et al., 2005a), an order of magnitude less even than V1309 Sco. The LRN class is likely separated from another class of red transients where progenitors were observationally identified to be dusty modestly-massive stars (with $M \sim 10 M_{\odot}$) –

as for example in the cases of SN 2008S and NGC 300 OT (Berger et al., 2009; Prieto et al., 2008; Smith et al., 2009); those ILRTs are better known as supernova impostors. Nonetheless, because the recognition of red transients as a new type of astrophysical object is very recent, their classification is not yet by any means universally established or finally accepted throughout the astrophysics community.

We note that some investigators have suggested that LRNe could be present only in old populations, with V838 Mon standing as an exception (see also the discussion against this point of view in Siegel & Bond, 2007). It is important to clarify that our proposed link between CEEs and LRNe implies that there should not be any such restriction on population age for LRNe: our CEE outburst model is related only to the reason of the ejection – a CEE – and to the self-similar physics and recombination outburst following the CEE. Indeed, CEEs may occur in binary stars with companions of any masses. In terms of rates, CEE from massive stars are expected to be much more rare, as their relative fraction in the total number of stars is small; however they are not forbidden. In addition, given the current understanding of CEE physics, it is impossible to say how the CE ejection would differ in low-mass and high-mass stars.

2.1.2 Previous problems with a merger model: what does the standard CEE model predict?

One of the most common models suggested to explain different LRNe – V838 Mon, M85 OT 2006-1 and V1309 Sco – is a merger, either of two stars, or of a star with a planet (e.g., Soker & Tylenda, 2003, 2006; Kulkarni et al., 2007; Tylenda et al., 2011). It is also known as the merger-burst model; however, because a merger is a particular type of CEE, we will hereafter refer to it as to a CEE model. The case of V1309 Sco is rather unequivocally a CEE, as observations revealed a binary prior the outburst and a single star after (Tylenda et al., 2011). However, there were problems with justifying the physics behind this model. For example, a stellar merger scenario in the case of M85 OT2006-1 was rejected because an analysis of the energy available from a merger suggested that a violent merger would be unable, by a factor of a few, to explain the energy that was radiated away from M85 OT2006-1 (Ofek et al., 2008). In Boschi & Munari (2004), striking similarities between the M31-RV, V838 Mon and V4332 Sgr outbursts were noticed, leading to a discussion which concluded that the merger-powered outburst models proposed to-that-date showed too much dependency on metallicity, mass, and ages and hence could not explain the observed homology.

We list next a number of striking observational features of LRNe which were not previously theoretically anticipated by a CEE model (one leading to either a merger or a the formation of a

close binary) and which were not emphasized as discriminating features in previous studies:

- **Large increases in radius and luminosity.** In previously published CE simulations, the increase in the stellar radius of the bound mass during fast spiral-in is usually less than a factor of 10 (see e.g., Passy et al., 2012; Ricker & Taam, 2012). These simulations were performed for binaries that are expected to survive, rather than merge, i.e. these binaries have more energy injected into the stellar envelope – relative to the binding energy – than for binaries that merge. However the well-studied example V1309 Sco reached a maximum luminosity $\sim 3\times10^4\,L_\odot$, about ~ 5000 times larger than the initial luminosity of the progenitor ($\sim 3.0-8.6\,L_\odot$), whilst its effective temperature dropped to $\sim 4000\,$K during the peak luminosity and plateau (Tylenda et al., 2011). This indicates an increase in its apparent (or effective) radius by about 90 times, reaching $\sim 300 R_\odot$ (Tylenda et al., 2011), at least an order of magnitude more than simulations suggested. Similarly, interferometric observation showed that V838 Mon expanded by ~ 300 times during the outburst, to $1570\pm400\,R_\odot$, while its progenitor was likely $5-10\,M_\odot$ with a radius of only about $5\,R_\odot$ (Tylenda et al., 2005b).

- **An unexpectedly long duration.** Expansion of the envelope during CEE is expected to occur during the dynamical plunge-in phase (see, e.g., Ivanova, 2011), i.e. the stage during which the inspiralling star loses most of its angular momentum. It is theoretically expected, and confirmed by numerical simulations (see e.g. Passy et al., 2012; Ricker & Taam, 2012), that this phase proceeds on a timescale of about several *initial* dynamical timescales of the stellar envelope of the primary star. This is a few days for the case of V1309 Sco; however, the outburst lasts ≈100 days (Tylenda et al., 2011, also see Fig. 2.2) which is comparable to dynamical timescale of this object at the *maximum* of expansion, $\tau_{\rm dyn,max}\approx 80$ days. In the case of V838 Mon, the outburst lasted for about 80 days (Crause et al., 2003) while the initial dynamical timescale would be only a couple of hours. In case of M85 OT2006-1, in which the outburst last about 60 days (Pastorello et al., 2007), there are no strong constraints on progenitor.

- **Plateau phase.** Several ILRTs outbursts, after the initial rise in brightness, featured a plateau in their light curves in the red band at a luminosity somewhat lower than at the maximum. Specifically, in case of V1309 Sco the plateau duration is ~ 25 days (depending on the definition of the start and the end of the plateau phase, from 16 to 31 days, Tylenda et al., 2011, also see Fig. 2.2), $\sim 60-80$ days in case of M85 OT2006-1 (Pastorello et al., 2007), ~ 15 days in case of V4332 Sgr (Tylenda et al., 2005a, although the start of the outburst is not well known) and $\sim 30-40$ days in case of M31-RV (Boschi & Munari, 2004). V838 Mon

has a very complex visual band light curve with several peaks separated by about 30 days. Nonetheless, it does have an easily distinguished plateau in the red part of the spectrum as well as in bolometric luminosity; the overall duration of the outburst is about 80 days, and that plateau starts ~ 30 days after the peak luminosity and lasts for another ~ 35 days (Retter & Marom, 2003; Tylenda, 2005). Most of the energy in LRNe is radiated away during the plateau phase. The plateau shape had not been predicted and had not yet been explained.

- **An extremely rapid decline.** The post-common-envelope decline in luminosity of the merger product is expected to occur on a thermal timescale, which – for these over-luminous and over-inflated objects – is typically about a year. However, the abrupt decline in luminosity (by a factor of 100) in V1309 Sco, M31-RV, V4332 Sgr and V838 Mon happened in a dozen days (Tylenda et al., 2011; Boschi & Munari, 2004; Tylenda et al., 2005a; Retter & Marom, 2003; Tylenda, 2005, also see Fig. 2.2). For V1309 Sco, the timescale for exponential decrease was determined to be only a few days (Tylenda et al., 2011). Strikingly, the timescale for this sharp luminosity decrease is considerably shorter than the dynamical timescale $\tau_{\rm dyn,max}$ at the maximum of expansion for V1309 Sco (80 days) or for V838 Mon (about 500 days).

- **Inconsistent velocities.** While expansion velocities from the spectra were several hundred km/s [e.g., in V1309 Sco (Tylenda et al., 2011), in M85 OT2006-1 (Pastorello et al., 2007), and in V838Mon (Wisniewski et al., 2003)], velocities inferred from the apparent radius expansion imply speeds from only about 20 km/s (V1309 Sco) to about 100 km/s (V838 Mon).

In §2.1.3 below we explain how the model presented in this paper naturally accounts for the above features.

2.1.3 Wavefront of cooling and recombination in a CEE

As discussed above, the light curves of LRNe have five similar striking features, where two are the most exceptional in providing important clues to the physics of the outburst. First, the outbursts have a roughly constant plateau luminosity $L_{\rm P}$ for a time $t_{\rm P}$ that is typically dozens of days (for a note on the special case of V838 Mon see, see §2.1.5). Second, the inferred radius of the photosphere increases relatively slowly during most of the plateau phase, at the end of which the apparent radius decreases very quickly. This is reminiscent of the behavior of type IIP supernovae, in which the photosphere does not stay at a fixed Lagrangian coordinate but moves inwards in mass as the

ejecta expands and cools; roughly self-similar, homologous expansion means that the radius of the photosphere and luminosity of the emission remain approximately constant (Imshenik & Nadezhin, 1965; Grassberg et al., 1971; Grasberg & Nadezhin, 1976; Popov, 1993; Eastman et al., 1994).

Such a photosphere-defining 'cooling wave,' propagating inward in the frame of the expanding shock, was predicted for terrestrial explosions in air by Zel'Dovich et al. (1958a,b). This type of behavior does not need to be associated with recombination; it is only dependent on a non-linear temperature dependence of the opacity of the ejecta (see also Bethe, 1964), which argues that the necessary condition is that the effective opacity increases more rapidly than a cubic power of temperature). The low-opacity material outside the photosphere is able to cool by radiation much more effectively than the hot, high-opacity material inside. However, in the case considered here, as well as for type IIP SNe, recombination is the cause of the change in opacity that leads to this cooling-wave. The location of the effective photosphere is controlled by a sudden large reduction in the mean opacity of the ejecta after hydrogen recombination.

Even though the mean opacity greatly drops outside the region of recombination, the photons emitted during recombination will not in general escape directly. Although neutral hydrogen has a much lower Rosseland mean opacity when compared to ionized hydrogen, the relevant line opacity of neutral hydrogen is higher than for the ionized material. So the recombination photons themselves have a short mean free path, and there is no reason to expect strong H_α line emission, even if photons at other wavelengths are free to escape. Uniformly applying the Rosseland mean opacity in this case would be misleading, and full wavelength-dependent radiative transfer would be necessary to simulate precisely the structure of the cooling wave. Hence situations where the location of the cooling wave is defined by recombination are more complicated than the cases first considered by Zel'Dovich et al. (1958a,b), in particular because there is a release of energy from recombination that is coincident with the change in opacity. However, we consider that the energy input is so close to the photosphere that it justifies neglecting the effect of any heating on the main features of the hydrodynamics.

This physics is well-studied in the context of supernovae, and we can apply appropriate results here. The analytic model of Popov (1993), based on the idea of there being a wavefront of cooling and recombination (WCR), is particularly attractive. Although the method produces only approximate light curves, it provides accurate scaling relations that give insight into the underlying physics and to the interpretation of observations. Indeed, Kasen & Woosley (2009) verifies the major results of the Popov model with detailed hydrodynamical simulations that include radiative transfer.

The analytic WCR model has the following intrinsic features:

a) An outburst has a plateau phase. (For more on the condition which must be satisfied in order

to obtain a plateau, see below.);

b) Because the observable surface during the outburst is not the stellar surface, but instead the photosphere of the expanding ejected material defined by the location of the WCR, a large apparent radius increase is expected;

c) As this recombination front propagates inwards through the material by mass, its geometrical distance to the center can gradually increase and then decrease until the recombination of the material is over (see Eq. 16 in Popov, 1993), while at the same time the outflow passing through the WCR continues to stream outward. This leads to what could be observationally identified as an inconsistency between measured material expansion velocities and apparent expansion of the radiating surface: the photometric velocity indicating the expansion rate of the photosphere can be much less than spectroscopic velocities, which give the speed of the gas passing through the photosphere;

d) The model connects the outburst not with the dynamical timescale on which the CE rapidly expands, but with the timescale over which recombination wave proceeds;

e) After the recombination is completed, the model allows sudden transparency, which could be observed as rapid decline of luminosity and appearance of the central object. If material above the front is dense and cool enough, it could form dust that would hide the central object again (for a discussion of dust formation in the ejecta of a related class of transients then see, e.g., Kochanek et al., 2012).

The recombination process depends strongly on how not only temperature, but also density, evolves. Hydrodynamical simulations show that recombination temperature in this model is $\sim 5000-6000\,\mathrm{K}$ for thick and dense ejected envelopes, as in case of SNIIP (Popov, 1993; Kasen & Woosley, 2009). Somewhat colder recombination temperatures are expected in less dense ejecta, where the number density of free electrons (which are required for recombination) is smaller. In the grey atmosphere approximation, the effective temperature is a factor of $2^{1/4} \approx 1.2$ larger than the recombination temperature, corresponding to effective temperatures in the $\sim 4000-6000\,\mathrm{K}$ range (see also Litvinova & Nadezhin, 1985, who showed that effective temperatures shift to lower values once the energy of the outburst is decreasing). Although full 3D hydrodynamical simulations with radiative transfer are necessary for more detailed calculations of the effective temperature, it is clear that the WCR model predicts that a CEE outburst will be bright in the red part of the spectrum. The above is a simplification of the complicated situation occurring in these photospheres (e.g. it neglects the role of H^- ions formed due to electrons donated from metals), but the outcome of a detailed analysis should yield similar conclusions.

For this study, we take the WCR model derived by Popov (1993), in the convenient form expressed by Eastman et al. (1994), and re-scale it to the situation we are studying.[1] We scaled opacities to 0.32 $\mathrm{cm^2\,g^{-1}}$ for $X = 0.7$. The original derivation by Popov (1993) assumed that the kinetic energy input produces self-similar expansion of an envelope moving with constant velocity. This implies that the potential well of the exploding star has already been overcome, and hence that energy input for his equations in the case of CEE is the same quantity as $E_{\rm k}^{\infty}$.

An important assumption in Popov's model is that recombination, although controlling the energy release through its effects on opacity, does not dominate the dynamics of the expansion. In the case of CEE, we can estimate from Eq. (3) of the main paper how much energy is available from recombination. For typical cases of partial envelope ejection, such as in the simulated case of V1309 Sco below, the kinetic energy in the outburst is $E_{\rm k}^{\infty} \sim 3-4\times10^{47}(\,m_{\rm unb}/M_{\odot})\,$erg, exceeding the recombination energy by more than an order of magnitude. For cases of complete CE ejection, we can estimate the kinetic energy $E_{\rm k}^{\infty}$ to be of the same order as the initial potential energy of the CEE progenitor-star: $E_{\rm k}^{\infty} = Gm_{\rm unb}(m_1 - m_{\rm unb})(\lambda R_{\rm init})^{-1}$, where λ is an envelope structure parameter that is roughly of order unity for small low-mass giants but that can be as small as 0.01 for massive and larger giants (Loveridge et al., 2011). Then

$$\frac{E_{\rm k}^{\infty}}{E_{\rm recomb}} \sim 150 \times (X + 1.5 Y f_{\rm He})^{-1} \, \frac{m_1 - m_{\rm unb}}{M_{\odot}} \left(\frac{\lambda R_{\rm init}}{R_{\odot}} \right)^{-1} .$$

So $E_{\rm k}^{\infty}$ easily exceeds $E_{\rm recomb}$ by at least an order of magnitude. Hence, although the recombination energy is a larger fraction of E_k^{∞} in the CEE problem than it is in the Type IIP SNe problem, the recombination energy is still relatively small enough that we feel justified in assuming that it should not play a significant role in driving the dynamics, therefore making Popov's model applicable for CEE.

We briefly clarify here that the analysis for $E_{\rm k}^{\infty}$ above must self-consistently extend to the choice of ζ for complete envelope ejection. For that reason, a typical ζ for complete envelope ejection might be expected to be somewhat higher than a typical ζ for ejection resulting from a merger event. In those extreme cases where $\lambda = 0.01$ then an assumption of $\zeta = 100$ would become reasonable, though the range $1 < \zeta < 10$ seems likely to be more typical.

In Popov's simplified analytical model for the WCR, the main role of recombination is to provide the reason that the gas switches from opaque to transparent, resulting in a plateau-shaped light-curve. The Popov model predicts that light curves will be self-similar to each other, with their shape characterized by the dimensionless parameter Λ: larger values of Λ correspond to more

[1] For Eq. 2.1 in the main text, we have corrected a small numerical error in the coefficient of Eq. 9 of Eastman et al. (1994), for the plateau luminosity, such that it is consistent with the Popov (1993) value.

pronounced plateaus. We find that, scaling for the case of CEE-outbursts, Λ from Popov (1993) can be calculated as

$$\Lambda \approx 49 \left(\frac{R_{\rm init}}{3.5 R_\odot}\right)^{-1} \left(\frac{E_{\rm k}^{\infty}}{10^{46}\,{\rm erg}}\right)^{-1/2} \left(\frac{m_{\rm unb}}{0.03 M_\odot}\right)^{3/2} \left(\frac{\kappa}{0.32\,{\rm cm^2\,g^{-1}}}\right)^{2} \left(\frac{T_{\rm rec}}{4500\,{\rm K}}\right)^{4},$$

which for cases of complete envelope ejection becomes

$$\Lambda \approx 1700 \lambda^{1/2} \left(\frac{R_{\rm init}}{R_\odot}\right)^{-1/2} \left(\frac{m_{\rm unb}^2}{(m_1 - m_{\rm unb}) M_\odot}\right)^{1/2} \left(\frac{\kappa}{0.32\,{\rm cm^2\,g^{-1}}}\right)^{2} \left(\frac{T_{\rm rec}}{4500\,{\rm K}}\right)^{4}.$$

Consequently, for most of the range of possible CEE-progenitors, $\Lambda \gg 1$, and hence a plateau phase with sudden transparency is predicted. If $\Lambda \ll 1$, which is not a likely case for CE progenitors, the model predicts slow decline with no well defined plateau in the light-curve. Cases with intermediate values of $\Lambda \sim 1$ may provide a phase somewhat like a plateau, with the luminosity taking a comparatively long time to decline after recombination is completed (see also Fig. 2.3).

We note that these scaling relations were derived under the approximation that the ejection is spherically symmetric, which may well be less accurate here than for supernovae. In addition, Popov (1993) assumed that the plasma was radiation dominated, which may well be less appropriate for matter ejected from a stellar merger than for supernova ejecta. However, it has previously been noted that at the location of the cooling wave recombination itself will automatically lead to radiation becoming dominant (e.g., Chugai, 1991), which helps to justify our adoption of the Popov expressions. Indeed, Kasen & Ramirez-Ruiz (2010) show that during the recombination phase the third generalized adiabatic index (Γ_3) decreases below the normal value for radiation-pressure dominated matter, even for initially gas-pressure dominated matter. This allows continued expansion by an order of magnitude or more at near-constant temperature – independent of whether the initial matter is gas- or radiation-pressure dominated – and also increases the relative importance of radiation pressure, even in initially cold envelopes.

2.1.4 Simulations of V1309 Sco

For the properties of the pre-merger contact binary in V1309 Sco, we take a low-mass subgiant with mass $M_1 \sim 1.52 M_\odot$ and radius $R_1 = 3.5 R_\odot$ with a lower-mass companion of $M_2 \sim 0.16 M_\odot$ (Stępień, 2011), with an orbital period at Roche Lobe overflow of $P_{\rm orb} \sim 1.42$ days (the last detected orbital period before the merger, Tylenda et al., 2011).

The binding energy of the envelope of a subgiant representing V1309 Sco primary is $|E_{\rm bind}| \simeq 1.5 \times 10^{48}$ erg (as is standard, here we include both the gravitational potential and internal thermal

energy terms but not the recombination term). Stellar model calculations were performed using the STARS/ev stellar evolution code, originally developed by Eggleton (1971, 1972, 1973); Eggleton et al. (1973), with recent updates described in Pols et al. (1995); Glebbeek et al. (2008) and references therein. For this companion mass of $0.16 M_\odot$, even if the companion survives the entire spiral-in and the orbital energy is released as close as possible to the boundary of the primary's core (i.e. providing the maximum possible energy output), the merger would produce only about $\Delta E_{\rm orb} \simeq 5 \times 10^{47}$ erg. This is only a third of the envelope's binding energy. So a CEE in this system necessarily results in a merger before the envelope is unbound.

However, for this particular primary, soon after the companion starts to plunge-in, the released orbital energy near the surface exceeds the binding energy of that part of envelope already outside the location of the companion. From the detailed stellar model, we find that the mass that can become unbound during this initial phase of the spiral-in is $m_{\rm unb} \approx 0.04 M_\odot$. The total orbital energy that was deposited in this mass is $\sim 6 \times 10^{46}$ ergs; some of this material will be ejected only barely faster than the local escape velocity ($v_{\rm esc} \approx 420\,$km/s for the unperturbed star) and some will get significantly more specific kinetic energy. Ejected matter that is given more energy than is required for overcoming the potential barrier will still have non-zero kinetic energy at infinity $E_{\rm k}^{\infty} > 0$; this will be smaller than the total energy deposited, but should be of the same order.

The magnitude of the initial velocity v of the ejected upper layers can be qualitatively understood by considering a circular binary consisting of two companions with masses m_1 and m_2, orbital separation a, and total orbital angular momentum J approximated by Keplerian two-body expressions: $J = \mu \Omega a^2 = m_1 m_2 (Ga/M)^{1/2}$, where the reduced mass $\mu = m_1 m_2 / M$, $\Omega^2 = GM/a^3$, and $M = m_1 + m_2$. To shrink the orbit by da, a fraction of the orbital angular momentum dJ must be transferred to a portion dm_1 of the stellar envelope material. This angular momentum transfer occurs in the very top layers of the primary star, and hence the stellar mass which is inside the orbit of the companion star does not significantly change. Therefore, treating m_1 and m_2 as constant,

$$dJ \approx \frac{1}{2} \frac{J}{a} da = \frac{1}{2} \mu \Omega a da \; .$$

When the companion already orbits inside the envelope, $a \approx r_1$ (although the r_1 describing particular particles of matter can be somewhat larger than their initial r_1 in an unperturbed star). In the process, the stellar material dm_1 achieves an angular momentum $dJ = v r_1 dm_1$, implying a tangential velocity

$$v \approx \frac{1}{a} \frac{dJ}{dm_1} \approx \frac{1}{2} \mu \Omega \left(\frac{dm_1}{dr_1} \right)^{-1} .$$

For the masses and initial orbital period used in our V1309 Sco simulations, we find that this

initial tangential velocity is

$$v \approx 2.5 \text{ km s}^{-1} \left(\frac{dm_1/M_\odot}{dr_1/R_\odot} \right)^{-1}.$$

From the mass profile of the larger star's envelope, $dm_1/dr_1 = 4\pi r_1^2 \rho(r_1)$, where $\rho(r_1)$ is the density profile and r_1 is the distance to the center of the donor. In the upper $0.02 M_\odot$ of our pre-merger $1.52 M_\odot$ star $(dm_1/M_\odot)/(dr_1/R_\odot) \sim 10^{-4}$–$10^{-1}$, with smaller values closer to the surface. We note that when mass ejection begins, the layers will expand and somewhat more mass will have even smaller values of $(dm_1/M_\odot)/(dr_1/R_\odot)$. A significant fraction of this upper envelope therefore is expected to be ejected at velocities higher than $v_{\rm esc}$. Considering the pre-merger orbital configuration, the expected kinetic energy at infinity is of order $\sim 10^{46}$ erg.

The estimates above were made for a symmetric, non-rotating 1D stellar model. For a real – 3D – star filling its Roche lobe, most of the companion-envelope interactions occur close to the orbital plane. There the star's radius would be larger than for 1D models, so we expect that more mass could be lost in the rotating case. Yet, since most of this expansion of the stellar structure happens in the very outer layers, we do not expect the enhancement to be more than a factor of a few.

From the stellar model, we also find that $f_{\rm He} \approx 0.8$. Hence, if all mass that could become unbound would also recombine, the total energy that can be radiated away during the recombination in V1309 Sco case is $\sim 10^{45}$ erg – so the available recombination energy reservoir can explain the observed outburst's energy very well.

For a better estimate about how much mass could be ejected, we performed several numerical simulations using the 3D SPH code `StarCrash` (Lombardi et al., 2006; Gaburov et al., 2010). This code was specifically re-developed to deal with close binary systems (Lombardi et al., 2011). For these numerical studies, we varied the initial orbital period around the observed pre-merger value $P_{\rm orb} \sim 1.42$ day (Tylenda et al., 2011). Table 2.1 gives the complete list of initial conditions, including rotational synchronization of the giant. The companion was modeled as either a low-mass main sequence star (with SPH particles) or as a point mass (representing the core of a red giant which lost its envelope in a previous binary interaction, Stępień, 2011). Stellar structures were first calculated using the `STARS/ev` code and then relaxed in `StarCrash` in a binary configuration close to Roche-lobe overflow. As a result of this relaxation, the radius of the giant in the orbital plane was slightly larger than its 1D radius obtained with the stellar code as expected (Renvoizé et al., 2002).

A visualization of simulation ps334 presents the evolution of the column density (in g/cm^2) as viewed from a direction perpendicular to the orbital plane. After the merger, $\sim 0.06 M_\odot$ of unbound material is left streaming from the merger product with some deviation from axisymmetry, including clumpiness. In all simulations the merger ejects a small fraction of the donor, and the

unbound mass is comparable with our preliminary estimates, $\sim 0.04 M_{\odot}$ (depending on the degree of corotation, it varies from ~ 0.03 to $0.08 M_{\odot}$, see Table 2.1). This mass is obtained by computing the total energy (kinetic, gravitational and internal) for each particle: if this energy is positive, the particle is considered to be unbound. We find that for the same donors, having a MS companion will result in less mass ejection. For most simulations, the mass is ejected in two episodes (see Fig. 2.2), where during the first episode the companion is still outside the giant, and during the second it is plunging-in. In simulations mn351 and ms376, three episodes of mass ejection were observed. In one simulation, ms372, the mass ejection was mostly continuous. The mass ratio between first and second mass ejection varies from about 80% of all unbound mass being ejected during the first mass outburst to about 36%. The time interval between the starts of the first and last mass outbursts varies from 1 to 9 days, and the specific kinetic energy during the first mass outbursts is larger (see, e.g., Fig. 2.4).

As reported in Table 2.1, the kinetic energy of the unbound material at infinity $E_{\rm k}^{\infty}$ is $\sim 10^{46}$ erg. The initial energy powering the ejection $E_{\rm k}$ is larger, and is partly spent on overcoming the potential well just near the merged star, so $E_{\rm k}^{\infty}$ is not identical to $E_{\rm k}$. In each individual simulation, $E_{\rm k}^{\infty}$ asymptotically approaches some value soon after the merger (see Fig. 2.4). We find that the total value of $E_{\rm k}^{\infty}$ is larger when the unbound mass is larger, but the specific kinetic energy is lower.

We note that the observed V1309 Sco light-curve (see Fig. 2.2) might well be reproduced best assuming that, as in most simulations, there were two or three episodes of mass ejection, where in the first episode the unbound mass had higher ejection velocity (Fig. 2.5). It is tempting to interpret this as a promising sign for this model, and not just to the extent that adding more free parameters will always allow a better fit. Nonetheless, we recognize that a strong conclusion with regard to this point requires more sophisticated radiative transfer calculations in order to produce light-curves that properly take into account the asymmetry and structure of the ejected matter.

2.1.5 Individual objects

V838 Mon

V838Mon's light curve is an exception as being more irregular – its V magnitude exhibits three phases of brightening (Retter & Marom, 2003), with plateaus being very pronounced in bolometric luminosity (which is dominated by red spectra) during the last two peaks in V. This complex behavior might easily be linked to a dramatic and asymmetric start of a CEE. One way a CEE event can start is because of the Darwin instability (which is likely the case for V1309 Sco, as it is a system presumably with a large mass ratio); in this case a CE is formed almost immediately, on a

dynamical timescale. The other trigger for a CEE event is when one of the stars starts overfilling its Roche lobe due to evolutionary expansion (this might be the case for V838 Mon). In the latter case, the creation of a CE does not necessarily occur on a dynamical timescale: at the very beginning of the contact, loss of surface layers is not expected to occur smoothly and continuously. Mass transfer can bring a giant out of contact, either due to a binary expansion or due to contraction of the giant in response to sudden mass loss, and the mass transfer unavoidably will be continued later. This stage of evolution – the start of the CEE in giants – is not well understood and is currently under debate (for a review on the current understanding see Ivanova, 2011). The binary may then proceed to a CEE on a timescale which can be estimated to be anywhere from a year to hundreds of years (Podsiadlowski, 2001; Ivanova, 2011). We suggest hence that the observed three peaks of brightening are most likely linked to either one highly asymmetric interaction resulting in many clumps or to several mass outbursts, similar to the case V1309 Sco discussed above, but possibly not resulting in a merger.

It is remarkable as well that it is likely that V838 Mon is a binary star now (Munari et al., 2007), and hence may deliver several more interesting eruptive events before it completes its CEE evolution with either merger or the formation of a compact binary.

ILRTs from massive dusty stars

Some red transients have progenitors well identified to be cool red giants surrounded by dust. Noticeable examples are SN 2008S and NGC 300 OT (Berger et al., 2009; Prieto et al., 2008; Smith et al., 2009). A very good model explaining the physics of an explosion propagating through a cool expanded envelope was developed by Kochanek (2011). A CEE outburst model as described in our manuscript might seem – at first sight – not applicable. To start with, CEE outbursts presume that an envelope is still hot enough to be ionized.

However, the reason for the explosion in that model (Kochanek, 2011) is not fully established. It has been argued that it could be an electron-capture supernova (Berger et al., 2009) which occurred in an extreme asymptotic giant branch (AGB) star. The progenitor is suggested to have been a cold star with $T_{\rm eff} = 2500\ K$ and $\lg_{10}(L/L_{\odot}) = 4.6$ and 4.9, where the total energies radiated away in the transient stages were 3×10^{47} and 8×10^{47} erg, for SN 2008S and NGC 300-OT respectively (Kochanek, 2011).

Whilst a progenitor with those properties is consistent with being a massive AGB star, similar characteristics could also be possessed by a red giant during a long-term quasi-stable CEE phase known as the self-regulating spiral-in. This situation is expected to occur if the envelope was not ejected promptly during the plunge-in phase; in this case the companion orbits inside the CE in

a very rarefied region and the phase can last hundreds of years (Podsiadlowski, 2001). The stars appear to be puffed-up and somewhat cooler than would be predicted by standard evolutionary tracks (Ivanova & Podsiadlowski, 2002). In addition, the initial mass outburst during the initial interaction and the plunge-in (see the discussion on V838 Mon above) will cool down, potentially forming dust around the system. In this case, the main orbital energy release occurs deep inside the star, at the bottom of the expanded envelope. For stars orbiting AGB cores, the orbital energy release can easily be as high as a few times 10^{48} erg.

We therefore note that we can not rule out CEE from the list of possible triggers of the explosion underlying this subclass of ILRTs, even though the physics of the outburst is different from the WCR-determined model, since the outer parts of the extended envelope are cool enough to have recombined before the outburst.

η Carinae

The Great Eruption of η Carinae, which may also have been triggered by a stellar merger (see e.g., Podsiadlowski, 2010, and references therein), was recently measured via light echoes, and was surprisingly cool (Rest et al., 2012), as would have been produced if a recombination wave defined the photosphere. The amount of energy radiated was certainly too large to have been powered purely by the recombination of a sensible amount of material, so additional energy input would have been required.

2.1.6 Rates

A lower limit for the ILRT rate from observations is 0.019 yr^{-1} L_{MW}^{-1} (Ofek et al., 2008), where L_{MW} represents the luminosity of our Galaxy. With a star formation rate of $\approx 2\ M_{\odot}$ per year (though rates can be from 1 to 10 $M_{\odot}$ per year, Chomiuk & Povich, 2011) and with initial mass function from Kroupa (2002), we find that, per year, roughly 0.3 stars are formed with masses large enough ($\geq 1 M_{\odot}$) to evolve off the MS in less than a Hubble time. Roughly half of stars are in binaries, and, for these initial masses, 16% of those binaries evolve via CEE (with 48% of the binaries surviving the CEE and the other 52% experiencing a merger) (Politano et al., 2010). Hence the theoretically expected rate of CEEs is ~ 0.024 yr^{-1} L_{MW}^{-1}, in agreement with the observed lower limit.

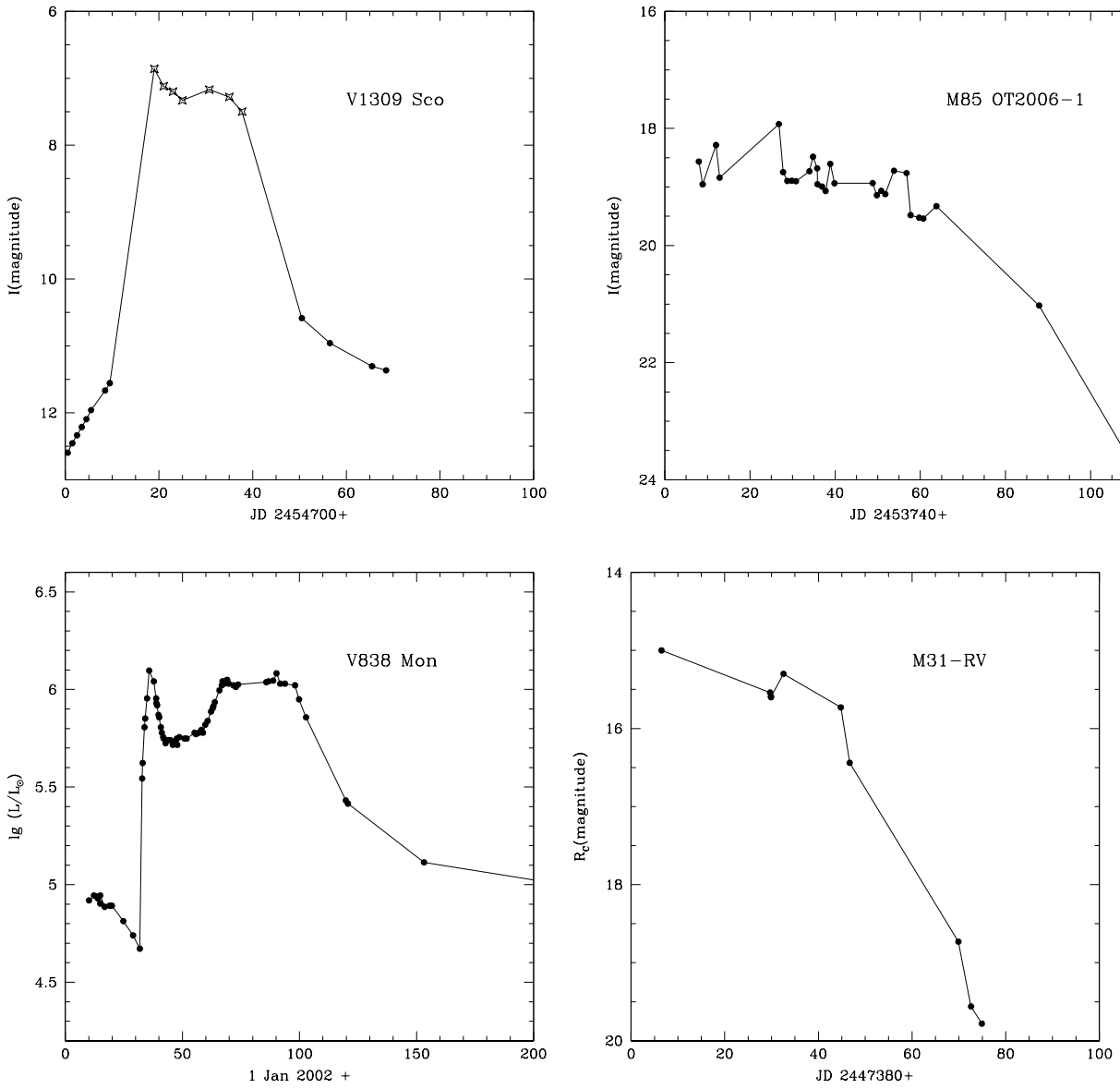

Figure 2.2: Observed evolution of magnitudes or luminosity for LRNe discussed in the text. Data were taken from Pastorello et al. (2007) for M85 OT2006-1, from Tylenda (2005) for V838 Mon and from Boschi & Munari (2004) for M31-RV. For V1309 Sco, we used data from AAVSVO (available at `http://www.aavso.org/`), marked by asterisk symbols, and from OGLE-II (Udalski, 2003), marked as solid dots.

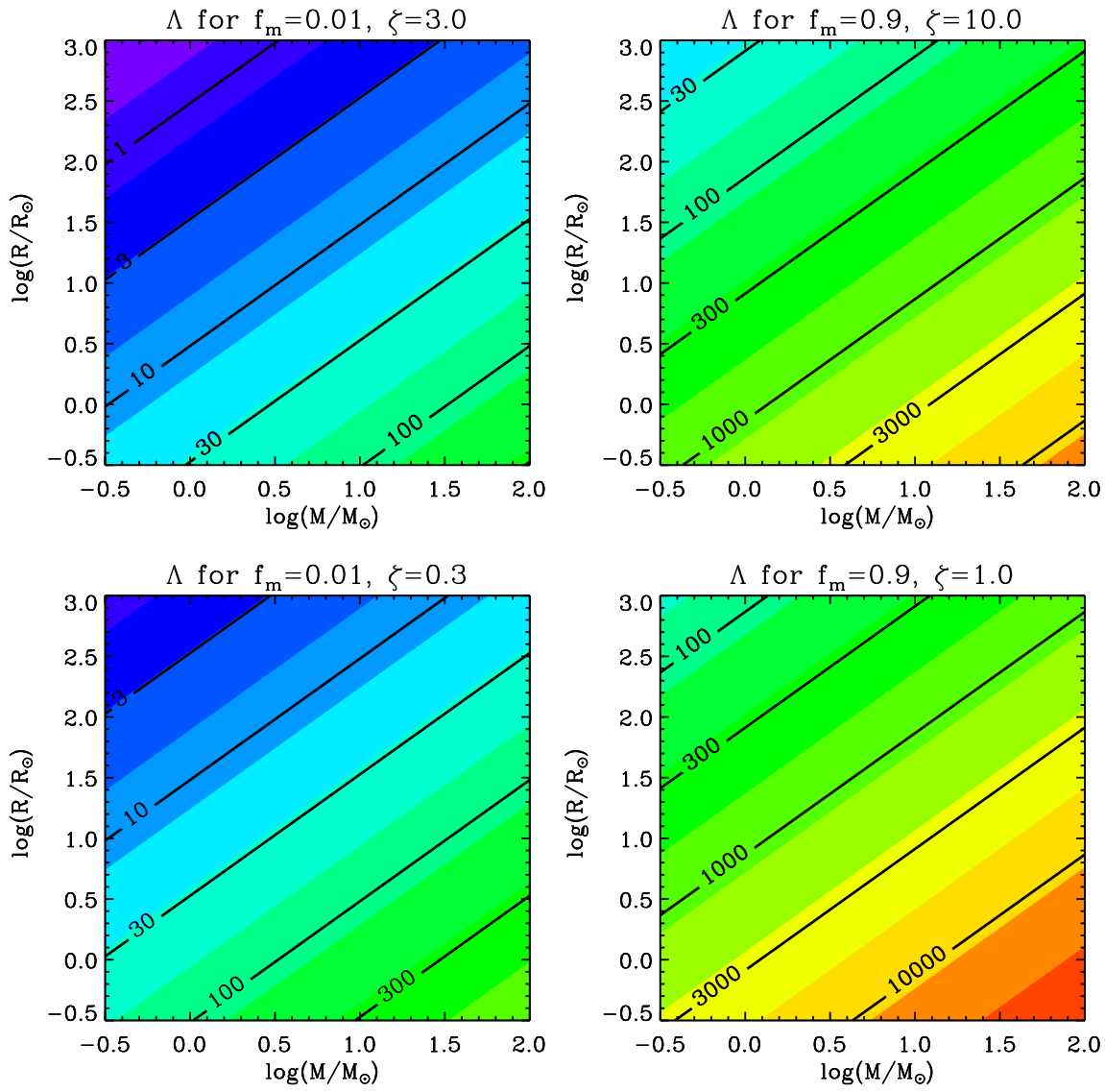

Figure 2.3: Values of Λ, i.e. the parameter which indicates whether the outburst is expected to lead to a plateau, as calculated from Popov (1993). We show how these Λ-values vary across a notional pre-CEE mass-radius plane for a selection of parameter choices indicative of different potential physical situations. The two left-hand panels are estimates for mergers which eject one percent of the mass of the primary star (i.e. $f_{\rm m} = 0.01$); the lower panel adopts $\zeta = 0.3$ and the upper panel $\zeta = 3$. The two right-hand panels represent estimates for envelope ejection (i.e. $f_{\rm m} = 0.9$); the lower panel adopts $\zeta = 1$, and the upper panel $\zeta = 10$ (as discussed in the text, it is reasonable to expect that ζ may typically be higher for full envelope ejection than for mergers). Only when small amounts of matter are lost from unusually large low-mass stars does Λ fall as low as 1. Hence we expect a plateau to be produced in the vast majority of CEE-related outburst light-curves.

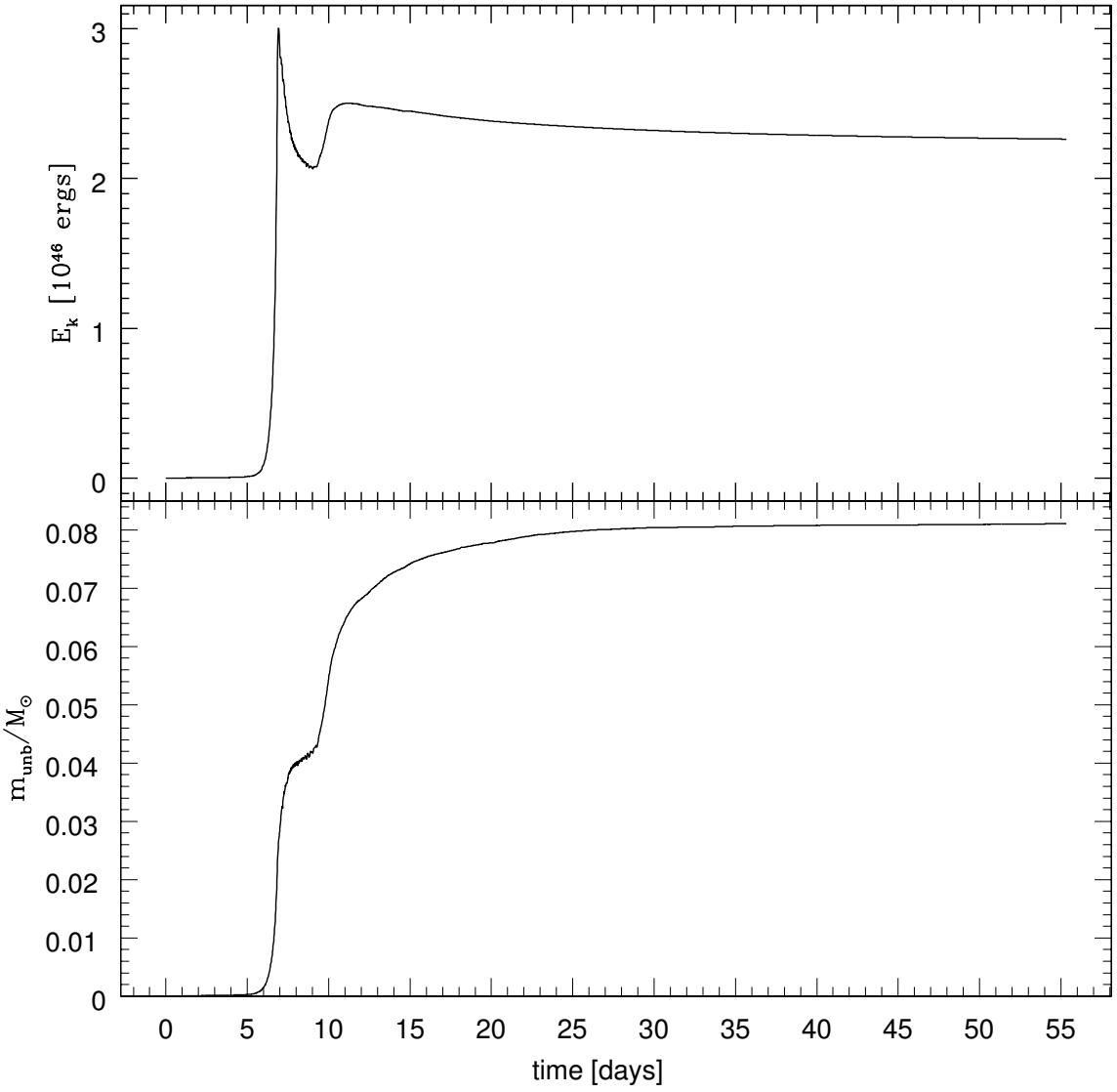

Figure 2.4: The time evolution of the kinetic energy $E_{\rm k}$ of the ejected material (top panel) and unbound mass $m_{\rm unb}$ (bottom panel) in simulation ps379. In the lower panel, note the two episodes of mass ejection, near times of 6 days and 10 days.

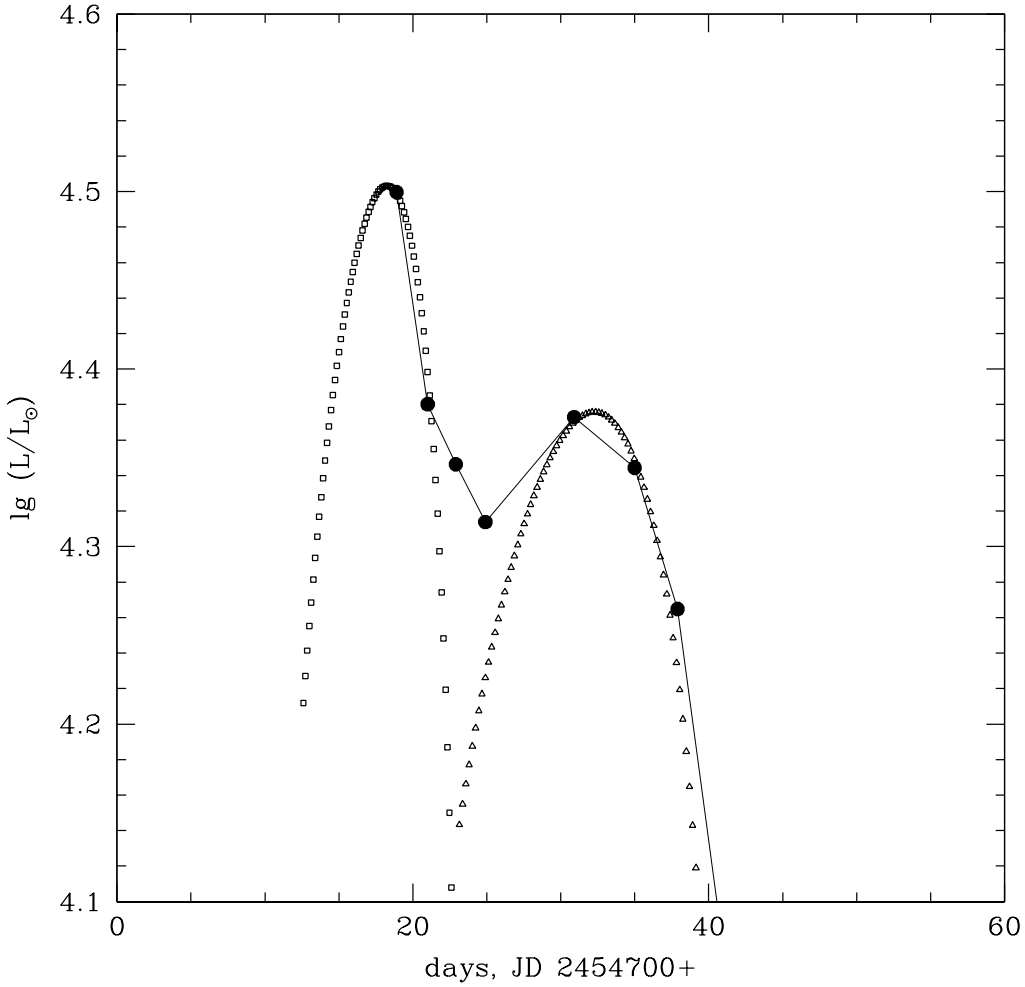

Figure 2.5: The observed evolution of bolometric luminosity during the V1309 Sco outburst (Tylenda et al., 2011) is represented by solid circles and a thin line. We compare this to the solutions of Eqs. 17 and 21 of Popov (1993), using two consecutive mass outbursts. The light-curve resulting from the first mass ejection is shown by squares: $m_{\rm unb} = 0.02 M_{\odot}$, $E_{\rm k} = 0.9 \times 10^{46}$ erg, $E^0_{\rm TH} = 0.13 \times 10^{46}$ erg is the initial thermal energy in this ejected layer, $E_{\rm th} = E_{\rm k}/2 + E^0_{\rm TH}$ (the material is shocked, the standard case for Popov's model when $E^0_{\rm TH} \ll E_{\rm k}$), the fit was done with $T_{\rm rec} = 5000$ K, characteristic for this peak (Tylenda et al., 2011). The light-curve resulting from the second mass ejection is shown with triangles $m_{\rm unb} = 0.04 M_{\odot}$, $E_{\rm k} = 0.9 \times 10^{46}$ erg, $E^0_{\rm TH} = 0.75 \times 10^{46}$ erg is the initial thermal energy in this ejected layer, $E_{\rm th} = E^0_{\rm TH}$ (no shock heating in second ejection. We adopted this for two reasons: a) this layer possesses $E^0_{\rm TH}$ larger than it would be suggested by Popov's approximation $E_{\rm k}/2$; b) the second mass outburst occurs after the companion is below the ejected layer), the fit used $T_{\rm rec} = 4000$ K, characteristic for this peak (Tylenda et al., 2011). The interval between the beginnings of the two outbursts is 6.7 days.

Model	R_1^{ev}	R_1	a	P_{orb}	f_{sync}	f_{RLOF}	N_{part}	Type	m_{unb}	E_k^{∞}	L_P	t_P
ps334	3.4	3.34	6.32	1.42	0.915	0.921	50000	PM	0.042	2.03	2.2e4	21
mn351	3.4	3.51	6.32	1.42	0.000	0.968	100000	MS	0.039	1.64	2.3e4	16
pn351	3.4	3.51	6.32	1.42	0.000	0.968	100000	PM	0.061	1.63	1.8e4	22
ps351	3.4	3.51	6.32	1.42	1.000	0.968	170000	PM	0.065	2.22	2.2e4	22
ms376	3.65	3.76	6.55	1.50	1.000	0.999	100000	MS	0.040	1.42	2.0e4	18
ps376	3.65	3.76	6.55	1.50	1.000	0.999	100000	PM	0.056	1.87	2.1e4	21
ms372	3.7	3.72	6.40	1.45	0.937	1.013	50000	MS	0.041	1.51	2.1e4	19
ps379	3.73	3.79	6.32	1.42	0.854	1.045	100000	PM	0.081	2.25	2.0e4	25

Table 2.1: Results from SPH simulations. R_1^{ev} is the radius of the donor from the stellar code in $R_\odot$, R_1 is the largest spatial size of the pre-CEE donor in the SPH simulation after relaxation in $R_\odot$, a is the initial orbital separation in $R_\odot$, P_{orb} is the initial orbital period (in days) of the relaxed binary in the SPH code, f_{sync} gives the synchronization of the red giant with the orbit (0 is for no rotation, 1 is for fully synchronized), N_{part} is the number of particles representing the giant star, and f_{RLOF} is the fraction of the radius of the primary with respect to its Roche lobe radius. MS is a main sequence star represented with 20 000 particles in mn351, and with 2000 particles in ms372 and ms376. PM is a point mass. The remaining columns give results and derived quantities: m_{unb} is the unbound mass in $M_\odot$; E_k^{∞} is the kinetic energy at infinity in 10^{46} ergs; L_P is the plateau luminosity in $L_\odot$ calculated from Eq. 2.1 of the main text; and t_P is the duration of plateau phase in days, calculated from Eq. 2.2 of the main text.

Acknowledgments: N.I. acknowledges support from the Natural Sciences and Engineering Research Council of Canada and the Canada Research Chairs Program. S.J. acknowledges support from the Chinese Academy of Sciences and National Natural Science Foundation of China. J.L.A.N. acknowledges support from CONACyT. J.C.L. thanks R. Scruggs for useful discussions. This research has been enabled by the use of computing resources provided by WestGrid and Compute/Calcul Canada as well as the Extreme Science and Engineering Discovery Environment (supported by NSF grant OCI-1053575).

Chapter 3

V1309 Sco — Understanding a merger

J. L. A. Nandez[1], N. Ivanova[1], and J. C. Lombardi Jr.[2]

[1]Department of Physics, University of Alberta, Edmonton, AB, T6G 2E7, Canada;
avendaon@ualberta.ca
[2]Department of Physics, Allegheny College, Meadville, PA 16335, USA.
Received 2013 November 25; accepted 2014 March 11; published 2014 April 15
DOI:10.1088/0004-637X/786/1/39

ABSTRACT

One of the two outcomes of a common envelope (CE) event is a merger of the two stars. To date, the best known case of a binary merger is the V1309 Sco outburst, where the orbital period was known and observed to decay up to the outburst. Using the hydrodynamical code `StarSmasher`, we study in detail which characteristics of the progenitor binary affect the outburst and produce the best match with observations. We have developed a set of tools in order to quantify any CE event. We consider binaries consisting of a $1.52\,M_{\odot}$ giant and a $0.16\,M_{\odot}$ companion with $P_{\rm orb} \sim 1.4$ days, varying the nature of the companion and its synchronization. We show that all considered progenitor binaries evolve toward the merger primarily because of Darwin instability. The merger is accompanied by mass ejection that proceeds in several separate mass outbursts and takes away a few percent of the donor mass. This very small mass, nonetheless, is important as it is not only sufficient to explain the observed light curve, but it also carries away up to one-third of the both initial total angular momentum and initial orbital energy. We find that all synchronized systems experience L_2 mass loss that operates during just a few days prior to the merger and produces ring-shaped ejecta.

The formed star is always a strongly heated radiative star that differentially rotates. We conclude that the case of a synchronized binary with a main-sequence companion gives the best match with observations of V1309 Sco.
Key words: binaries: close – hydrodynamics – stars: individual: V1309 Sco – stars: kinematics and dynamics – stars: rotation
Online-only material: animations, color figures

3.1 Introduction

More than half of all stars are in binaries or systems of even higher multiplicity (triplets, etc.) — e.g., as many as two-thirds of G stars are in multiple systems (Duquennoy & Mayor, 1991). The binary fraction increases with the spectral class, and for massive stars it is so large that more than 70% of them are expected to exchange mass with a companion (Sana et al., 2012). The fate of a binary is decided by how stable or unstable this mass transfer is. If the companion is not able to accept all the transferred mass, then the two stars start to share their outer layers, forming a so-called common envelope (CE). The outcome of the CE depends on how much orbital energy is deposited in the envelope. If the binary deposits enough orbital energy, the envelope could be ejected and a new binary composed of the companion and the core of the donor will be left in a tight orbit (Paczynski, 1976; Webbink, 1984). However, if the binary does not deposit enough energy, it will instead merge to form a single star (for more details and for the most recent review of the CE event; see Ivanova et al., 2013b).

A new class of transients was recently identified. With a total energy output anywhere in the range of $10^{45} - 10^{47}$ erg, their peak luminosities were just below that of Type Ia SNe while still above that of novae (see, e.g., Bond et al., 2003; Kulkarni et al., 2007; Bond, 2011). The spectra of these mysterious transients are predominantly red, completely unlike novae, and they are known under several alternate names: luminous red novae (LRNe), intermediate luminosity red transients, intermediate luminosity optical transients (ILOTs), V838 Mon-like events, and supernova impostors. In this work, we pay specific attention to those of red transients, which are usually labeled as LRNe, with the most important examples being V838 Mon (Kimeswenger et al., 2002), V1309 Sco (Tylenda et al., 2011), M85 OT2006-1 (Rau et al., 2007) and M31 RV (Boschi & Munari, 2004). We note that the LRN class is likely distinct in its nature from another class of red transients, known as supernova impostors. Their progenitors have been observationally identified as dusty modestly massive stars as, for example, in the cases of SN 2008S and NGC 300 OT (Prieto et al., 2008; Berger et al., 2009; Smith et al., 2009).

Several hypotheses have been proposed to explain the nature of outbursts in different LRNe. The most common model is a merger, either of two stars or a star and a planet, with such merger-burst models being first proposed to explain V838 Mon type events (Soker & Tylenda, 2003; Tylenda & Soker, 2006). Later, Soker & Kashi (2012) also suggested that the outbursts could be powered by mass accretion onto a main-sequence star from an asymptotic giant branch star.

There were, however, initially some problems with justifying the physics behind the merger model. For example, Boschi & Munari (2004) had noticed that the M31 RV, V838 Mon, and V4332 Sgr outbursts were strongly homological and could not be explained by merger-powered outbursts that showed too much dependency on metallicity, mass, and ages. A simplistic estimate of the energy that could be available from a merger fell short by a factor of a few from the energy that was radiated away from M85 OT2006-1 (Ofek et al., 2008). Ivanova et al. (2013a) provided a further comparison between the theoretical expectations for a merger-burst model and the observations and found a number of other inconsistencies. In particular, compared to theoretical expectations, the observations implied too large of an increase in radius and luminosity, as well as too long in duration for the outburst and plateau phases. In addition, the observed velocities and extremely rapid luminosity decline were difficult to explain.

The Rosetta Stone was the V1309 Sco outburst, which was observed before, during, and after its outburst. The key was that the observations showed that the object was a contact binary prior to the outburst and a single object afterward (Tylenda et al., 2011), undoubtedly indicating a merger. On the basis of these observations, Ivanova et al. (2013a) suggested that the outburst in V1309 Sco, as well as in similar LRNe, is controlled by the recombination of the material that is ejected during the CE event. This model helps to explain the homology of the class including the plateau phase, the range of the total energy radiated away, and the differences between the velocities derived from spectra and from apparent radius expansion as well as the observed colors. The proposed link between the observations and the theoretically predicted light curve relies on how much of the material is ejected and how much kinetic energy that material carries away.

In this paper we present numerical simulations of the merger of the V1309 Sco binary, describing in full detail the models that were used to predict the light curve of V1309 Sco in Ivanova et al. (2013a). We depict our numerical methods, initial models, and assumptions in Section 3.2. To make useful predictions that would allow the linking of theory and observations, we pay special attention in Section 3.3 to how to quantify key quantities in the merger event — what is bound and unbound material and the entropy and temperature of the ejecta — as well as how to determine when the physical merger takes place. We discuss how the pre-merger binary evolves to the CE events in Section 3.4. This includes how the initial conditions (such as binary's synchronization

and the nature of the companion) could affect its orbital evolution. We also discuss whether it is possible to match the period decay observed in V1309 Sco. The details of the mass exchange and the mass loss prior to the merger are also described in Section 3.4, while the mass ejection throughout the whole process is discussed in Section 3.5. Further discussion on how to classify the unbound material and its properties at the end of the simulation are also given in Section 3.5. In Section 3.6 we discuss the symmetry of the merger product, how to get one-dimensional profiles from the three-dimensional smoothed particle hydrodynamics (SPH) code, and what the entropy and rotation profiles the merger product are.

3.2 Modelling the merger: methods and initial conditions

Observations of V1309 Sco during 2002-2008, presented in Tylenda et al. (2011), show that the object was a binary with a steadily decaying orbital period P near 1.44 days. The binary was argued to be a contact binary with the observationally derived effective temperature of $T_{\rm eff} \sim 4500$ K and luminosity of $3.0-8.6\,L_{\odot}$.

Stępień (2011) used these pre-outburst observations to determine a possible binary configuration and the evolutionary states of the progenitor binary companions. On the basis of that study, we adopted for our initial conditions a primary star mass $M_1 = 1.52\,M_{\odot}$ and a secondary star mass $M_2 = 0.16\,M_{\odot}$; the primary star is an early subgiant, while the secondary could be either a low-mass main-sequence star or a stripped giant core (essentially, a white dwarf) remaining from the previous mass transfer.

To model the merging binary, we first evolved both companions individually, using the stellar evolution code `EV/STARS` (Eggleton (1971, 1972), recently updated Glebbeek et al. 2008). The $M_1 = 1.52\,M_{\odot}$ primary was evolved until we could match the observations for temperature, luminosity, and radius (to fulfill the requirement to fill the Roche lobe for the known orbital solution). When a lower-mass companion was adopted to be a main sequence star, we evolved it using the same stellar code `EV/STARS` to the same age as the primary star. When a lower-mass companion was a white dwarf — the case when the secondary could be a stripped core of a red giant and was more massive in the beginning — we did not model the possible first mass transfer onto current primary, as that mass gain that had occurred to the current primary a long time ago during its main sequence and does not significantly affect its current subgiant structure.

At the second step, we used the one-dimensional stellar structures (obtained from the stellar evolution code) as initial conditions for three-dimensional hydrodynamical simulations. For the three-dimensional simulations, we used the code `StarSmasher`, which is based on the SPH

method; see, for example, Monaghan (1992). The code was developed by Lombardi et al. (2006), and the equations of motion have been updated by Gaburov et al. (2010; the most recent version of the code is described in Lombardi et al., 2011).

Each star was relaxed in the SPH code individually, by evolving the profile provided by the stellar code to its hydrostatic equilibrium in three dimensions. The relaxed stars then were placed in the inertial frame of a binary.

Table 3.1: Initial conditions for the performed simulations in this work.

Model	$R_{\rm RG}^{\rm ev}$	$R_{\rm RG}$	R_*	R_V	a	$P_{\rm orb}$	$f_{\rm sync}$	$f_{\rm RLOF}$	$f_{\rm RLOF}^*$	N_1	N_2	Companion Star
ps334	3.40	3.34	3.56	3.26	6.32	1.42	0.915	0.90	0.98	50161	1	Degenerate
mn351	3.40	3.51	3.70	3.52	6.32	1.42	0.000	0.97	1.02	99955	19938	Main-Sequence
pn351	3.40	3.51	3.70	3.52	6.32	1.42	0.000	0.97	1.02	99955	1	Degenerate
ps351	3.40	3.51	3.70	3.39	6.32	1.42	1.000	0.93	1.02	169831	1	Degenerate
ms376	3.65	3.76	3.96	3.63	6.55	1.50	1.000	0.97	1.05	99955	1974	Main-Sequence
ps376	3.65	3.76	3.96	3.63	6.55	1.50	1.000	0.97	1.05	99955	1	Degenerate
ms372	3.70	3.72	3.98	3.59	6.40	1.45	0.937	0.98	1.08	50161	1974	Main-Sequence
ps379	3.73	3.79	4.00	3.68	6.32	1.42	0.854	1.01	1.10	99955	1	Degenerate
pn344	3.66	3.44	3.63	3.46	6.38	1.44	0.000	0.94	0.99	99955	1	Degenerate
ps375	3.66	3.75	3.95	3.63	6.38	1.44	1.000	0.99	1.08	99955	1	Degenerate
mn344	3.66	3.44	3.63	3.46	6.38	1.44	0.000	0.94	0.99	99955	4944	Main-Sequence
ms375	3.66	3.75	3.95	3.63	6.38	1.44	1.000	0.99	1.08	99955	4944	Main-Sequence
pn319	3.39	3.19	3.38	3.20	6.38	1.44	0.000	0.87	0.92	80023	1	Degenerate

Name of the model: p stands for a point mass secondary, m stands for a main sequence secondary, n is for non-synchronized cases, s is for synchronized cases, and three digits stand for the value of the relaxed primary radius.
Radii: $R_{\rm RG}^{\rm ev}$ is the radius of the donor in the stellar code in $R_\odot$, $R_{\rm RG}$ is the radius of the donor assuming the outermost particle distance in $R_\odot$, R_* is the radius of the donor after adding 1 smoothing lengths for the outermost particle in $R_\odot$, and, R_V is the volume-equivalent radius of the donor.
Binary initial setup: a is the orbital separation in $R_\odot$, $P_{\rm orb}$ is the orbital period of an initially relaxed binary in SPH code in days, $f_{\rm sync}$ is the degree of synchronization; $f_{\rm RLOF}$ is the ratio R_V to the radius of the Roche lobe and characterizes overflow of the donor, $f_{\rm RLOF}^*$ is the ratio R_* to the radius of the Roche lobe.
Resolution: N_1 is the number of particles for the giant stars, N_2 is the number of particle for the accreting star.

In our studies, we performed 13 merger simulations. The list of all merger models with the corresponding initial conditions can be found in Table 3.1. Below we describe in detail the reasons for the diversity of the adopted initial conditions.

3.2.1 Nature of the low-mass companion and the number of SPH particles

In order to find the best scenario to the observations presented by Tylenda et al. (2011), we compared two possibilities for the nature of the low-mass secondary: a main-sequence star and a stripped core of a red giant (a degenerate companion). A degenerate companion is considered as a compact object particle in SPH, characterized by its mass and interacting only gravitationally

with other SPH particles. A main-sequence star was treated as described above, and was generally represented by several thousand SPH particles.

The number of SPH particles that represent the primary star and the secondary companion need to differ by about an order of magnitude, with more SPH particles representing the primary star. This does not correlate directly with the masses of the companions but rather with their average densities. To have comparable smoothing lengths for particles inside a main-sequence star and inside a subgiant, the number of SPH particles that describes the secondary must be much smaller than the number for the primary. If instead a small companion is represented by a comparable number of particles as the primary, then when the companion is crushed inside the primary star during the merger, computational time increases substantially.

In Table 3.1 we list the numbers of particles adopted at the start of each simulation: N_1 is for the primary star, and N_2 is for the secondary star. If $N_2 = 1$, the companion is modeled as a compact object particle.

3.2.2 The radius of the primary star

Mapping a one-dimensional star of radius $R_{\rm RG}^{\rm ev}$ into a three-dimensional star and then relaxing it in a three-dimensional code usually leads to a change of the star's radius (see also the discussion about the somewhat similar effect for polytropic stars in Renvoizé et al., 2002). Further uncertainty arises from extracting the radius of a three-dimensional star represented by particles instead of on a continuous grid. Also, in stellar codes, the stellar radius is by definition the radius of the photosphere, which cannot be resolved by our SPH code. One way to define the stellar radius in three dimensions is to find the position of the outermost particle. However, the outermost particle's kernel extends the density to $2h_{\rm out}$ from the location of this particle (see for more details Monaghan & Lattanzio, 1985), where $h_{\rm out}$ is the smoothing length of the outermost particle.

Let us consider the mapping and relaxation in more detail. When a star is first mapped into three dimensions, the outermost particles will be located at a position $R_{\rm RG}$ that is about $2h_{\rm out}$ less than $R_{\rm RG}^{\rm ev}$. While the relaxation proceeds, the position of the outermost particle can change, and this change depends on the number of particles, rotation of the star, and the method used to relax the star, for example, if artificial drag force and/or artificial viscosity are used. Hence, $R_{\rm RG}$ at the end of the relaxation can in some cases be smaller and in other cases larger than $R_{\rm RG}^{\rm ev}$. In the relaxed model, the density goes to zero at different radii R, with R being a function of the polar angle θ and azimuthal angle φ. The quantity $R_{\rm RG}+2h_{\rm out}$ is the maximum of $R(\theta,\varphi)$ over all possible θ and φ values. Because the density is sometimes zero inside the radius $R_{\rm RG}+2h_{\rm out}$ and always zero outside this radius, the radius $R_{\rm RG}+2h_{\rm out}$ is an overestimate of the average radius.

In Table 3.1 we list the primary radii found by several methods—$R_{\rm RG}^{\rm ev}$ is the radius as obtained by the one-dimensional stellar evolutionary code, $R_{\rm RG}$ is the radius after relaxation in three-dimensional SPH code determined by the outermost particle, and the effective radius $R_* \equiv R_{\rm RG} + h_{\rm out}$. In all the cases, the desired radius is within a smoothing length from either $R_{\rm RG}$ or R_*.

Arguably the most important radius is the "volume-equivalent" radius $R_{\rm V}$. In this case, we sum up over all particles m_i/ρ_i, where m_i and ρ_i are the mass and density of each particle i, to find the total volume V occupied by the particles. Then we solve for radius as $R_V = (3V/4\pi)^{1/3}$. We find that R_V tends to be on the lower boundary of our other radius estimates, very close to $R_{\rm RG}$, and never exceeding R_*. Through this paper, we use $R_{\rm V}$ as the default definition of the primary radius.

3.2.3 Orbital separation, orbital period, and the Roche lobe overflow

The binary orbital separation a, the orbital period $P_{\rm orb}$, and the ratio of the donor star radius to its Roche lobe radius that quantifies the Roche lobe overflow (RLOF), $f_{\rm RLOF} = R_{\rm V}/R_{\rm RL}$, are all closely connected. With the approximation from Eggleton (1983), in our system $R_{\rm RL} = 0.574a$.

While the observed orbital period right before the merger of V1309 Sco was measured to a quite good precision, it cannot be stated firmly if that period should be a true initial period for our merger simulations. Further, small variance of the pre-merger orbital period would not affect the outcome qualitatively; however, for our simulations $f_{\rm RLOF}$ is very influential on how fast an initial binary would decay into a complete merger.

Adopted initial values for a, $P_{\rm orb}$, and $f_{\rm RLOF}$ are listed in Table 3.1. In the adopted notation, if $f_{\rm RLOF} > 1$, the donor star is overflowing, and if $f_{\rm RLOF} < 1$, the donor is still confined in its Roche lobe. We also list $f_{\rm RLOF}^* = R_*/R_{\rm RL}$. If $f_{\rm RLOF}^* > 1$, a donor may start to lose particles because of their oscillation around their positions by a smoothing length, even if $f_{\rm RLOF} < 1$.

3.2.4 Synchronization

While stars with convective envelope are believed to be quickly tidally synchronized, it is not fully clear if a relatively fast expanding subgiant will remain tidally locked to its 10 times less massive companion. We therefore considered cases with different synchronization, from non-rotating stars to fully synchronized cases. In a fully synchronized binary, the angular velocities of both companions are the same as that of the orbit $\Omega_{*,1} = \Omega_{*,2} = \Omega_{\rm orb} = 2\pi/P_{\rm orb}$. To quantify the degree of synchronization in each simulation, we introduce $f_{\rm syn} \equiv \Omega_*/\Omega_{orb}$. The critical value $f_{\rm syn} = 1$ corresponds to a fully synchronized case, while $f_{\rm syn} = 0$ corresponds to an fully non-synchronized (irrotational) case: see Table 3.1. In our simulations, each star is first relaxed with its own spin and only then placed in a binary.

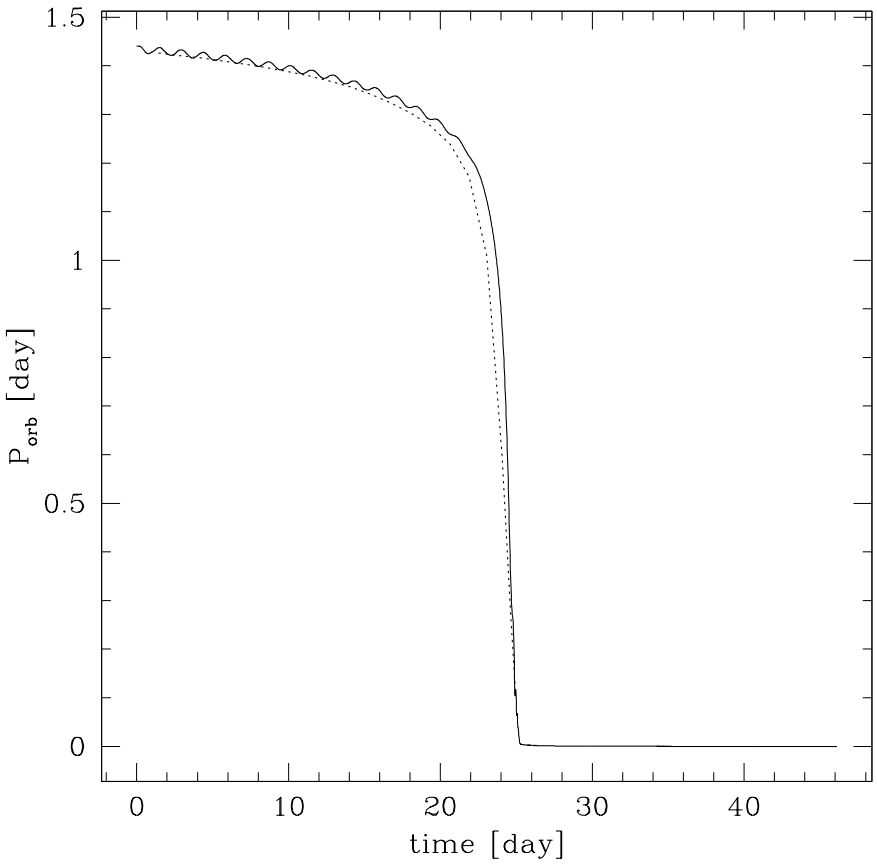

Figure 3.1: Orbital period for the simulation pn344. The instantaneous orbital period is shown with the solid line, and the apparent orbital period is shown with the dotted line.

3.3 Definitions

3.3.1 Orbital period

In a system that is not represented by only two mere point masses, but by a collection of many particles, the definition of what exactly is an orbital period is ambiguous. While several approaches can be used, we will discuss and use in this paper two of them.

First, we can find the *instantaneous* orbital period $P_{\rm orb,inst}$ at each time step. This can be done by assuming a Keplerian orbit of two bodies, where the mass of each body is the mass bound to that companion, and the separation is given by the locations of the cores of the stars (for more details, see Lombardi et al., 2006). The real orbit is slightly eccentric once orbital dissipation starts, hence the instantaneous orbital period can have an oscillatory behavior, with the period of oscillations

being equal to the real orbital period (see Figure 3.1).

We also can find *apparent* orbital period — this is how long it takes for an observer to see one complete binary revolution. It is found as follows.

1. For the calculations of the apparent orbital period only, the center of coordinates $(0,0,0)$ has been assigned to the center of mass of the more massive star, and the orbital plane is $X-Y$.

2. t_0 is the moment of time when the low-mass companion crosses $X-Z$ plane at some $(x_0,0,0)$.

3. t_1 is the moment of time when the low-mass companion has passed through all the Cartesian quadrants (made a 360^o rotation around the center of coordinates) and crosses $X-Z$ again at some $(x_1,0,0)$.

4. The apparent orbital period is then $P_{\rm orb,app} = t_1 - t_0$.

Note that this method does not intrinsically imply that two interacting bodies would necessarily have a Keplerian orbit. Because of the effects of tidal bulges, the apparent orbital period is generally smaller than instantaneous period (see, for example, Equation (7.6) in Lai et al., 1993), especially when the envelope of the primary star is starting to be significantly puffed up (see Figure 3.1). Also note that apparent period can be found for the first time only after one orbital period, as can be seen in Figure 3.1.

3.3.2 Ejecta

For the analysis of our simulations, we define as *ejecta* the unbound material of the binary system. We consider two ways to define unbound material.

Conventional definition. We say that a particle belongs to the ejecta if the total energy of that particle (the sum of kinetic, internal and gravitational energies) is positive:

$$\frac{1}{2}m_i v_i^2 + m_i\Phi_i + m_i u_i > 0. \tag{3.1}$$

Here v_i is the velocity of the particle i relative to the center of mass (fixed at the origin), m_i is the mass of the particle i, and u_i is the specific internal energy of the particle i. The potentials of each particle Φ_i and their gravitational accelerations are calculated using direct summation on NVIDIA graphics cards, softened with the usual SPH kernel as in (Hernquist & Katz 1989; for more details on implementation and justification, see Lombardi et al., 2011). The first term in the Equation ((3.1)) is the kinetic energy, the second is the gravitational potential energy, and the third is the internal energy of the particle i.

Abridged definition. We say instead that a particle corresponds to the ejecta if the sum of kinetic and gravitational energies is positive:

$$\frac{1}{2}m_i v_i^2 + m_i \Phi_i > 0. \tag{3.2}$$

Note that this definition implies that internal energy does not play a role in determining whether the matter leaves the system. By default in this paper we use the abridged definition, as discussed more below.

3.3.3 Common envelope

We recognize that the CE is formed by the expanding envelope of the primary. We define that a particle belongs to a CE if the following conditions are satisfied.

1. A particle is bound to the binary system — the sum of kinetic and gravitational energies, calculated with respect to the binary, is negative.

2. A particle is located outside of the Roche lobe of the secondary.

3. A particle is counted only if its density is above the threshold density $\rho_{\rm TR} = 10^{-6}$ g cm^{-3}.

At the start of RLOF, material from the primary streams inside the Roche lobe of the secondary, forming an accretion disk. Material transferred via the Lagrangian pont L_1 cannot be unambiguously considered as forming a CE, at least not before it starts to encompass the Roche lobe of the secondary. This motivates the second condition described above, which is taken into account only when the orbital separation exceeds the initial primary radius.

At the beginning of the binary interaction, a few low-mass surface particles are typically perturbed from the surface but remain bound to the binary for a while. However, because they have extremely low densities, they do not significantly affect the orbital evolution, nor do they form a continuous envelope. Each of those very low density particles can take a volume comparable to that of the primary star. We therefore limited the density of particles that contribute to the CE. Our threshold density implies that even if a sphere that envelops both the primary and the secondary is filled up with particles below this threshold density, the total mass of these particles will be $\lesssim 10^{-4} M_\odot$.

For each particle that satisfies the conditions above, we find the volume which that particle fills, $V_i = m_i/\rho_i$. We then sum those volumes and solve for the volume-equivalent radius of the CE, $R_{\rm CE}$.

3.3.4 Entropy

For each particle, we calculate the entropy as

$$S_i = \frac{k m_i}{m_{\rm H}\mu_i} \ln \frac{T_i^{3/2}}{\rho_i} + \frac{4}{3}\frac{m_i a T_i^3}{\rho_i} + S_{0,i}, \tag{3.3}$$

where $S_{0,i}$ is a constant and depends only on the chemical composition of the particle (see Bisnovatyi-Kogan, 2001), T_i is the temperature of the particle computed in the same way as in Lombardi et al. (2006), ρ_i is the density of the particle found by the SPH code, k is the Boltzmann's constant, $m_{\rm H}$ is the hydrogen mass, a is the radiation constant, and μ_i is the mean molecular weight. The SPH code does not evolve the chemical composition — the code conserves μ_i for each particle in the system. However, because the code uses as input realistic stellar models, particles can have different μ_i and accordingly different $S_{0,i}$. We find $S_{0,i}$ as described in Appendix 3.A.

The specific entropy of the unbound material for each time-step, $s_{\rm unb}$, can be obtained by dividing the total entropy of the ejecta by the total unbound mass, $m_{\rm unb}$, i.e.,

$$s_{\rm unb} \equiv \frac{\sum_{i,\rm unb} S_i}{\sum_{i,\rm unb} m_i} \,. \tag{3.4}$$

The summation here is only over the unbound particles.

We also define similarly the average temperature of the unbound material at each time-step as

$$\bar{T}_{\rm unb} = \frac{\sum_{i,\rm unb} T_i m_i}{\sum_{i,\rm unb} m_i} \,. \tag{3.5}$$

3.3.5 Start of the common envelope, merger, and the end of the simulations

We define several crucial phases in the evolution of our merging binary.

First, we find when the CE phase starts, $t_{\rm CE}$. For that we use the conventional definition of the common envelope — this is the moment when the companion starts to orbit inside the material that is bound to the primary core. Note that, observationally, a binary likely would not be distinguished as a binary from the moment the CE phase started.

When the companion just starts to orbit within the common envelope — the "loss of corotation" stage – the orbit still decays relatively slowly. This stage is then followed by the plunge-in phase, during which the companion quickly loses its orbital angular momentum as the orbit quickly shrinks. Assuming that this shrinkage is a half of the orbital separation during one initial orbital period, the value of $\dot{a}/a$ is about -4×10^{-6} s^{-1}. We hence adopt the definition $t_{\rm plunge}$ as the time when $\dot{a}/a = -4 \times 10^{-6}$ s^{-1}.

We say that the binary is fully merged when the separation between the cores (in other words, the separation in our instantaneous Keplerian orbital solution) is less than 0.1 $R_\odot$. This corresponds to an instantaneous orbital period

$$P_{\rm orb,inst} < 0.004 \left(\frac{M_\odot}{M_{\rm tot}}\right)^{1/2} {\rm d}, \tag{3.6}$$

where $M_{\rm tot}$ is the total mass of the binary. (Note that while the companion is already inside the primary star, the instantaneous orbital period is not a physically valid quantity but is an upper limit for the "true", or apparent, period.) For our case of $M = 1.68\ M_\odot$, this corresponds to $P_{\rm orb,inst} \lesssim 0.003$ d. Thus, the merger time, $t_{\rm merg}$, is defined as the moment when the orbital separation (or the orbital period) is less than 0.1 $R_\odot$ (or 0.003 d).

3.4 Orbital evolution prior to merger.

In this section, we analyze how the initially detached binary approaches RLOF, how it starts the CE phase, and how it merges. The "approach" phase is far from being well understood (Ivanova et al., 2013b), not least because three-dimensional simulations would usually start at RLOF. While many of our models also start close to their RLOF, we also simulate a number of cases for dozens of days or more prior the RLOF.

In Figure 3.2, we show as an example the evolution of the instantaneous orbital separation in the model pn319. This separation is compared to the radius of the envelope that is initially just the primary envelope and then transforms to the CE (the radius of that envelope is calculated as described in the §3.3.3). We can distinguish three phases.

1. The approach to RLOF and the start of the common envelope phase.
2. The loss of corotation (or *phase I* of the CE event as per adopted classification; see, e.g., Section 2 in Ivanova et al., 2013b);
3. The plunge-in with the termination (or *phase II* as per classification).

3.4.1 Why does the orbit decay and the common envelope start?

It was suggested by Darwin (1879) that if the orbital angular momentum of the binary is less than three times the spin angular momentum of its companions, the binary is dynamically unstable and the stars would fall to each other. The revised condition for the instability is that the configuration is unstable once the orbital angular momentum is less than the critical value (Hut, 1980):

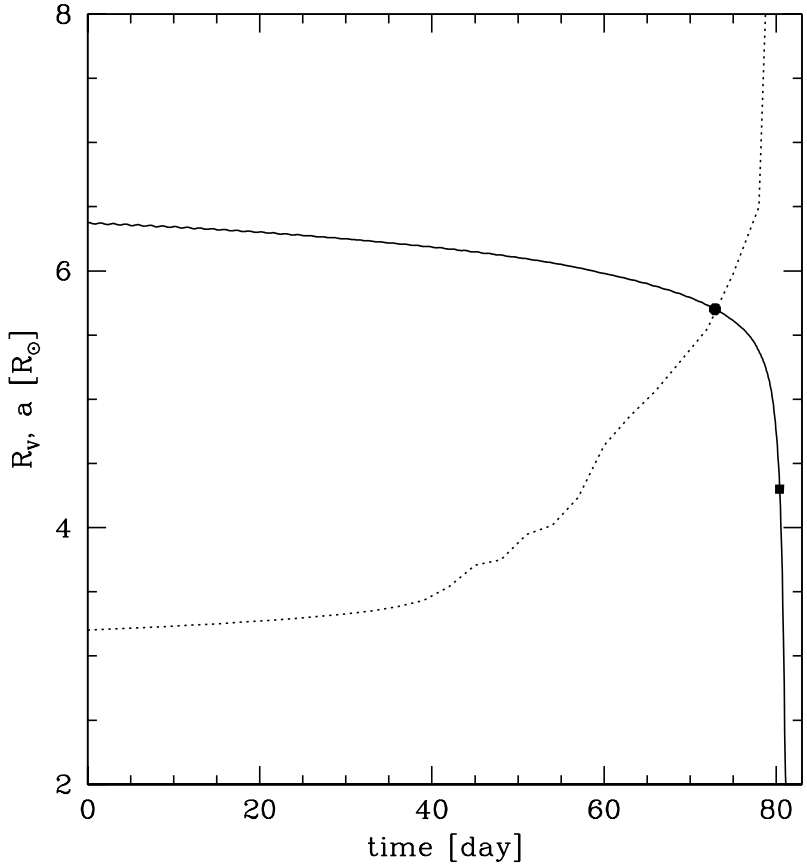

Figure 3.2: Instantaneous orbital separation (solid line) and the radius of the primary star envelope that is transitioning into the common envelope (dotted line) for the simulation pn319. The black solid circle marks the start of the common envelope, $t_{\rm CE}$, and black solid box marks the stars of the plunge-in, $t_{\rm plunge}$.

$$J_{\rm orb} < J_{\rm cr} = 3(I_1 + I_2)\,\Omega\ , \tag{3.7}$$

where I_1 and I_2 are the moments of inertia of the binary components, and Ω is the angular velocity of the synchronous rotation and revolution, $\Omega_{\rm orb} \simeq 5 \times 10^{-5}$ Hz for all our simulations. For a detached binary the orbital angular momentum, in the two-point mass approximation, is

$$J_{\rm orb} = \sqrt{G\frac{M_1^2 M_2^2}{M_1 + M_2} a(1-e^2)}, \tag{3.8}$$

where e is the eccentricity of the orbit. All our simulations start in an circular orbit, $e = 0$, and the orbital angular momentum is about the same, $J_{\rm orb} \simeq 2.8 - 2.9 \times 10^{51}\,{\rm g\,cm^2/s}$.

Table 3.2: Angular momenta and Darwin instability.

Model	I_1	$J_{\rm orb}$	$J_{\rm cr}$	$\lvert L_{\rm tot,SPH}\rvert$	$L_{\rm cr}$	$L_{\rm b}$	$L_{\rm unb}$
ps334	1.90	2.85	2.92	3.75	3.83	2.76	0.987
mn351	2.52	2.82	3.87	2.85	4.10	2.35	0.502
pn351	2.52	2.85	3.87	2.85	4.10	2.32	0.529
ps351	2.06	2.85	3.17	3.91	3.90	2.62	1.300
ms376	2.63	2.90	3.83	4.18	4.15	3.25	0.937
ps376	2.63	2.90	3.83	4.18	4.15	3.25	0.935
ms372	2.60	2.87	3.92	4.10	4.14	3.18	0.915
ps379	2.77	2.85	4.25	4.07	4.20	2.92	1.150
pn344	2.39	2.86	3.62	2.87	4.05	2.31	0.556
ps375	2.64	2.86	4.00	4.09	4.15	2.81	1.290
mn344	2.39	2.86	3.63	2.86	4.05	2.37	0.494
ms375	2.64	2.86	4.00	4.09	4.15	3.16	0.924
pn319	1.84	2.86	2.80	2.87	3.79	2.08	0.783

I_1 is the moment of inertia of the primary star in 10^{55} g cm^2,
$J_{\rm orb}$ is the orbital angular momentum of a 2 point-mass binary in 10^{51} g cm^2 s^{-1},
$J_{\rm cr}$ is the critical orbital angular momentum of a 2 point-mass binary in 10^{51} g cm^2 s^{-1},
$L_{\rm b}$ is the total angular momentum for the bound material at the end of the simulation in 10^{51} g cm^2 s^{-1},
$L_{\rm unb}$ is the total angular momentum for the unbound material at the end of the simulation in 10^{51} g cm^2 s^{-1},
$L_{\rm tot,SPH}$ is the total angular momentum for the SPH particles in 10^{51} g cm^2 s^{-1},
$L_{\rm cr}$ is critical angular momentum in 10^{51} g cm^2 s^{-1}.

We compute the moment of inertia for each of our stars individually. As all rotation is around the $z-$axis,

$$I = \sum_i m_i (x_i^2 + y_i^2), \tag{3.9}$$

where the particle coordinates x_i, and y_i are measured with respect to the center of mass of the star under consideration. The moments of inertia in our primary stars are in the range $I_1 = 1.84 - 2.77 \times 10^{55}$ g cm^2, and our non-degenerate companion has $I_2 = 1.1 \times 10^{52}$ g cm^2. For the subset of simulations where the low-mass companion is non-degenerate, the range of I_1 is narrower, $I_1 = 2.4 - 2.6 \times 10^{55}$ g cm^2. The smallest value corresponds to the simulation pn319, and the largest value corresponds to the simulation ps379. In the case of our most compact donor, in the simulation pn319, we have $J_{\rm cr} = 2.8 \times 10^{51}\,{\rm g\,cm^2/s}$ (in this simulation, $J_{\rm orb} \simeq 2.8 \times 10^{51}\,{\rm g\,cm^2/s}$), hence the system is right at the border of the Darwin instability by the criterion defined by Equation (3.7). In all other simulations, $J_{\rm cr} > J_{\rm orb}$.

The other way to express the criterion for the Darwin instability is in terms of the angular momentum: the binary is unstable once the total angular momentum is less than critical value (Hut, 1980)

$$L_{\rm cr} = 4\left[\frac{1}{27}G^2\frac{M_1^3M_2^3}{M_1+M_2}(I_1+I_2)\right]^{1/4} \tag{3.10}$$

where M_1 and M_2 are the masses of two companions (here note that a factor of G was missed in the original work). For our case,

$$L_{\rm cr} \simeq 4.07\times10^{51}\left[\frac{I_1+I_2}{2.5\times10^{55}{\rm g\ cm^2}}\right]^{1/4}{\rm g\ cm^2/s}\ , \tag{3.11}$$

The center of mass in our simulations is located at the origin. We then compute the total angular momentum of our system by using $\mathbf{L} = \mathbf{r}\times\mathbf{p}$ for each SPH particle:

$$\mathbf{L}_{\rm tot,SPH} = \sum_i \mathbf{r}_i\times(m_i\mathbf{v}_i). \tag{3.12}$$

The condition that $L_{\rm tot} < L_{\rm cr}$ was derived for the case when a binary system is in tidal equilibrium, and tidal equilibrium can be established only if coplanarity, circularity, and corotation have been established (e.g., Hut, 1980). In a binary for which corotation has not yet been established, as in some of our simulations, the instablity sets in even earlier as even more of the orbital angular momentum would have to be spent on spinning up the companions. If a donor star has overfilled its Roche lobe, the condition is also inapplicable, as the system has already become dynamically unstable. Table 3.2 shows that $L_{\rm tot,SPH} < L_{\rm cr}$ in all our simulations, except when R_* is significantly larger than the Roche lobe radius. This reconfirms that the system we consider is affected by Darwin instability.

3.4.2 Synchronization of the binary system and how the primary expands

Let us consider first the model ps351, with a synchronized donor and a degenerate companion. The simulation starts with a primary that has $f_{\rm RLOF} < 1$ but $f^*_{\rm RLOF} > 1$. Once the primary has filled the volume equivalent of its Roche lobe, its surface material starts to expand rapidly into the Roche lobe of the companion (see Figure 3.3 and the top left panel in Figure 3.4). After this moment, the primary keeps expanding, overfilling its Roche lobe. Only 2.8 days elapse between the initial RLOF and the CE formation, even though the CE does not appear very well visually distinguished in the right top panel of Figure 3.4. The time between the primary starting to expand rapidly and the moment when the CE has formed is only two initial orbital periods — this is a dynamical event.

Another synchronized model, the model ps334, is a binary where the donor was well inside of its Roche Lobe as even $f^*_{\rm RLOF} < 1$. However, this model also shows the same characteristic behavior described for the model ps351 — in particular, it shows the same rapid expansion of the

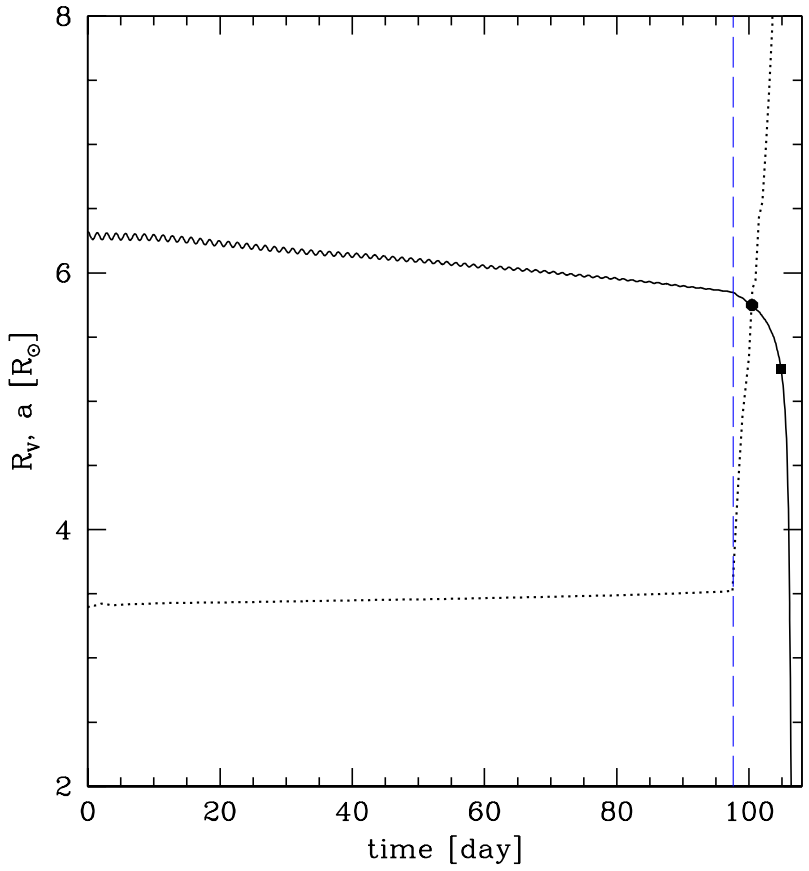

Figure 3.3: Instantaneous orbital separation (solid line) and the radius of the primary star envelope transitioning into the common envelope (dotted line) for the simulation ps351. The blue dashed line marks 97.6 days, when the sharp decay in the orbit and rapid increase in the radius of the primary start. The black solid circle marks the start of the common envelope, $t_{\rm CE}$. And black solid box marks the start of the plunge-in, $t_{\rm plunge}$.

primary once RLOF commences. We find that this fast increase of the primary radius with the CE starting soon thereafter is observed in all synchronized simulations with a degenerate companion. The same models show that most of the transferred mass is lost from the binary via the Lagrangian point L_2. The duration of mass loss through L_2 is comparatively short — e.g., in ps351 L_2 mass loss starts at about 97.7 days, just after the rapid radius increase starts; L_2 mass loss occurs only when a dynamical timescale mass transfer takes place.

Note that this rapid expansion does not necessarily lead to the drastic changes in the light curve of the outburst, which could be solely formed by the recombination wave fronts, Ivanova et al. (2013a).

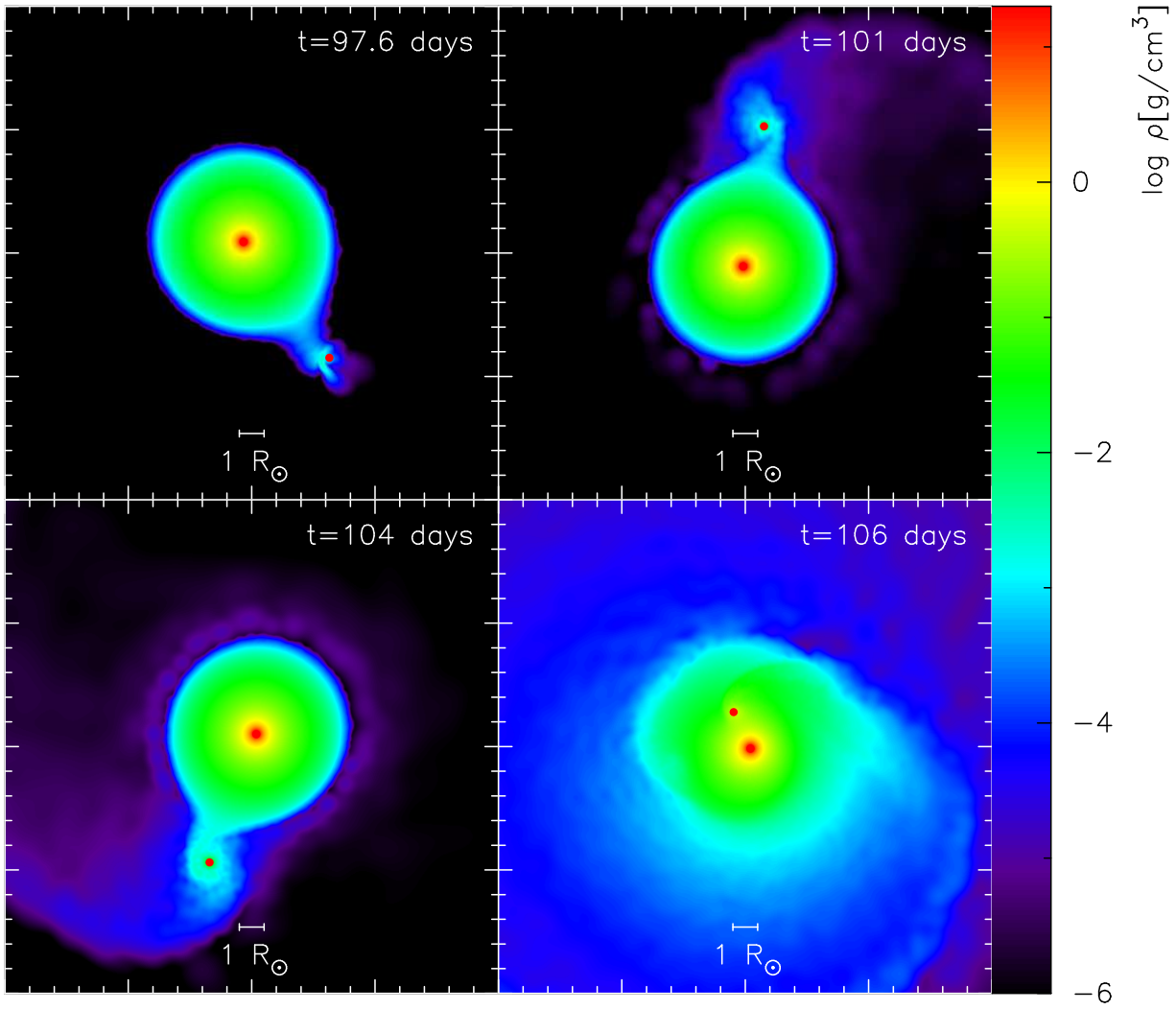

Figure 3.4: Cross-sectional slices for density in the orbital plane for the simulation ps351. The top left panel (t = 97.6 days) is when the primary has overflown its Roche lobe and more material is being transferred to the companion. The top right panel (t = 101 days) shows that the Roche lobe of the companion is overflown. The bottom left panel (t = 104 days) is for the stage when the companion spirals into the primary, while the bottom right panel (t = 106 days) shows the two orbiting cores engulfed by the envelope of the primary; after about 0.9 day the cores merge.

Now let us consider the case where the donor is not synchronized at the start of a simulation, e.g., pn319. Like ps334, this system started with the primary well within its Roche lobe, and the donor starts to transfer mass when it overflows its Roche lobe, on day 57.2 in Figure 3.2, and see also Figure 3.5. The star keeps slowly expanding while overfilling its Roche lobe, until it reaches the size of the orbit, then the fast mass transfer starts to the interior of the Roche lobe of the secondary. A slow increase in radius is observed in all non-synchronized models as well as in

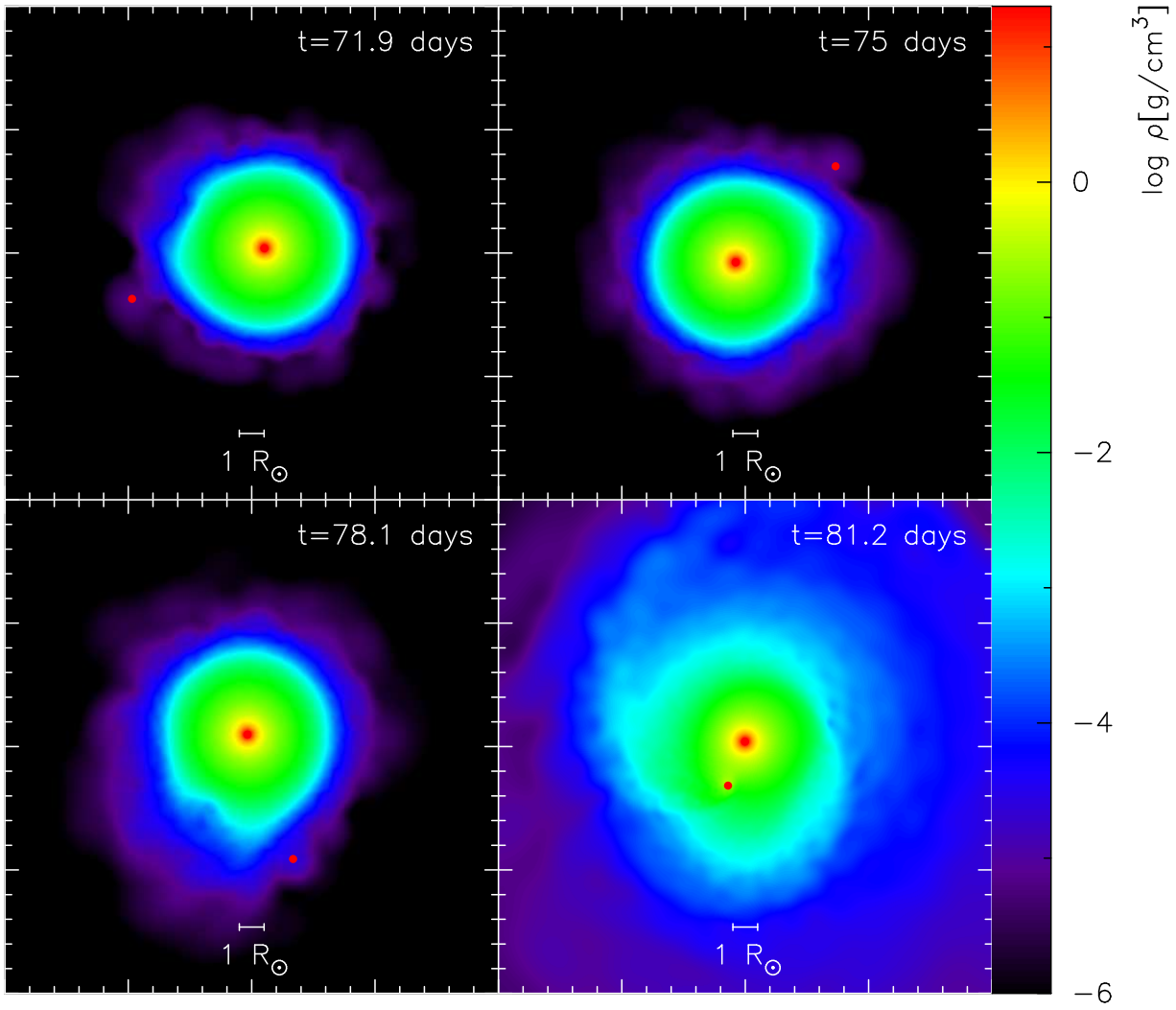

Figure 3.5: Cross-sectional slices for density in the orbital plane for the simulation pn319. The top left panel (t = 71.9 days) is when the primary has overflown its Roche lobe and more material is being passed to the companion. The top right panel (t = 75 days) shows that the Roche lobe of the companion is overflown. The bottom left panel (t = 78.1 days) is for the stage when the companion spirals into the primary, while the bottom right panel (t = 81.2 days) shows the two orbiting cores engulfed by the envelope of the primary; after about 0.5 day the cores merge.

synchronized with a non-degenerate companion. In none of the non-synchronized models do we observe any noticeable L_2 mass loss — the material from the Roche lobe of the secondary, if lost, was lost isotropically.

We speculate that this slow expansion of the primary star towards the orbit could be a numerical artifact related to SPH particles oscillations around their positions by a smoothing length h (about 5% of the radius for surface particles). For the most of the simulated models, it implies that the

Table 3.3: Important times.

Model	$t_{\rm CE}$	$t_{\rm plunge}$	$t_{\rm merg}$	$t_{\rm end}$
ps334	154.91	157.10	158.4	283
mn351	10.40	13.42	13.6	15
pn351	11.80	13.08	14.7	30
ps351	100.45	104.85	106.9	156
ms376	26.9	29.02	31.2	43
ps376	39.72	42.58	44.9	61
ms372	11.2	12.80	15.1	23
ps379	3.30	6.28	7.7	55
pn344	21.40	24.01	25.6	46
ps375	8.90	12.74	14.1	36
mn344	20.50	24.22	24.4	31
ms375	9.66	13.50	13.8	20
pn319	72.90	80.40	81.7	115

$t_{\rm CE}$ is when the low-mass companion is engulfed by the envelope of the more massive star, $t_{\rm plunge}$ is when the low-mass companion is plunged into the donor, $t_{\rm merg}$ is when the merger took place and $t_{\rm end}$ is last moment in the simulations. The times are in days.

primary star would find itself often in "instantaneous" RLOF; this unavoidably speeds up the start of the CE phase. On the other hand, the oscillations by 5% of the stellar radius are comparable to the scale over which convective eddy exists. In giants that have surface gravity close to zero, the surface not smooth, the convective plumes, which are comparable in size to the giant radius, would rise above the conventionally defined surface (e.g., see Chiavassa et al., 2011).

3.4.3 Synchronization of the binary system and the timescale

To understand how the initial conditions affect the pre-merger evolution, we first consider the effect of synchronization. There are several pairs of simulations that have the same initial conditions except for $f_{\rm sync}$.

1. pn351 and ps351 both have primaries at about RLOF (see also Figure 3.6).
2. ps334 and pn319 have almost identical conditions, and both primaries are well within their RLOF.
3. Two pairs, pn344–ps375 and mn344–ms375, are harder to analyze cleanly. In each pair, the relaxed primary has significant RLOF in the case of a synchronized binary, while the non-synchronized binary is well within its Roche lobe.

It can be seen that if the relaxed stars are within their Roche lobes ($f^*_{\rm RLOF} < 1$), then the synchronized binary, as expected, has a slower period decay, with up to a 10 times difference (see table

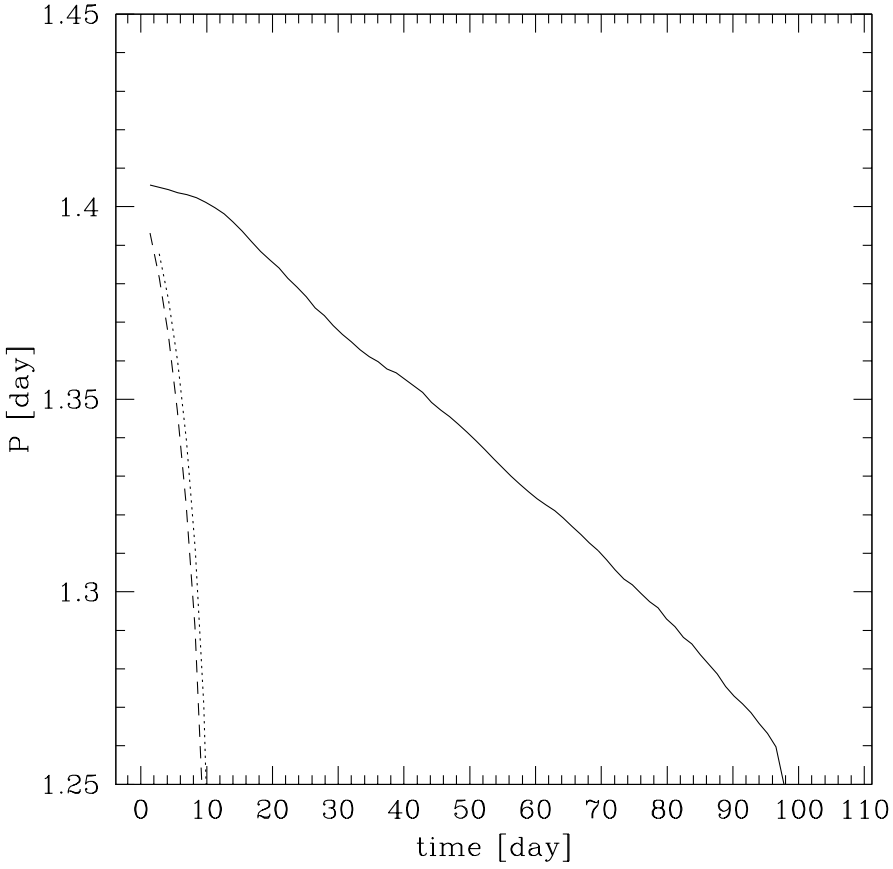

Figure 3.6: Evolution of the orbital period for the simulations pn351 (dotted), ps351 (solid), and mn351 (dashed).

3.3 data for the simulations in pairs 1 and 2 above). Being an RLOF binary cancels this effect, and in case 3 — synchronized but overflowing their Roche lobe primaries with $f^*_{\rm RLOF} > 1$ — results in a faster merger.

We conclude that the synchronization prior to Roche lobe overflow leads to a slower period decay.

3.4.4 Companion's nature and the timescale

We consider the effect of the companion's nature, degenerate (represented by a point) versus non-degenerate (represented by a group of particles), by comparing the following pairs.

1. pn344 and mn344 (primaries are well within their Roche lobes, $f^*_{\rm RLOF} < 1$).

2. pn351 and mn351 ($f_{\rm RLOF} < 1$ but $f^*_{\rm RLOF} = 1.02$ — primaries have some particles going be-

yond their Roche lobes).

3. ps376 and ms376 ($f^*_{\rm RLOF} = 1.05$).

4. ps375 and ms375 (primaries are near their Roche lobe limit with $f_{\rm RLOF} = 0.99$ and $f^*_{\rm RLOF} = 1.08$).

Unlike the comparison in Section 3.4.3, the degree of RLOF in the primary is the same within each pair, as each member of the pair has the same synchronization.

In binaries where the primary is well within its Roche lobe (case 1) or is just at its Roche lobe limit (case 2), the merger time only weakly depends on the nature of the companion, differing only by about a day (see Table 3.3). In cases of larger primaries that also noticeably overfill their Roche lobes (cases 3 and 4), a non-degenerate companion leads to a shorter merger timescale, by up to three times. We can conclude that a non-degenerate companion may affect the orbital decay timescale but likely not as significantly as the synchronization of companions.

3.4.5 Can we match the observations?

Tylenda et al. (2011) found that they can fit V1309 Sco pre-outburst observations with an exponential period decay, as a function of time t:

$$P_{\rm obs} = P_0 \exp\left(\frac{b_0}{t - t_0}\right) , \tag{3.13}$$

where $P_0 = 1.4456$ (the period in days), $b_0 = 15.29$ and $t_0 = 2455233.5$ was a Julian Date at several hundred days after the merger took place. The binary period decay was traced in observations for about 2000 days before the binary was seen last as such. Numerical simulations of a binary that is almost at its RLOF and for the duration of thousands of its orbital periods are well beyond both numerical capabilities of our code and the computational time demand. In our longest simulation, the binary spent 158 days before it merged. A similarly short interval prior to merger has only four observational data points for periods, where each of those four points was derived using 50 observations; the errors in the period determination for those four points were $0.002 - 0.008$ day. We therefore can attempt to qualitatively compare only the tail of the decay, while assuming that the same fit is valid for the tail of observations as for the whole set.

For each simulation that started with $f_{\rm RLOF} < 1$, we trace the apparent orbital period decay from the start of the simulation until the start of the CE phase, $t_{\rm CE}$. We fit this orbital evolution to the exponential decay described by Equation (3.13) in order to find best-fit values for P_0 and b_0; we also look at how quickly the system completes the merger, $t_{\rm merg}$. The results for all the simulations that have been evolving for 20 days or more before the binary has merged are shown in Table 3.4.

Table 3.4: Fit parameters for simulations with merger times larger than 20 days.

Model	P_0	b_0	t_0	*RSS*	ν
ps334	1.91 ± 0.02	135 ± 10	440 ± 10	114	85
ps351	2.17 ± 0.08	202 ± 30	470 ± 30	169	69
ms376	1.537 ± 0.003	1.52 ± 0.07	36.0 ± 0.4	30	16
ps376	1.84 ± 0.04	35 ± 6	159 ± 10	10	21
pn344	1.506 ± 0.002	1.49 ± 0.03	28.3 ± 0.1	6	12
mn344	1.500 ± 0.001	1.33 ± 0.02	26.8 ± 0.1	3	11
pn319	1.547 ± 0.002	7.8 ± 0.1	105.5 ± 0.5	22	46

P_0, b_0 and t_0 are the fitted parameters for the function given by the eq. (3.13) (in days);
RSS is the residual sum of squares in units of 10^{-6}.
$\nu = N - n$ is the number of degrees of freedom, where N is number of observations and n is the number of fitted parameters. Only models with $\nu > 10$ are shown.

Equation (3.13) implies that an exponential orbital decay takes place if b_0 is much smaller than t_0. We find that the models ms376, pn344, mn344 and pn319 have the period decay shaped similarly to that found by Tylenda et al. (2011) — Table 3.4 shows that on those simulations t_0 is much larger that b_0. On the other hand, for a monotonical period decay, b_0 should be of the order of t_0. In the models ps334, ps351, and ps376, t_0 is about 3 times larger than b_0, and the decay in those simulations is almost linear with time, unlike in the observations of V1309 Sco.

In Figure 3.6 we show examples of the linear and exponential orbital decays in the models ps351, pn351 and mn351 (note that pn351 and mn351 did not have enough pre-merger models to deduce values of b_0 and t_0). Note that in the simulation ps351, the orbital period decay is a linear decay for about 90 days, with an abrupt decline thereafter.

In Figure 3.7 we show two fits for Equation (3.13) for the simulation pn319. One fit uses values from Tylenda et al. (2011), and another uses fit parameters as in Table 3.1. The difference between the results is marginal and within the error bar from observations (≤ 0.01 day). We conclude that the period decay of this model can be fit with about the same shape as the period decay found for V1309 Sco.

We conclude that even though synchronized systems with a degenerate companion have a longer period decay time, they do not exhibit the *shape* of the decay observed in the case of V1309 Sco. This shape can be explained by either (1) a nonsynchronized binary with a degenerate companion or (2) a binary with a main-sequence companion (either synchronized or unsynchronized).

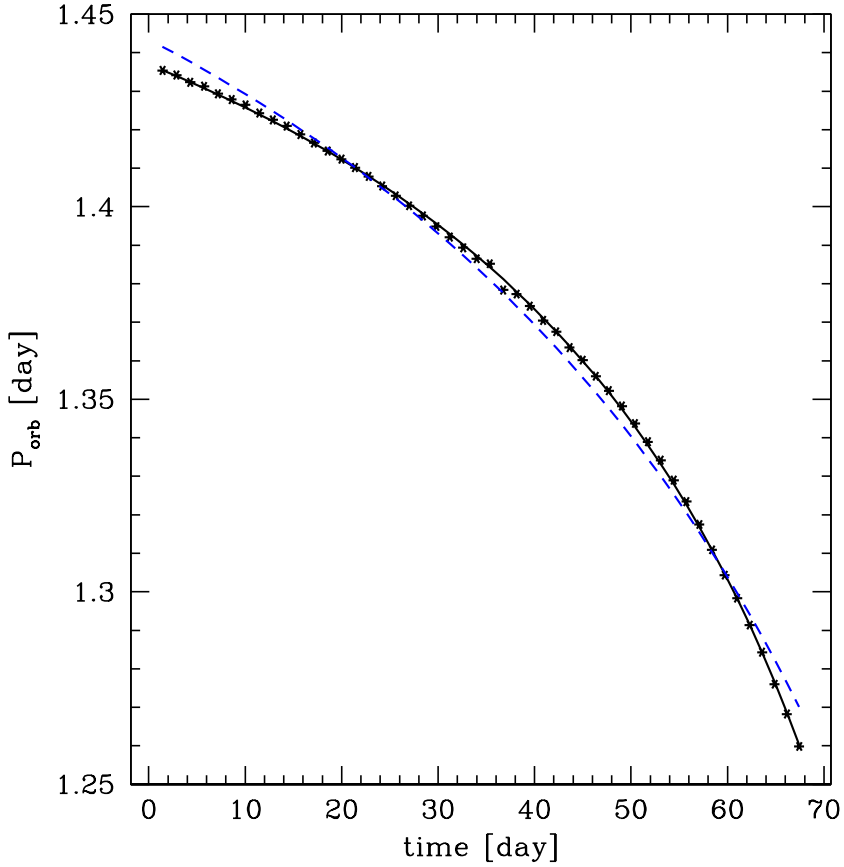

Figure 3.7: Evolution of the orbital period for the simulations pn319 (the dots). The solid line is the best fit with $P_0 = 1.5472$ days, $t_0 = 105.458$ days, and $b_0 = 7.7985$ days, while the blue dashed line is the fit with $P_0 = 1.6242$ days, $t_0 = 129.596$ days, and $b_0 = 15.29$ days.

3.5 Ejecta

3.5.1 Which material is unbound?

It has been proposed in Ivanova et al. (2013a) that the outburst of V1309 Sco was controlled by the recombination of material ejected during the binary merger. The total energy of the outburst, during the recombination, would therefore depend on the amount and speed of the ejected material. To reproduce the light curve of the outburst, one needs then the ejecta mass loss rate as a function of time. In this section we concentrate on the details of how to recover the mass loss rate with time. This task requires the identification of the ejected material *right at the moment when it starts its initial escape*.

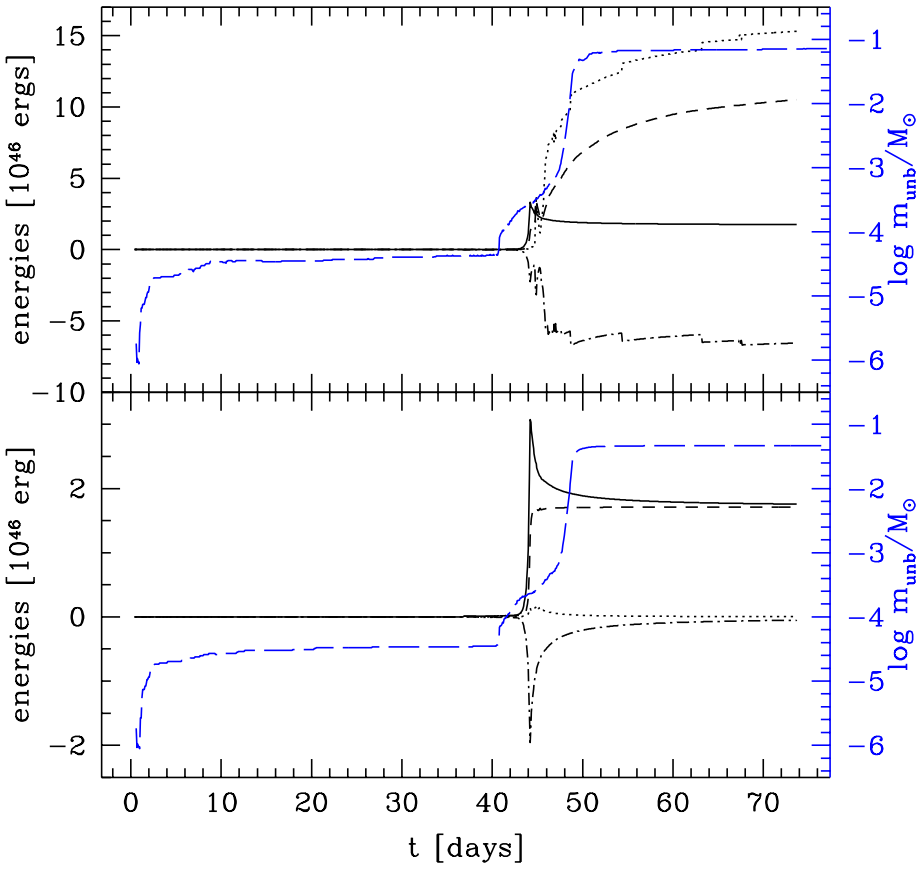

Figure 3.8: Energies in the ejecta in the simulation ps376 — the kinetic energy (solid line), the internal energy (dotted line), the potential energy (dash-dotted line), and the total energy (dashed line); whilst the blue long-dashed line shows the evolution of the ejecta mass. On the top panel the ejected material is determined using the criterion (3.1), and on the bottom panel the ejected material is determined using the criterion (3.2).

In Section 3.3.2 we have discussed two ways to define the unbound material. Let us consider how both definitions work in the case of some particular example, the simulation ps376. In Figure 3.8 we show the evolution of the kinetic, potential, internal, and total energies for the material that was classified as ejecta, using the criteria given by Equations (3.1) and (3.2).

In the "conventional" case, the internal energy of all "ejected" material greatly exceeds its kinetic energy (see Figure 3.8). As the simulation proceeds, the internal energy stays at a large value. This is not what would be expected in a case of an adiabatic expansion anticipated for our ejected and expanding material.

With the "abridged" definition, the internal energy decreases with time as expected for an adia-

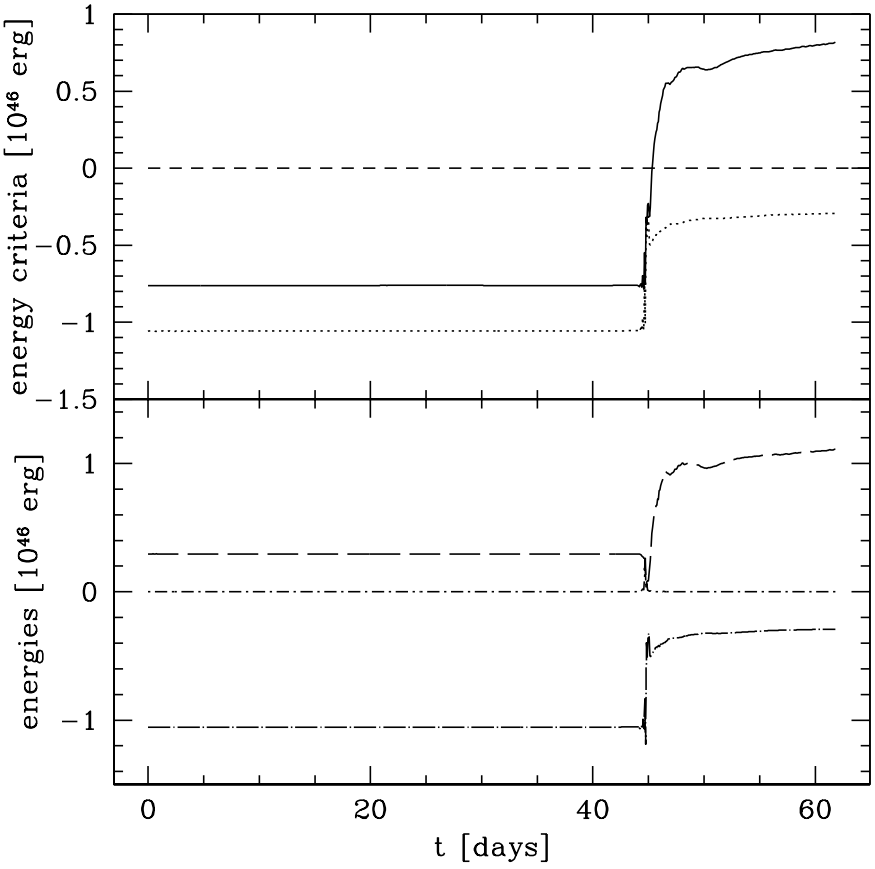

Figure 3.9: Top panel: how two criteria on determining unboundedness work for the particle 52287 in the simulation ps376 (solid line denotes the conventional definition, and the dotted line denotes the abridged criterion). Bottom panel: the kinetic (dotted-dashed line), potential (long dotted-dashed line), and internal (long dashed line) energies for the same particle.

batic expansion. In this case the kinetic energy dominates the energy of the ejecta by the end of the simulation, even though values of the kinetic energy in the ejected material by both definitions are similar.

A careful check shows that the difference between the two methods is primarily due to several particles located around the low-mass companion. The internal energy of these shock-heated particles is high, but their relative velocity to the center of mass is very low.

Figure 3.9 compares how both criteria work for the particle 52287 in the simulation ps376. It can be clearly seen that the internal energy of this particle at all time is much larger than its kinetic energy. After the binary merges, the "conventional" criterion implies that this particle is unbound to the system, while the "abridged" criterion indicates that the particles is bound.

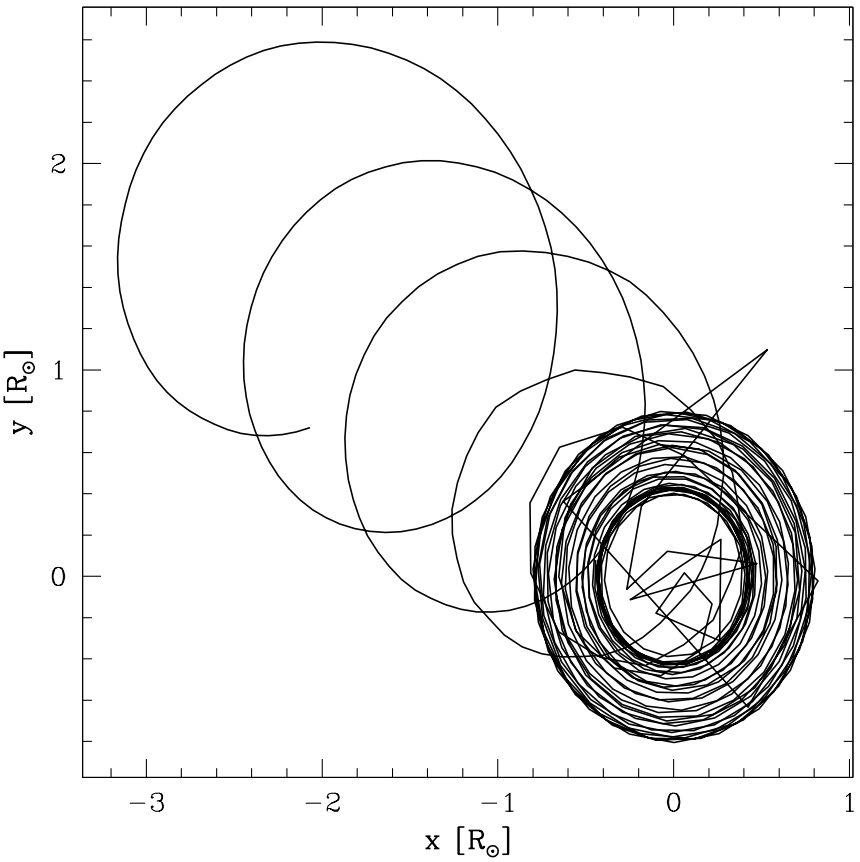

Figure 3.10: Trajectory of the particle 52287 in the simulation ps376 projected onto the orbital plane. The particle finishes near $(x, y) = (-2.1, 0.7)$ at the end of the simulation.

In Figure 3.10 we show the positions of the particle 52287 projected onto the orbital plane. It can be seen that this particle remains in the vicinity of the merger product, its orbit becomes wider after the merger, but its path follows the movement of the center of mass of the merger product until the end of the simulation. We find that this particle (among other similarly heated particles) is unable to transfer its heat to neighboring SPH particles on the timescale of the simulation. Therefore, we chose to use the "abridged" criterion in order to classify all the particles with this behavior as bound particles.

3.5.2 Mass outbursts

We found that the ejection of stellar material usually proceeds in several mass outbursts, when the mass loss rate increases significantly for short periods of time and then drops again. To identify and distinguish these mass-ejection outbursts, we compute the change in the mass of the ejecta with

Table 3.5: Mass, duration and kinetic energy of each episode of mass for each simulation.

Model	$m^b_{\rm unb}$	$m^d_{\rm unb}$	$m^a_{\rm unb}$	t^b	t^d	t^a	$E^b_{\rm kin,\infty}$	$E^d_{\rm kin,\infty}$	$E^a_{\rm kin,\infty}$	$E^b_{\rm kin,max}$	$E^d_{\rm kin,max}$	$E^a_{\rm kin,max}$
ps334	–	0.0405	0.0048	–	4.02	1.15	–	1.62	0.08	–	5.91	0.15
mn351	0.0100	0.0280	–	0.97	2.63	–	0.53	0.95	–	1.40	1.34	–
pn351	0.0115	0.0160	0.0123	1.08	1.44	5.92	0.59	0.55	0.14	1.69	1.04	0.23
ps351	–	0.0467	0.0227	–	3.80	5.50	–	1.85	0.24	–	6.19	0.45
ms376	0.0321	0.0123	–	1.90	1.6	–	1.08	0.25	–	4.06	0.40	–
ps376	–	0.0409	–	–	2.28	–	–	1.54	–	–	5.40	–
ms372	0.0317	0.0119	–	2.10	1.50	–	1.17	0.32	–	4.27	0.43	–
ps379	–	0.0410	0.0255	–	3.70	3.10	–	1.65	0.38	–	6.27	0.65
pn344	0.0128	0.0165	0.0085	1.30	1.25	4.38	0.64	0.56	0.09	2.13	1.08	0.16
ps375	–	0.0412	0.0384	–	2.70	4.30	–	1.61	0.56	–	6.12	0.90
mn344	0.0108	0.0237	–	1.00	2.00	–	0.52	0.62	–	1.52	1.09	–
ms375	0.0320	0.0130	–	2.00	1.40	–	1.22	0.33	–	4.45	0.44	–
pn319	0.0147	0.0199	0.0209	1.20	2.40	8.40	0.67	0.73	0.31	2.19	1.33	0.51

$m_{\rm unb}$, t, $E_{\rm kin,\infty}$ and $E_{\rm kin,max}$ are the mass ejecta in $M_\odot$, duration in days and kinetic energy at infinity in 10^{46} ergs and maximum kinetic energy at the moment of ejection of each mass ejection. The superscript a implies "after the merger", and the subscript b implies "before the merger" while d implies "during the merger".

time, $\dot{m}_{\rm unb} \equiv dm_{\rm unb}/dt$. For example, in Figure 3.11 we can distinguish three episodes of the mass outbursts, each corresponding to a spike in the mass-ejecta rate $\dot{m}_{\rm unb}$. The first peak corresponds to the mass outburst *before* the merger (during the plunge-in), the second peak correspond to the mass outburst *during* the merger, while the last one corresponds to the mass outburst *after* the merger has been completed. Recall we defined *merger* as the time when $a_{\rm orb} < 0.1 R_\odot$; see Section 3.3.5.

A summary of the mass outbursts in different simulations is presented in Table 3.5. We find that the mass-outburst before the merger is absent in synchronized system with a degenerate donor — the same systems that feature rapid radius expansion and L_2 mass loss. In contrast, all non-synchronized simulations with a degenerate donor show all three outbursts mentioned above. Binaries with a non-degenerate donor do not produce a mass outburst after the merger; instead they always have two episodes of mass ejection independent of the initial synchronization. The duration of all episodes is on the order of the dynamical timescale of the system. Most of the ejected material is ejected during the mass outbursts, but not all (see also Table 3.6 for the total mass of the material to infinity).

Compared to the determination of the mass of the ejecta, proper values of the ejecta kinetic energy *exactly* at the moment when the material was ejected are harder to determine. This is because the ejection is a continuous process, and each mass outburst can take from a few hours up to several days. At each time-step we have some particles that are ejected right then, but other particles were ejected during the previous time-step, and have already started their travel to infinity, so they already have lost some initial kinetic energy after overcoming partially the potential well. An example can be seen in Figure 3.12 — the mass of each outburst loses its kinetic energy with

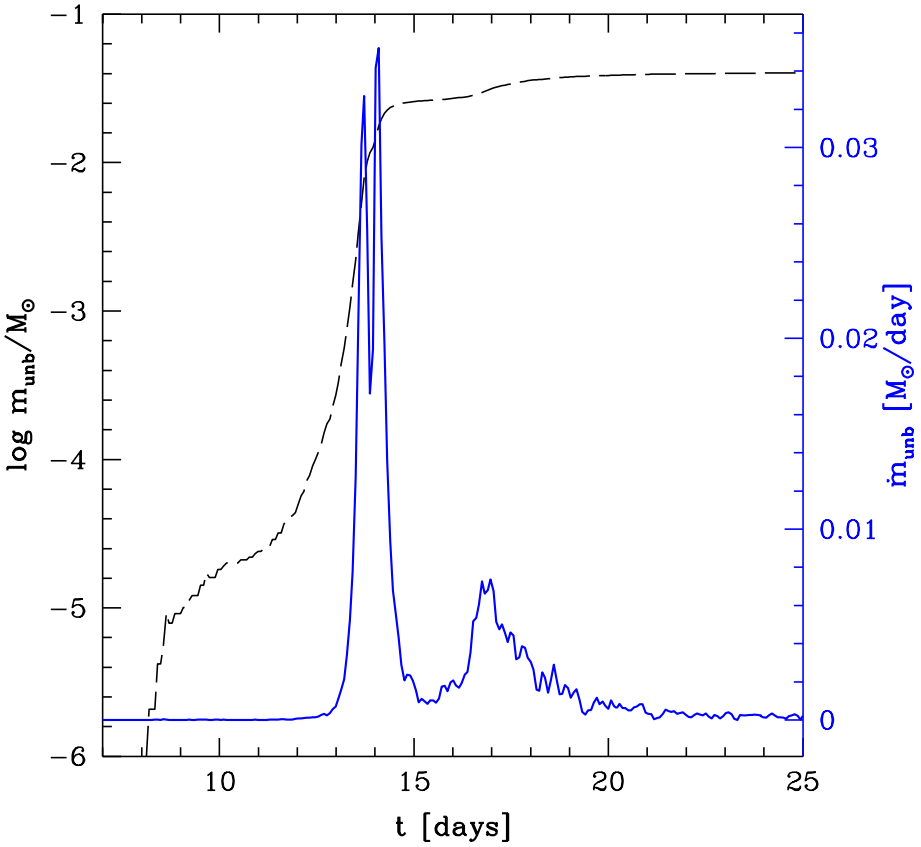

Figure 3.11: Mass of the ejecta (black dashed line) and its derivative (blue solid line) as functions of time, in the simulation pn351. Each peak shown in the plot corresponds to one episode of the mass outburst.

time until it approaches a constant value at infinity. In Table 3.5 we provide the kinetic energy that all particles contributing to each mass outburst had at the moment they were identified as unbound for first time. We anticipate that those values are lower estimates for the kinetic energy of the ejecta, as velocities inferred from these energies do not greatly exceed the escape velocities. However, the relative values between the outbursts is more meaningful and shows that ejecta from the initial outburst usually have a higher velocity than those from the second or third outburst.

It was shown that the observed light curve in V1309 Sco could be reconstructed with two mass outbursts of 0.02 and 0.04 $M_{\odot}$ mass loss, with corresponding kinetic energies for each outburst as 0.9×10^{46} erg and 0.75×10^{46} erg (Ivanova et al., 2013a). These values are within the range of the obtained values in our simulations (see Table 3.5), with non-degenerate and non-synchronized systems being the closest match.

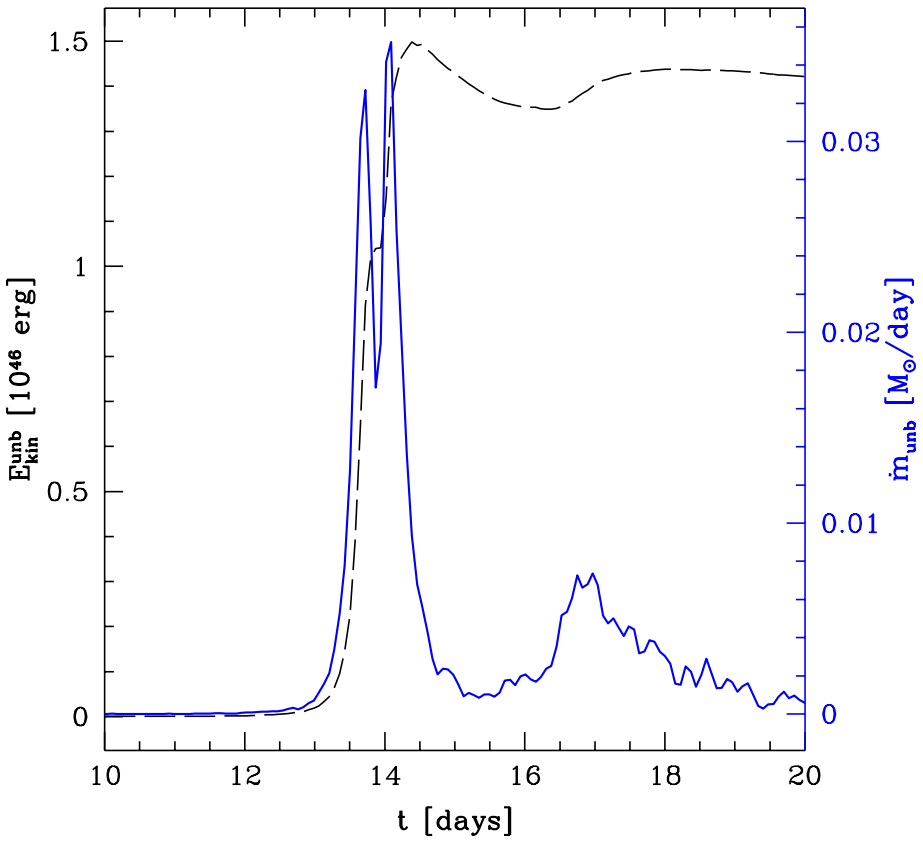

Figure 3.12: Kinetic energy of the ejecta (black dashed line) and $\dot{m}_{\rm unb}$ (blue solid line) in the simulation pn351.

3.5.3 Properties of the ejected material at the infinity

Velocity of the ejecta

The energy formalism commonly used to evaluate an outcome of a CE event assumes that the material is ejected with energy just sufficient to move that material to infinity and that its kinetic energy there is zero and hence does not need to be taken into account in the energy balance. We find that the kinetic energy of the ejected material is significantly non-negligible at infinity; moreover, it is not much different than at the moment it was just ejected (see Figure 3.13). Since at the onset of the simulations the two stars are considered point masses, we can compute the initial orbital energy by simply using $E_{\rm orb} = GM_1M_2/(2a_{\rm orb})$, where $M_1 = 1.52\,M_\odot$ and $M_2 = 0.16\,M_\odot$, and $a_{\rm orb} \simeq 6.3\,R_\odot$ (see Table 3.1). Hence, $E_{\rm orb} \sim 7.3 \times 10^{46}$ erg, which can be compared with the kinetic energy given by Table 3.6. We can conclude that the ejecta takes away up to one-third of the initial orbital energy.

Table 3.6: Velocities at infinity.

Model	$v_{\rm esc}^{\rm ini}$	$v_{\rm esc,bin}^{\rm ini}$	$m_{\rm tot}^{\rm unb}$	$E_{\rm kin,\infty}^{\rm unb}$	$v_{\infty}^{\rm unb}$	$j_{\rm unb}/j_{\rm ini}$
ps334	404	319	0.0549	1.94	189	8.06
mn351	396	319	0.0382	1.51	199	7.74
pn351	396	319	0.0415	1.30	177	7.50
ps351	398	319	0.0800	2.28	169	6.96
ms376	383	313	0.0470	1.46	177	8.01
ps376	383	313	0.0466	1.75	194	8.08
ms372	382	317	0.0464	1.55	183	8.10
ps379	381	319	0.0808	2.26	168	5.88
pn344	400	317	0.0415	1.33	180	7.86
ps375	383	317	0.0859	2.40	168	6.16
mn344	400	317	0.0362	1.21	183	8.01
ms375	383	317	0.0479	1.65	186	7.92
pn319	415	317	0.0583	1.80	176	7.88

$v_{\rm esc}^{\rm ini}$ is the escape velocity from the surface of the initial primary, $v_{\rm esc,bin}^{\rm ini}$ is the escape velocity from the initial binary (using a), $m_{\rm tot}^{\rm unb}$ is the total unbound mass in $M_{\odot}$, $E_{\rm kin,\infty}^{\rm unb}$ is kinetic energy at infinity in 10^{46} ergs, $v_{\infty}^{\rm unb}$ is the velocity of the ejecta at infinity, $j_{\rm unb}/j_{\rm ini}$ is the ratio between the specific unbound angular momentum and specific initial angular momentum. All velocities are in km/s.

Note that we did not use the CE energy formalism anywhere in our calculations.

In Table 3.6 we show the velocities of the ejected material at infinity, $v_{\infty}^{\rm unb}$, and they are as large as 42% to 51% of the initial escape velocity from the surface of a donor. The velocities we obtain are well consistent with the average velocities of the ejecta from the observations, 160–180 km s^{-1} (Mason et al., 2010). We note that, as with the velocity at the moment of the ejection, at infinity there is also no single-valued velocity for all the ejected material, and ejecta speeds are usually significantly higher at the start of the mass loss, for the outer layers, and smaller for material ejected after the merger is complete.

Angular momentum

The total angular momentum carried away by the ejecta is between 17% and 33% of the initial total angular momentum of the binary, even though it is taken away by an extremely small amount of the material (see Table 3.2). The specific angular momentum of the ejected material exceeds the initial specific angular momentum by a factor of 5.8–8.1 (see Table 3.6). The relative fraction of the total angular momentum that is carried away with the ejecta is highest in the simulations with a synchronized binary and a degenerate donor and smallest in non-synchronized binaries with a non-degenerate donor.

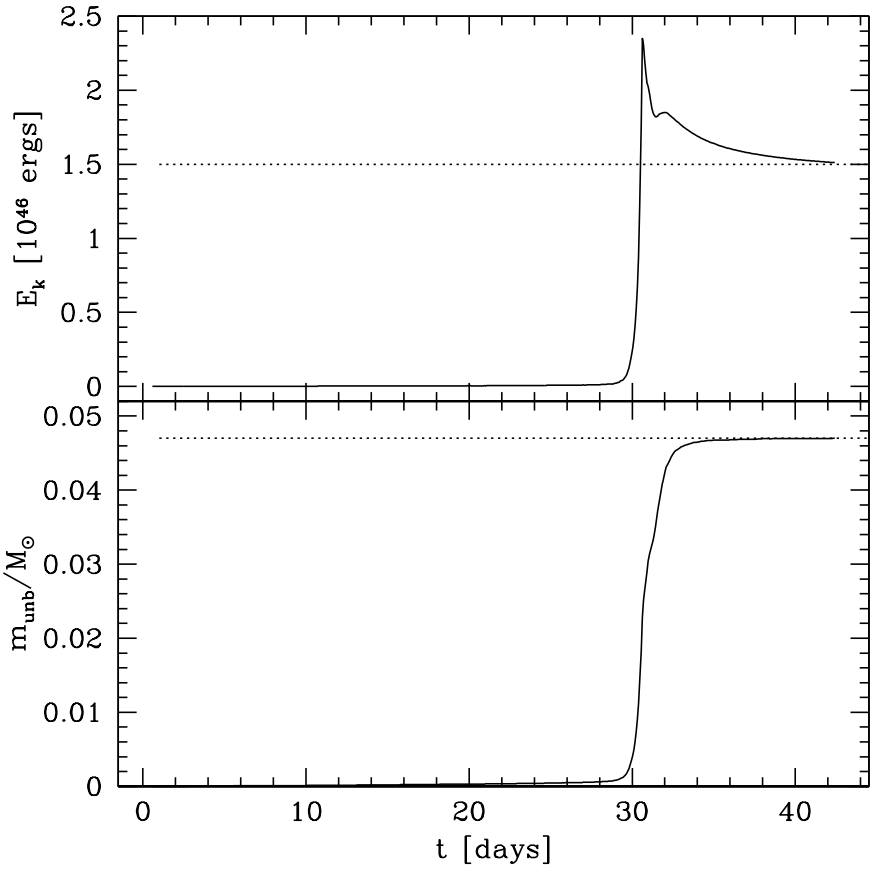

Figure 3.13: Kinetic energy (top panel) and mass (bottom panel) of the unbound material in the simulation ms376. The dotted lines indicate the final values at infinity.

The entropy and temperature of the ejecta

The specific entropy of the material in the envelope of the unperturbed donor, $s/(kN_{\rm A})$, is about 22 mol g^{-1}. The initial mass loss starts when the CE has not yet formed but the ejected material is already shock-heated, with its specific entropy increased by about 20 mol g^{-1} (see Figure 3.14). Once the CE forms and the companion starts its spiral-in, the ejected material is the most shock-heated throughout the complete event — its specific entropy exceeds its initial value by up to 50 mol g^{-1}. As the companion continues to plunge-in, more of the envelope of the donor gets ejected, but this material is already less shock-heated, and overall the entropy of the ejecta decreases and reaches a minimum — the big dip that takes place at about $t_{\rm merg}$. As the merger is completed and the ejected material evolves adiabatically, its entropy remains constant, at a value about 8 mol g^{-1} higher than the initial value of the specific entropy in the donor. This general behavior is characteristic for all the simulations, while the final and maximum entropy values varying somewhat from case to case.

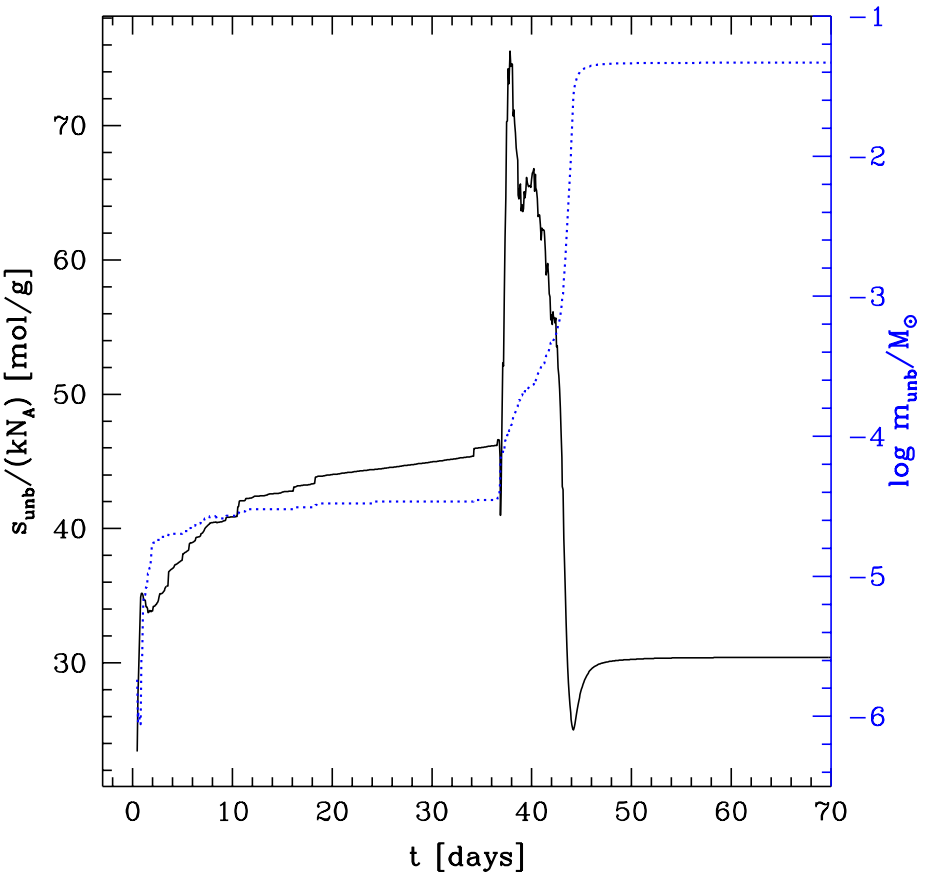

Figure 3.14: Evolution of the specific entropy (black solid line) and mass (blue dotted line) of the ejecta in simulation ps376.

Figure 3.15 shows the evolution of the average temperature for the unbound material, in the same simulation ps376 as for the specific entropy discussed above. The first spike in the simulation takes place at the first contact between the low-mass companion and the surface of the giant and involves only a small quantity of ejected material. The second spike corresponds to the first episode of the mass ejection — when the CE gets formed. The third spike is due to the shock-heating during the merger. After the merger is completed and there are no more mass outbursts, the ejecta temperature demonstrates adiabatic cooling. In our simulations, the equation of state does not include ionization. In a real merger, the recombination process will undoubtedly change the temperature evolution (Kasen & Ramirez-Ruiz, 2010; Ivanova et al., 2013a).

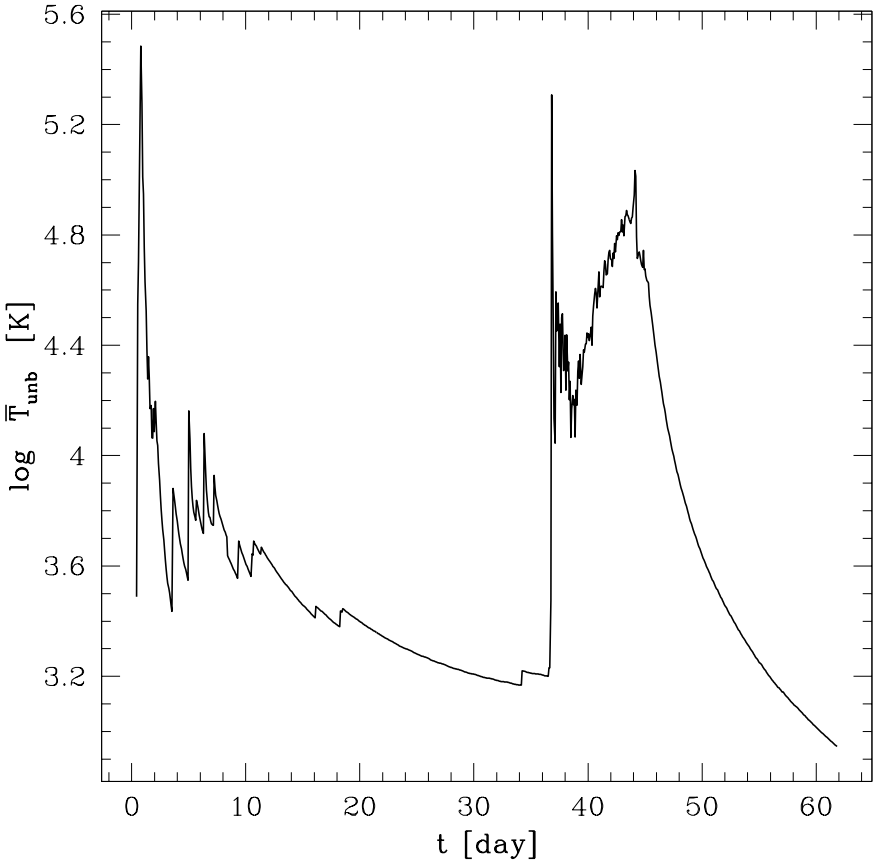

Figure 3.15: Average temperature of the unbound material (simulation ps376).

3.5.4 Ejecta appearance

The ejection proceeds in mass outbursts. If outbursts are well separated by a minimum in the rate of the mass loss, they might be distinguished even when the ejecta is very far from the merged object. Indeed, in all our simulations with a synchronized binary, the ejecta appears in the form of a ring. In Figure 3.16 we show the formation of a typical ring structure from the initially spiral-shaped outflow. In the case shown, the outer ring is formed by the material from the mass outburst during the merger, and the inner, less pronounced ring, by the last mass outburst. We do not see a ring or another well distinguished structure formation in simulations with a non-synchronized binary — there, the ejecta is rather isotropic, with many "clumps."

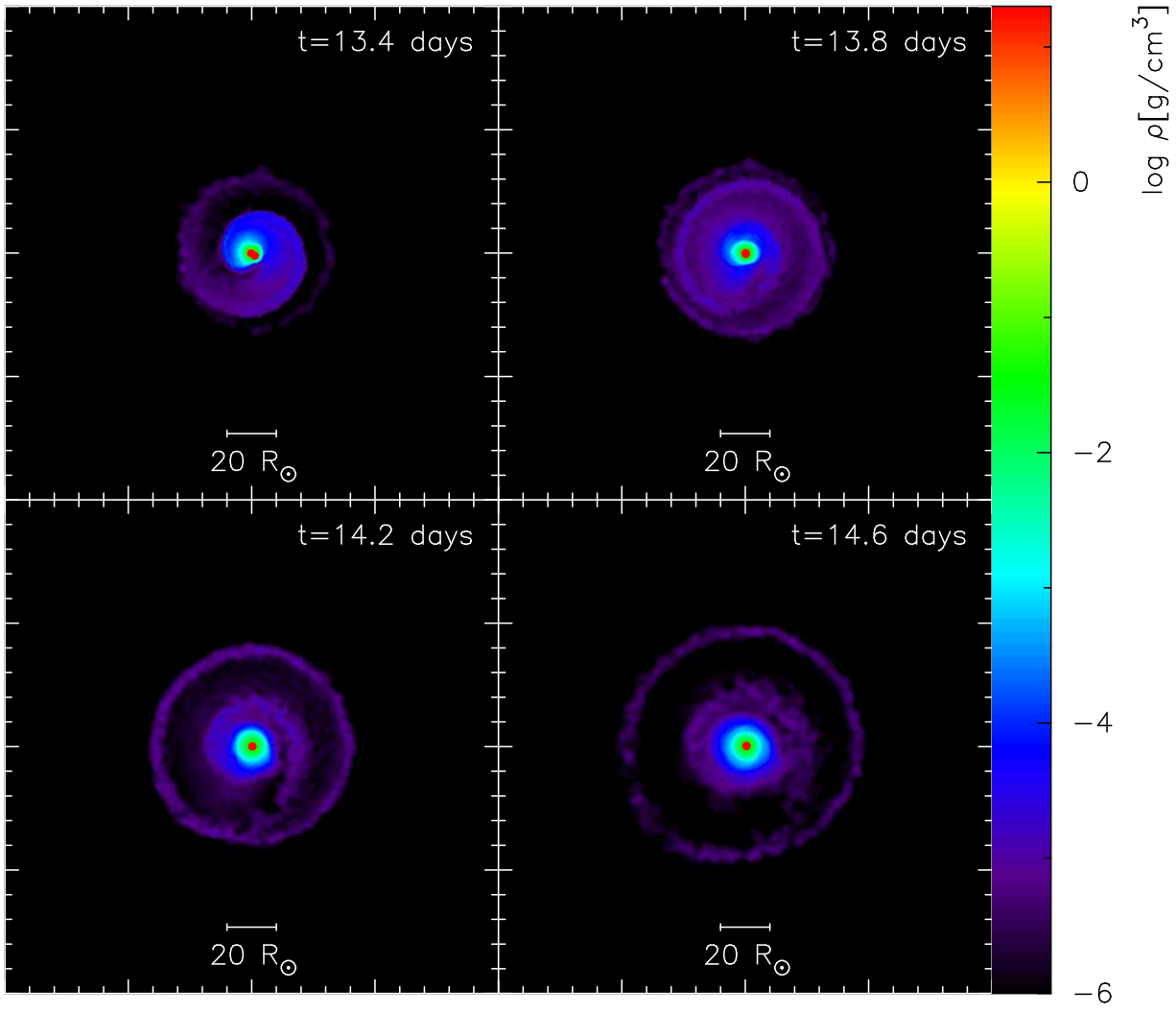

Figure 3.16: Ring formation in the simulation ps375.

3.6 Merger product

The observations of V1309 Sco after the outburst, when its light curve was rapidly declining, show that its temperature is cooler than that of its progenitor. Its radius, inferred from luminosity and temperature, reached $\sim 310\ R_\odot$ at maximum. In about 15 days after the peak, the radius of the object was estimated to have reduced already to $\sim 150\ R_\odot$, and in a few years it shrunk to about $5\ R_\odot$, just a bit larger than the progenitor (Tylenda et al., 2011). While the implied radius of $\sim 150\ R_\odot$ during the luminosity plateau is related to the wavefront of cooling and recombination of the ejecta (Ivanova et al., 2013a), the observations during the light-curve decline correspond to the surface of the merged star that becomes visible once the ejecta has fully recombined and become

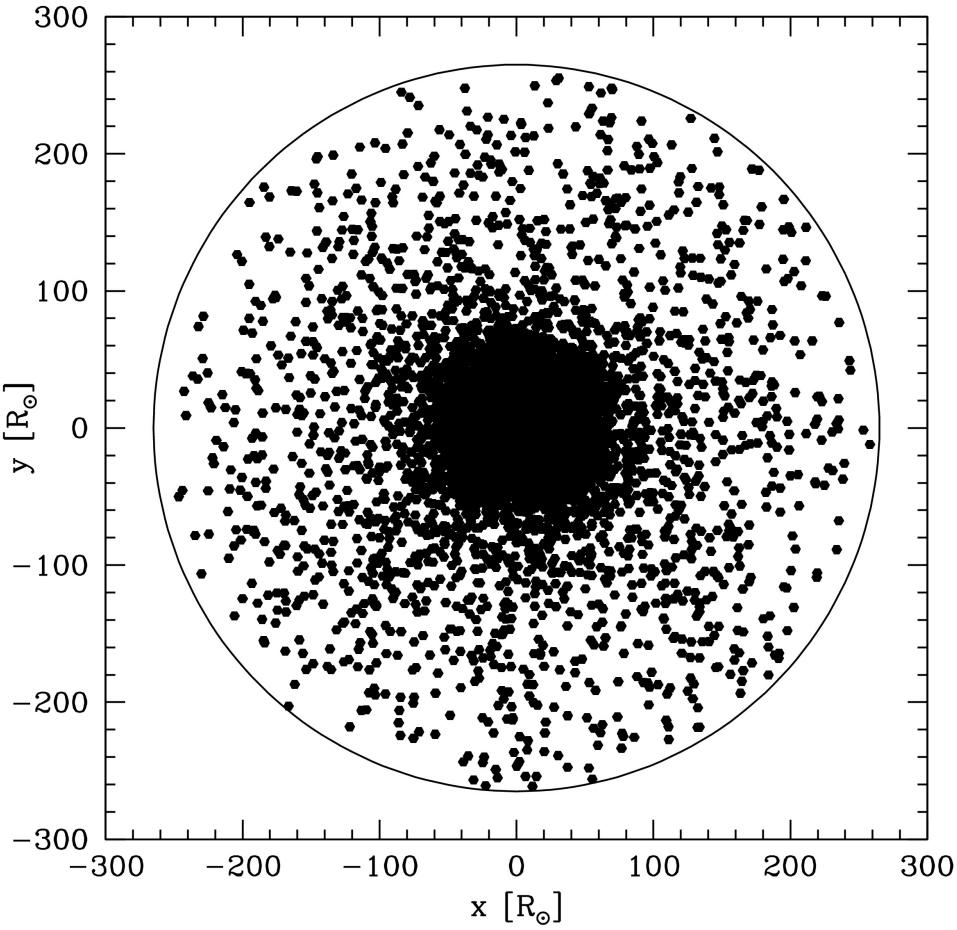

Figure 3.17: Distribution of particles projected onto the equatorial plane when the merger product has reached its hydrostatic equilibrium for the simulation ms376.

transparent.

3.6.1 Equilibrium

We analyze the merger product once it is in hydrostatic equilibrium. We define this as when the kinetic energy of the merged object is much smaller than its internal energy, $E_{\rm in}/E_{\rm kin} > 30$, and the internal and kinetic energies of the merger product remain nearly constant for a time interval comparable to its dynamical timescale. By that moment at least 1.6 $M_{\odot}$ of the bound mass is enclosed in a radius less than 100 $R_{\odot}$ (see Figures 3.17 and 3.18). The same radius of 100 $R_{\odot}$ corresponds roughly to the surface of optically thick material. More specifically, in simulations with a non-degenerate companion, the bound objects are fully enclosed in a radius less than 120 $R_{\odot}$,

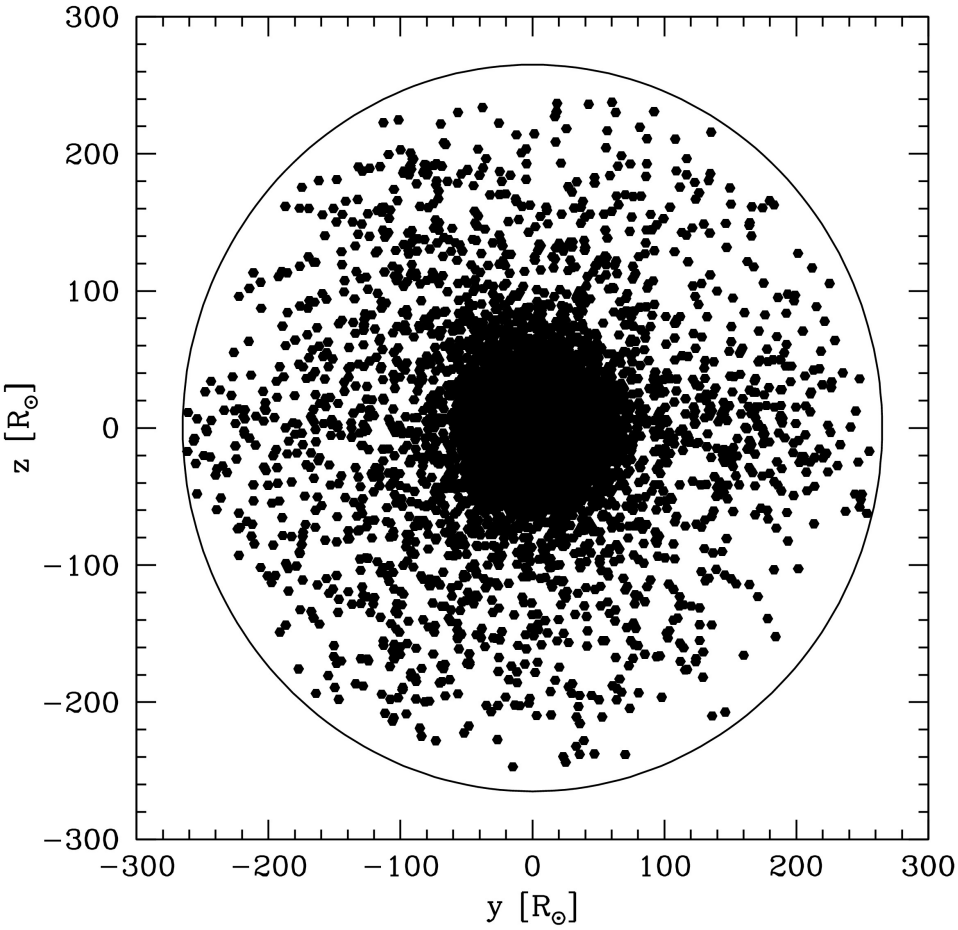

Figure 3.18: Distribution of particles projected onto the *yz* plane when the merger product has reached its hydrostatic equilibrium for the simulation ms376.

while in simulations with a degenerate companion bound material can extend much farther away, up to $\sim 600\ R_\odot$. The dynamical timescale for a $1.6\ M_\odot$ object of $100\ R_\odot$ is about 15 days, and as we found from the simulations, the kinetic and thermal energies usually stabilize in about half that time. The low-mass expanded envelope can be expected to contract on its own thermal timescale, which is just about a few years, as in observations. This thermal contraction phase, with the rapid loss of energy from the envelope with radiation, however, cannot be modeled with the SPH code, despite the timescale being close to the dynamical timescale.

3.6.2 Symmetries

We find that the distribution of particles of the merger product is fairly symmetric, both in the equatorial (xy) plane and the polar axis (yz) plane; however, rotation flattens the merger product so that there are more particles near the equator than near the poles (see Figures 3.17 and 3.18).

We calculate the mass of the bound material in different directions. The northern and southern hemispheres have a very similar mass (except for the core), with the ratio of masses very close to one. Similarly, we also calculate the mass enclosed in a cone with an opening angle of 50° along $+x$, $+y$, and $+z$ directions. These numbers reveal that the ratio between m_{+x} and m_{+y} is about one, while the mass ratios of m_{+x}/m_{+z}, and m_{+y}/m_{+z} are up to 1.5 in the case of a non-synchronized binary with a main-sequence donor. At the same time, a synchronized binary with a main-sequence donor is almost symmetric.

3.6.3 Star profiles

For rotating stars, it is argued that the stellar equations should be solved across isobaric shells instead of spherical shells (e.g., Heger et al., 2000). Accordingly, the transformation from a three-dimensional SPH model to a one-dimensional model can be done by averaging on isobaric surfaces.

We sorted the particles by means of two methods, (1) pressure, and (2) radius; where the particles with maximum pressure is defined as the center in the method (1), and the center of mass of the bound material is defined as the center of the merged product for the method (2). Once we have sorted the particles by pressure or radius, we average the thermodynamics and dynamical variables of the SPH particles by a regular fixed bin.

In Figure 3.19 we compare the radius profiles of the formed star (the model ms376) obtained by the radius-sorting and pressure-sorting methods. Except for the very inner part near the core the radius profiles obtained with two methods are indistinguishable. A similar comparison of density and temperature profiles obtained with the two methods show that there is a slight effect for the temperature near the surface (it is lower when isobaric surfaces are used), but otherwise both methods continue to give similar results (see Figures 3.20 and 3.21).

3.6.4 Angular momentum

We find that the merger product does not rotate as a solid body — see Figure 3.22, where we show the specific angular momentum profile of the merger product in simulation ps376 compared to that of the initial RG star and that of the merger product if it were to rotate rigidly. We note that

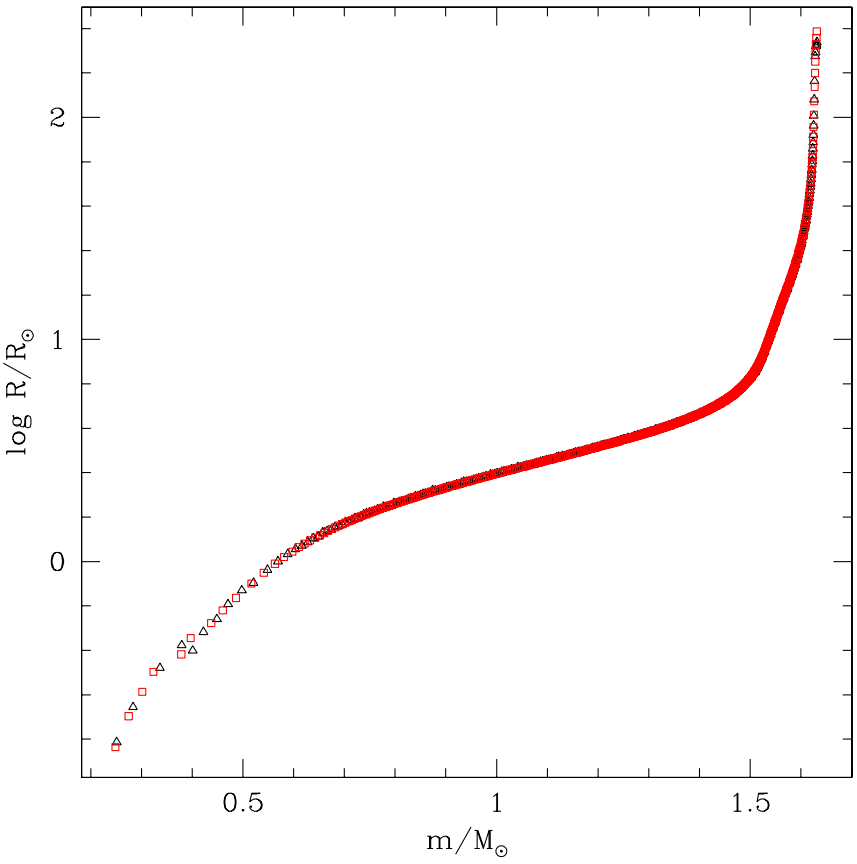

Figure 3.19: Radius profiles for the merger product for the simulation ms376. The black open triangles show the profile for the merger product sorted by pressure while the red open boxes are sorted by radius. See the text for details about the sorting methods.

our simulations use the Balsara switch in the artificial viscosity in order to minimize the spurious transport of angular momentum (Lombardi et al., 1999).

The envelope of the merger product, from about 1.25 $M_\odot$ to 1.5 $M_\odot$, shows rotation close to that of a rigid body with $\Omega = 10^{-5}$ Hz — note that the star is still expanded, which is why the rotation appears to be slower than in the initial star. Overall, the merger product has two to three times more angular momentum than in the initial star. If the merger product contracts to $5R_\odot$ within several years, as in the observations, the critical surface angular velocity will become $\Omega_{\rm crit} = 10^{-4}$ Hz and the critical value of the specific angular momenta near the surface will be $j_{\rm crit} \sim 10^{19}$ cm^2 s^{-1}. Therefore, it is possible (although not necessary) that the outer layers of the merger product might rotate close to the critical rate. We also note that the rotational profile with $dh/dr < 0$ is secularly unstable on the thermal timescale of the star (Kippenhahn, 1969).

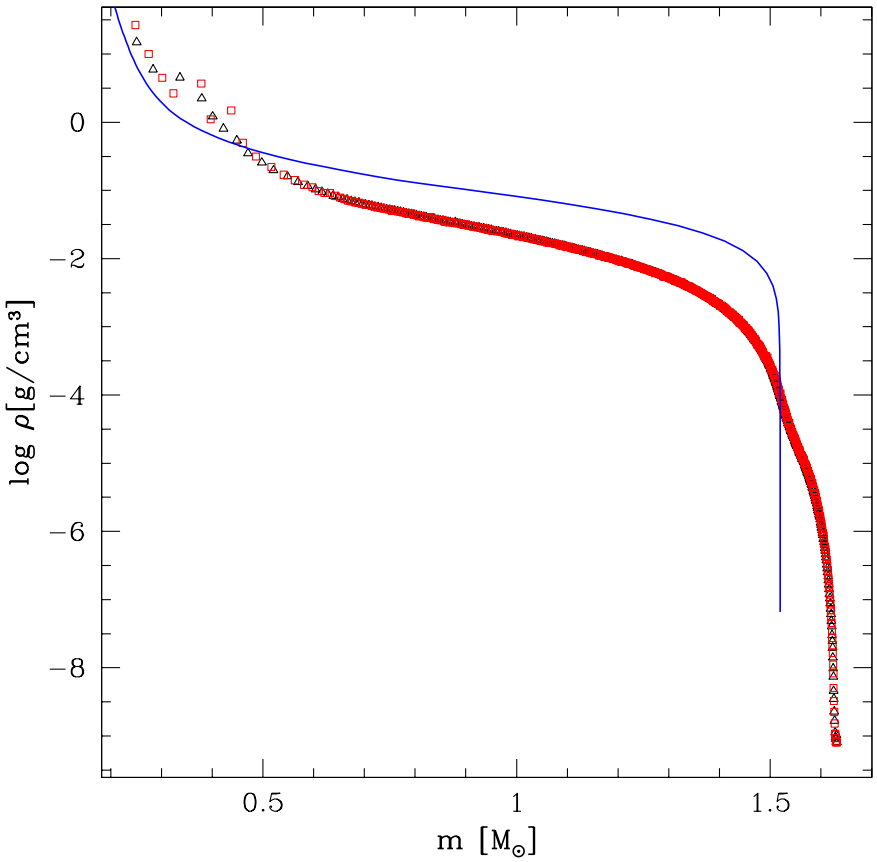

Figure 3.20: Density profiles for the merger product for the simulation ms376. The black open triangles show the profile for the merger product sorted by pressure, while the red open boxes are sorted by radius. The blue solid line corresponds to the initial profile of the RG.

3.6.5 Entropy

In Figure 3.23 we show the specific entropy of the merger product, comparing it with the initial entropy profile of the donor as given both by the one-dimensional stellar evolution code and by the relaxed three-dimensional SPH model. All entropies here are obtained using Equation (3.27), which takes into account chemical composition and radiation. This equation, however, neglects partial ionization. This results in the artificial peak near the surface in the entropy profile of the initial stellar model. Otherwise, the relaxed three-dimensional star and the initial one-dimensional star are very similar everywhere except very close to the core, which is represented by an artificial particle. The merger product has been shock-heated throughout, with no trace of either the convective envelope with uniform specific entropy of about 22 mol g^{-1} or of its convective companion

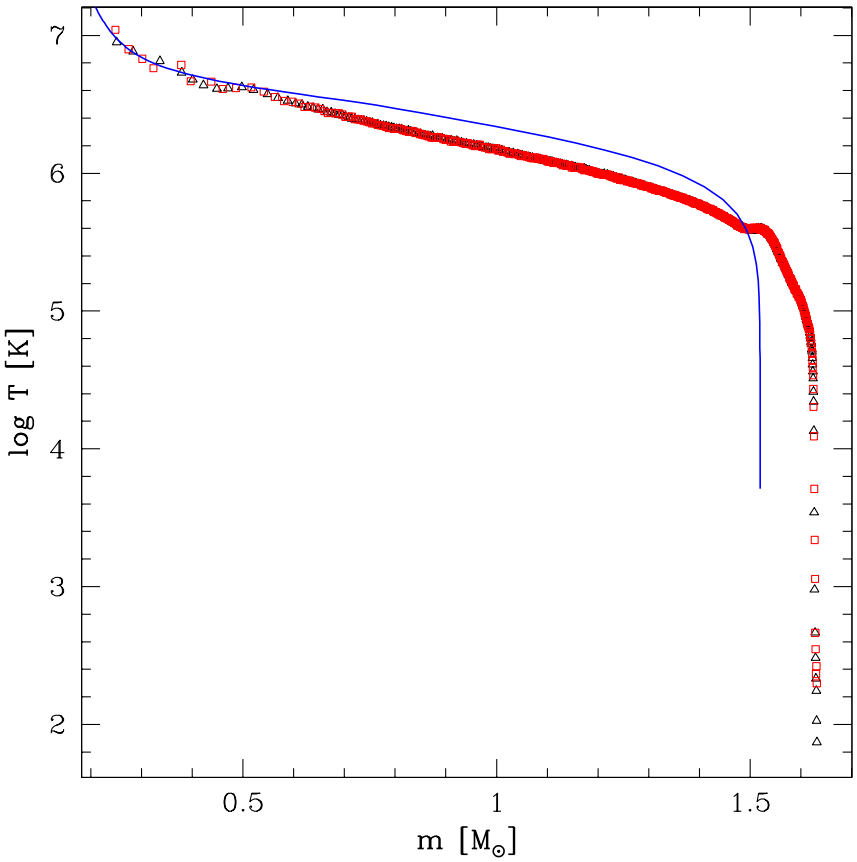

Figure 3.21: Temperature profiles for the merger product for the simulation ms376. The black open triangles show the profile for the merger product sorted by pressure, while the red open boxes are sorted by radius. The blue solid line corresponds to the initial profile of the RG.

that had a uniform specific entropy of about 12 mol g^{-1}.

3.7 Discussion

In this paper we have studied the V1309 Sco outburst by adopting a model in which the outburst results from the merger of a binary consisting of a $1.52 M_\odot$ giant and a $0.16 M_\odot$ companion, with a 1.44 day orbital period prior to merger. We have analyzed how initial conditions such as the nature of the companion (whether it was a white dwarf or a main-sequence star) and the initial synchronization between the orbit and the rotation of the donor could affect the dynamical evolution before, during, and after the merger, and we have compared our results to available observations.

For this analysis we have developed a set of tools that allow us to quantify the numerical sim-

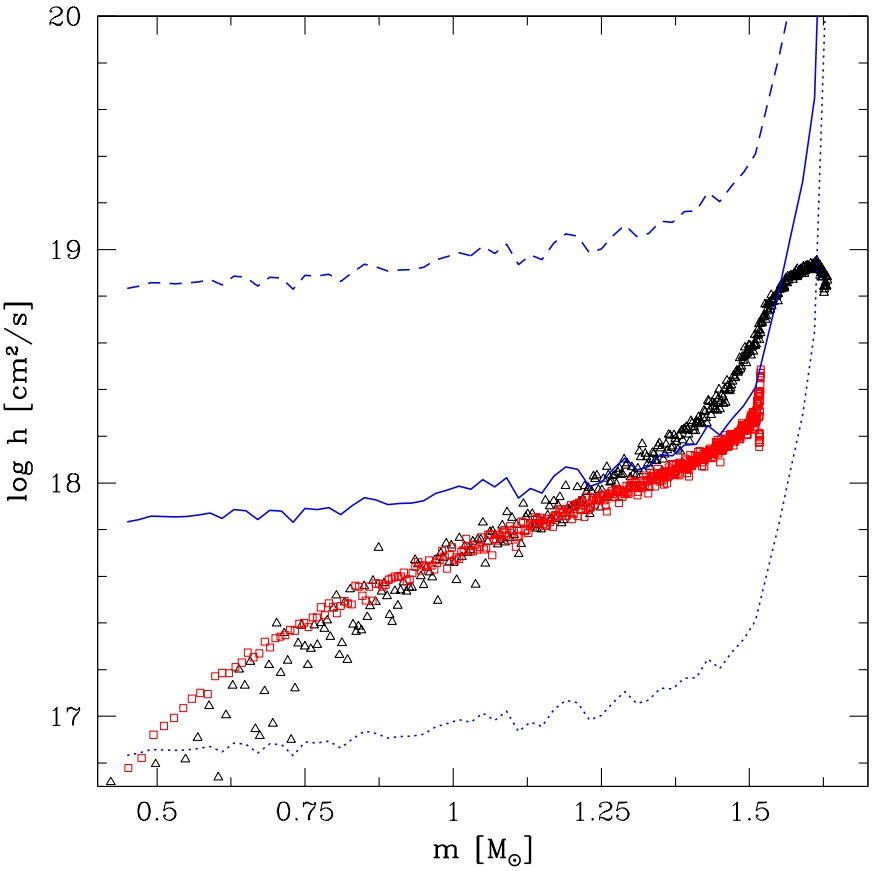

Figure 3.22: Specific angular momentum profile for the merger product (black open triangles) and the primary star (red open boxes), for the simulation ms376. The blue lines show the specific angular momentum for $\Omega = 10^{-4}$ Hz (dashed line), $\Omega = 10^{-5}$ Hz (solid line), and $\Omega = 10^{-6}$ Hz (dotted line).

ulations of CE events in a general case, independently of whether the event under consideration would result in a merger, as in the case of V1309 Sco, or in a binary formation. In presenting this set of tools, we have specifically discussed the following.

1. How to compute the effective radius of the donor star — we have found that the volume equivalent radius is best when considering mass transfer (Section 3.2.2, also Section 3.3.3).

2. How to define the orbital period in a binary decaying into a CE — we have analyzed the binary from the point of view of instantaneous (found from Keplerian orbits) and apparent (visually detectable) orbital periods (Section 3.3.1).

3. The relevant characteristic timescales — we have discussed how to determine quantitatively

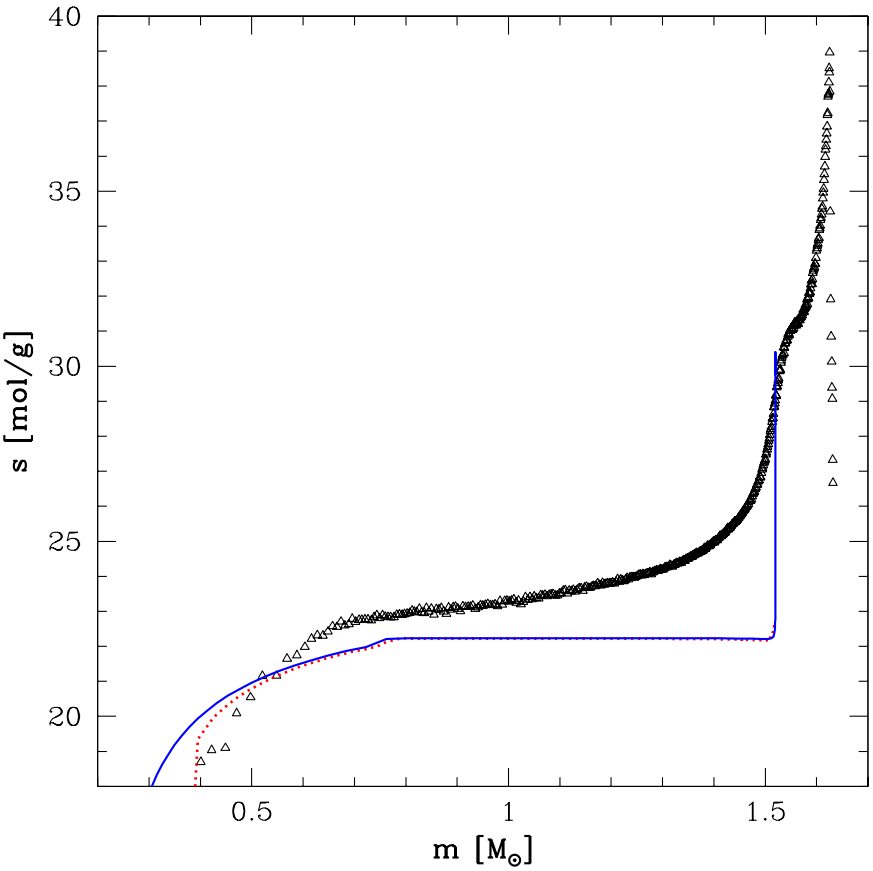

Figure 3.23: Specific entropy profiles for the merger product for the simulation ms376, assuming a fully ionized gas. The black open triangles show the profile for the merger product, the red dotted line corresponds to the profile for the relaxed primary in SPH, while the blue solid line corresponds to the profile given by the stellar model before the relaxation in SPH.

the start of the CE in simulations, as well as the start of the plunge-in and the moment of the merger (Section 3.3.5).

4. How to distinguish the unbound material — we have determined that the positiveness of the sum of only the potential and the kinetic energies for an SPH particle should be used as a criterion for its unboundedness and that inclusion of the internal energy in the criterion can lead to an error in the identification of the ejected material (Section 3.3.2 and 3.5.1).

5. The symmetry of the post-CE merger product — we have compared the degree of asymmetry of the formed star in different directions as well as compared the mapping of the three-dimensional structure to a one-dimensional profile using spherical and isobaric sur-

faces (Section 3.6.2 and 3.6.3).

By comparing the initial orbital angular momenta with the critical angular momentum determined from the spin of the stars, we have showed that all the binary configurations we have considered should be affected by the Darwin instability at the start of the simulations. But what can be expected from the Darwin instability, what are the timescales for the orbital-decay evolution that we obtain, and how reasonable are these timescales when compared against observations?

As expected, a longer timescale for the orbital decay takes place in a synchronized binary than a non-synchronized binary with all other initial conditions being similar. Our longest simulation proceeds for ~ 150 days before the merger. During the *early stage* orbital decay (before any mass transfer), the orbital-decay timescale $P/\dot{P}$ is as long as several decades, while by the end, the decay has accelerated significantly and is much faster. We also are able to fit some of our simulations with the observationally obtained exponential decay; the latter implies the match for $\dot{P}/\ddot{P}$. This suggest that the timescales in the simulations and in the observations are similar and are on the order of several to a dozen years before significant mass loss.

Note that there is no comparison between the merger timescale from the simulation and the observational ones, as we cannot know the value of $R/R_{\rm rlof}$ at the start of the observations. The initial value of $R/R_{\rm rlof}$ is very important, as the decay timescale depends sensitively on how close the donor is to its RLOF. A donor that is 99% to its RLOF would merger easily 1000 times faster than a donor that is 94% to its RLOF, even if observationally they would have the same orbital periods. For our characteristic timescales $t_0 - t_{\rm merg}$, the numbers are not terribly different than the observations, as we have t_0 being larger than the merger time by up to several hundred days, similar to in the observational fitting from Tylenda et al. (2011), where $t_0 = 2455233.5$, and if we assume that $t_{\rm merg}$ is roughly 2454530, then $t_0 - t_{\rm merg}$ is about 700 days.

However, can the Darwin instability itself provide such a fast dissipation of the orbit, or could another reason be primarily responsible for the orbital evolution? Tylenda et al. (2011) discussed that, along with the Darwin instability, it is possible that the merger could have started because the system entered into deep contact, a scenario contemplated by Webbink (1976, 1977) and started to lose mass via L_2. It is expected that the Darwin instability would act on the timescale of tidal friction, $\tau_{\rm TF}$, and that $\dot{P}/\ddot{P} \sim \tau_{\rm TF}$(Eggleton & Kiseleva-Eggleton, 2001), while the L_2 mass loss is expected to act on the same timescale as L_1 mass transfer Webbink (1976, 1977). Pejcha (2013) has argued that the Darwin timescale in V1309 Sco is too long — likely thousands of years — compared to $\dot{P}/\ddot{P}$ inferred from observations, where $\dot{P}/\ddot{P}$ is only about a few years. Instead, it was proposed that the observed period decay is due to non-conservative mass transfer from the primary to the companion accompanied by a simultaneous mass loss via a wind, during at least several

pre-merger years.

Let us investigate this in more detail. The tidal friction timescale for a star of mass M_1 and radius R_1 in a binary with a companion of mass M_2 at an orbital separation a can be estimated as (Eggleton & Kiseleva-Eggleton, 2001)

$$\tau_{\rm TF} = \tau_{\rm V} \frac{a^8}{9R_1^8} \frac{M_1^2}{(M_1+M_2)M_2} (1-Q)^2 \ , \tag{3.14}$$

where Q is the quadrupolar deformability of the star, and $Q = 0.223$ for polytropes of $n = 3/2$ (Eggleton, 2006). For our initial binaries, $\tau_{\rm TF}/\tau_{\rm V} \approx 40-70$ (the factor varies from 40 to 70 because of our range of initial conditions and the strong power dependence of the timescale on the ratio a/R_1). Here $\tau_{\rm V}$ is an intrinsic viscous timescale (Zahn, 1977). For a star with a substantial convective envelope, $\tau_{\rm V}$ is the timescale on which turbulent friction takes place, or the global convective turnover timescale. The detailed stellar model from our stellar evolution code gives the global convective turnover time as ~ 260 days for our primaries, consistent with a simple estimate from the Zahn formula. Accordingly, $\tau_{\rm TF}$ is 30-50 yr. This value is smaller than the range quoted in Pejcha (2013) by one to two orders of magnitude. This is due to two main reasons. First, Pejcha (2013) assumes $Q << 1$, which, while appropriate for polytropes with $n = 3$, leads to an overestimate of $\tau_{\rm TF}$ by nearly a factor of two for stars with large $n = 1.5$ convective envelopes. Second, Pejcha (2013) adopts that $\tau_{\rm V}$ can be as large as decades, which is significantly larger than the actual global convective turnover time given by a stellar evolution code or the formula for the friction timescale (Equation (4.11) in Zahn, 1977).

We further note that originally the Darwin instability and its relation with the viscous timescale were formally established in the limit of small viscosities (weak friction) for *equilibrium tides* (Alexander, 1973; Zahn, 1977; Hut, 1981; Eggleton & Kiseleva-Eggleton, 2001). The basic assumption of equilibrium tides is that isobaric surfaces within the star are always equipotential surfaces — i.e., the star is in the state of hydrostatic equilibrium (Eggleton & Kiseleva-Eggleton, 2001). It might be expected that this approximation breaks down when a star approaches its Roche lobe. Indeed, Eggleton (2012) argued that the Darwin instability in binaries with extreme mass ratios and evolved companions (as in the case of V1309 Sco) can have a timescale as small as a few days.

However, even though the Darwin instability has most likely naturally led to the merger both in V1309 Sco and in our simulations, it is not likely that it will naturally explain the rate of the orbital decay in our simulations. The artificial viscosity in our simulations cannot match completely the convective viscosity that has played a role prior to merger. In a star with a convective envelope, viscosity comes from up and down motions, which are not present in our SPH model. In the SPH

code, an artificial viscosity acts only when a velocity gradient is present and hence has a very different effect on the evolution of a binary orbit than what would be caused by the convective viscosity in a real binary.

We should clarify that the orbital decay due solely to the Darwin instability (before *any* mass loss) could have been observed in our simulations only while R_* remains smaller than Roche lobe of the donor—once R_* is larger, the donor would always have some SPH particles that find themselves outside of its Roche lobe. Those particles may get lost from the binary, may relocate to the Roche lobe of the secondary, or may get slightly more energetic and trigger further expansion, but ultimately these SPH particles oscillations speed up the orbital decay. In most of our simulations, the significant orbital evolution prior to merger takes place when $R_* > R_{\rm RL}$ and is affected by particles oscillations.

Because the timescales cannot be used for a direct comparison, we have to look to other features. The simulated *shape* of the orbital decay does match the observed exponential shape for a synchronized binary with a main-sequence companion or for a non-synchronized binary with a degenerate companion. On the basis of this pre-merger behavior, these are our favored types of progenitor binary. In contrast, the orbital decay in synchronized binaries with a degenerate companion is not consistent with the observed exponentially shaped decay.

Now let us return to the mass loss from the system. In our simulations, we indeed observe situations in which most of the mass lost from the system prior to merger proceeds via L_2. However, this occurs only in initially synchronized binaries (note that as synchronized binaries we include systems with the degree of corotation down to 0.85) — non-synchronized systems show mainly an isotropic mass loss in "clumps." Why do synchronized binaries in our simulations have L_2 mass loss prior to merger, while non-synchronized do not? This could be because the specific angular momentum of the material that is transferred from the donor to the secondary in a synchronized system is higher than in an non-synchronized system, and a particle can be lost via L_2 only if it has an angular momentum high enough to at least reach L_2 point. Indeed, we find that the average specific angular momentum of SPH particles moving in the neighborhood of L_1 point toward the secondary in synchronized systems exceeds the angular momentum threshold posed by the L_2 location, but only by about 50%. It also might be because only in synchronized systems the donor is shaped as theoretically expected simplified Roche lobe, while in an non-synchronized binary, the donor is significantly more spherical and starts to lose mass before it extends to L_1.

A fully non-conservative L_2 mass loss in our system leads to a decrease in the specific angular momentum of the remaining binary. It forces the orbit to shrink, which leads to the increase in RLOF; the latter accelerates exponentially the L_1 mass transfer, which quickly becomes fully dy-

namical, and the system merges. Indeed, in our simulations, L_2 mass loss, once started, lasts only for a few days. However, non-synchronized binaries, those that do not have L_2 mass loss, merge too, even though it takes much longer for them to complete the merger after their L_1 mass transfer started. Hence, depending on how well the system is synchronized, L_2 mass loss can precede the merger, but it does not have to be responsible for the merger to occur. Our results therefore suggest that L_2 mass loss could not be responsible for a long-term (several years timescale) orbital decay in V1309 Sco [1]. This, coupled with our estimate for $\tau_{\rm TF}$ above and with our checks of the Darwin instability criterion, advocates that it was indeed the Darwin instability that resulted in the observed orbital decay.

Soker & Kashi (2012) discussed that the outbursts for ILOTs could be powered by mass accretion onto a main-sequence star which could potentially launch jets. We found that the non-synchronized cases do not form an accretion disk, since the donor's particles do not have enough angular momentum to go through L_1. In contrast, the synchronized cases show a few SPH particles around the main-sequence star (accretion disk). The total mass of these particles is $\sim 0.0005 M_{\odot}$, and their velocities, relative to the main-sequence star center of mass, are up to 200 km s^{-1}. For comparison, the escape velocity of the main-sequence star is close to 600 km s^{-1}. The highest velocity gas in our simulations, which is just above the escape velocity of the donor, is reached when the CE is starting or has started; hence, the highest velocity gas is not due to jets/winds from the accretion disk. The accompanying visualizations are useful for understanding the flow pattern of the gas (see the animations in the online journal, Figures 3.24 and 3.25).

We have analyzed how the mass loss proceeded throughout all of our simulations, finding that most of the mass loss takes place in up to three individual mass outburst — before the merger, during the merger, and after the merger was completed — where each outburst takes away from about 0.0048 to 0.047 $M_{\odot}$ and lasts from one to a few days (several dynamical timescales of the initial binary). Our synchronized systems with a degenerate companion lack a clear separation between the mass outbursts before and during the merger. All our simulations with a non-degenerate donor have two episodes of mass outburst and lack the third mass outburst after the merger is completed. All simulations with a non-synchronized donor and a degenerate companion show three mass outbursts, and vice versa. The observed light curve was reconstructed best with two mass outbursts, suggesting that the latter systems are least likely to represent the initial binary. The total amount of

[1] We also find that Equation (3) in Pejcha (2013) is incorrect, as can be verified by checking this equation in the limiting case of $\beta = 1$, when the mass is lost with specific angular momentum of the donor star. Pejcha (2013) uses Equation (3) for the orbital period evolution during the mass transfer and at the same time for calculating mass transfer rates and, consequently, for the mass loss rate. Detailed derivations of orbital evolution for various modes of the mass loss and the mass transfer can be found in Soberman et al. (1997).

the ejected mass in our simulations does not vary much between the models and is from $0.038 M_{\odot}$ to $0.086 M_{\odot}$.

The kinetic energy of the ejected material at infinity is comparable to the initial binding energy in the envelope of the donor. This suggests that the energy formalism used for predicting CE outcomes needs to account for kinetic energies in the energy budget. We find that velocities at infinity are 160–190 km s^{-1}; they are in the same range as were found in observations of V1309 Sco using the profile of the HeI emission line, 160–180 km s^{-1} (Mason et al., 2010).

We find that the specific angular momentum of the ejected material is significantly larger than the specific angular momentum of the material of the material in the initial binary, by 5.8–8.1 times[2]. In our simulations involving a synchronized binary, the ejecta form a well-distinguished outer ring with a bit less pronounced second inner ring — this is the consequence of L_2 mass loss. In non-synchronized binaries, the ejecta have the shape of an expanding bubble with "clumps." Currently, the observations do not yet allow us to distinguish whether the ejecta form a ring or bubble (Nicholls et al., 2013), but it may be done in the future. In this case, it can provide a further insight on how much the system was synchronized at the start.

Martin et al. (2011) proposed that if a merger produces a disk, this disk could be the progenitor of Jupiter-like planets around the merged star. We observe that ejecta is "clumped" in all our simulations, with the clumpiness being especially apparent in the case of non-synchronized systems. The long-term evolution of these clumps cannot be traced in our code.

After the merger, hydrostatic equilibrium in the bound mass is obtained fairly quickly, within a dozen days. By then, most of the bound and optically thick mass is located within a radius of 100 $R_{\odot}$. This luminous and expanded object will further experience thermal relaxation, with an initial timescale of a few years. We find that the formed star is significantly shock-heated compared to its progenitor and, before thermal relaxation takes place, has an entropy profile characteristic of a radiative star. With our SPH code, we cannot judge when exactly the envelope of the star will become convective again, but it may take place as quickly as within a few years after the merger.

Partially as a result of the high angular momentum loss with the ejecta, and partially due to a relatively slow rotation of the initial system, the merged objects are not expected to be necessarily at their critical rotation even after they are thermally relaxed and shrunk — their angular momenta are only about two to three times of the initial ones. The merged star, when in hydrostatic equilibrium

[2]We note that in the γ-formalism that uses angular momentum conservation to predict the outcomes of the CE events, this value would be taken as 1.5 (Nelemans et al., 2000). There is no reason to believe that the same value of $\gamma \sim 1.5$ is valid for all the systems entering the CE phase. Since this parameter has a tremendous effect on the outcome, where a difference in only few per cent in its value can change the outcome completely (Woods et al., 2011; Ivanova et al., 2013b), a fine-tuning for each kind of binary needs to be done.

but before its thermal equilibrium, does not appear to have a solid body rotation — while the donor is still expanded, its outer layers rotate significantly slower than its inner layers. For a time after the thermal relaxation (which takes only a few years for the expanded outer layers), the obtained specific angular momentum profile predicts that the outer layers will rotate faster than the inner layers. It may be expected that during the thermal relaxation, as the object transforms from a radiative to a convective star and at the same time would attempt to redistribute the angular momentum, the object will have strong differential rotation. This may result in an efficient dynamo operation that will be accompanied by X-ray luminosity (Soker & Tylenda, 2007). Following the derivation in Soker & Tylenda (2007), this X-ray luminosity can be estimated to be $\sim 10^{31}$ erg s^{-1} during the envelope contraction phase. We note however that their estimate might be not fully applicable, as at the initial contraction stage the object is radiative. A more detailed study of how the thermal relaxation proceeds in the merger product is definitely required for understanding magnetic field formation when the convective envelope is developed for the first time. Currently, 5 yr after the outburst, the ejecta provides a hydrogen column density from $\sim 10^{23}$ to 10^{24} cm^{-2} and can hide an X-ray object with the luminosity up to 10^{32} erg s^{-1}. Indeed, a recent *Chandra* observation, made in 2013, did not detect a single photon during 35 ks exposure (S. Rappaport 2013, private communication).

We conclude that all considered progenitor binaries can produce an outburst resembling the V1309 Sco event. The comparison of details of observations with features obtained in simulations, such as how the mass is ejected, what is the radius of the merged object, and the shape of the orbital period decay before the merger most favors a synchronized binary with a main-sequence companion. Future observations of the shape of the ejected material (a shell-type bubble versus a ring) and the X-ray luminosity can help with further understanding of V1309 Sco object.

The authors are grateful to S. Rappaport for providing the results of *Chandra* observations. The authors thank R. Tylenda and the referee N. Soker for the valuable comments. J.L.A.N. acknowledges support from CONACyT. N.I. acknowledges support by NSERC Discovery Grants and Canada Research Chairs Program; this research was supported in part by the National Science Foundation under Grant No. NSF PHY05-51164. J.C.L. is supported by the National Science Foundation under grant No. AST-1313091 and thanks Zach Silberman for useful discussions. Some code for this project was developed in the Extreme Science and Engineering Discovery Environment (XSEDE), which is supported by National Science Foundation grant OCI-1053575. This research has been enabled by the use of computing resources provided by WestGrid and Compute/Calcul Canada.

3.A Entropy in a Fully Ionized Gas

The specific entropy s (erg K^{-1} g^{-1}) of a mixture of atoms, ions, and electrons together with radiation is given by Bisnovatyi-Kogan(2001; note that the is a + symbol missing after the 5/2 and before the ln in the double summation in the English version) as follows,

$$s = \frac{k}{\rho}\sum_i\sum_{j=0}^{i} n_{ij}\left\{\frac{5}{2}+\ln\left[\left(\frac{m_i kT}{2\pi\hbar^2}\right)^{3/2}\frac{g_{ij}}{n_{ij}}\right]\right\}+\frac{k}{\rho}n_e\left\{\frac{5}{2}+\ln\left[\left(\frac{m_e kT}{2\pi\hbar^2}\right)^{3/2}\frac{2}{n_e}\right]\right\}+\frac{4}{3}\frac{aT^3}{\rho}, \quad (3.15)$$

where x_i is the mass fraction of the element, y_{ij} is the fraction of the ith element ionized to the j-state, $m_i = A_i m_{\rm u} = (1{\rm g})A_i/N_A$ is the nuclear mass,

$$n_{ij} = x_i \rho y_{ij}/m_i \quad (3.16)$$

is the number density of ions,

$$n_e = \sum_i\sum_{j=1}^{i} j n_{ij}\ {\rm cm}^{-3} \quad (3.17)$$

is the electron number density,

$$\mu = \left[\sum_i \frac{m_u}{m_i}\, x_i \sum_{j=0}^{i}(1+j)y_{ij}\right]^{-1} \quad (3.18)$$

is the number of nucleons, $m_{\rm u} = 1.66057\times10^{-24}$ g is the atomic mass unit, $N_A = (1\ {\rm g})/m_{\rm u}\ {\rm mol}^{-1}$ is the Avogadro's number, $m_e = 9.10953\times10^{-28}$ g is the mass of the electron, $\hbar = 1.0546\times10^{-27}$ erg s is the Planck constant, $k = 1.38064\times10^{-16}$ erg K^{-1} is the Boltzmann constant, $a = 7.565\times10^{-15}$

erg cm^{-3} K^{-4} is the radiation density constant, and $c = 2.9979 \times 10^{10}$ cm s^{-1} is the velocity of light in vacuum. For a fully ionized gas the fraction of the ith element ionized to the j-state can be written as

$$y_{ij} = \begin{cases} 1 & i = j \\ 0 & i \neq j \end{cases}, \tag{3.19}$$

and $A_i \approx 2i$. Then, we can get

$$n_e = \sum_i i n_{ii} = \rho \sum_i i \frac{x_i}{m_i} = \frac{\rho N_A}{\mu_e}, \tag{3.20}$$

where μ_e is the mean molecular weight per free electron,

$$\mu_e \equiv \left[\sum_i i \frac{x_i}{A_i} \right]^{-1} \approx \left[x_H + \frac{x_{He}}{2} + \frac{1}{2} x_A \right]^{-1}; \quad x_A = \sum_{i \geq 3} x_i.$$

For the case of ions, we can write the total density as follows:

$$n_I = \rho \sum_i \frac{x_i}{m_i} = \frac{\rho N_A}{\mu_I}, \tag{3.21}$$

where μ_I is the ion mean molecular weight,

$$\mu_I \equiv \left[\sum_i \frac{x_i}{A_i} \right]^{-1} \approx \left[x_H + \frac{x_{He}}{4} + \frac{1}{14} x_A \right]^{-1}; \quad x_A = \sum_{i \geq 3} x_i.$$

Notice that we assume that the average of A_i is about 14. Now, we can define $X = x_{\rm H}$, $Y = x_{\rm He}$ and $Z = \sum x_i$ as the elements heavier than Helium. Therefore,

$$X + Y + Z = 1, \tag{3.22}$$

and we can rewrite μ_I and μ_e as follows,

$$\mu_I \approx \frac{28}{26X + 5Y + 2}, \tag{3.23}$$

$$\mu_e \approx \frac{2}{X + 1}. \tag{3.24}$$

Hence,

$$\mu = \left(\frac{1}{\mu_I} + \frac{1}{\mu_e} \right)^{-1} = \frac{28}{40X + 5Y + 16}. \tag{3.25}$$

Hence, the entropy of the gas can be written as follows, by substituting the equations (3.16) and (3.20) into (3.15) and expanding terms,

$$\begin{aligned} s &= kN_A \sum_i \frac{x_i}{A_i} \ln \left[\left(\frac{kT}{N_A 2\pi\hbar^2} \right)^{3/2} \frac{1}{\rho N_A} \right] + kN_A \sum_i \frac{x_i}{A_i} \ln \left(\frac{A_i^{5/2}}{x_i} \right) + \frac{5}{2} \frac{kN_A}{\mu_I} + \frac{5}{2} \frac{kN_A}{\mu_e} + \frac{4}{3} \frac{aT^3}{\rho} \\ &+ \frac{kN_A}{\mu_e} \ln \left[\left(\frac{kT}{N_A 2\pi\hbar^2} \right)^{3/2} \frac{1}{\rho N_A} \right] + \frac{kN_A}{\mu_e} \ln \left[2(m_e N_A)^{3/2} \mu_e \right], \end{aligned}$$

which has terms in common; thus, the new equation can be written as

$$s = \frac{kN_A}{\mu}\ln\left[\left(\frac{kT}{N_A 2\pi\hbar^2}\right)^{3/2}\frac{1}{\rho N_A}\right] + \frac{5}{2}\frac{kN_A}{\mu} + \frac{4}{3}\frac{aT^3}{\rho} + \frac{kN_A}{\mu_e}\ln\left[2(m_e N_A)^{3/2}\mu_e\right] + kN_A\sum_i \frac{x_i}{A_i}\ln\left(\frac{A_i^{5/2}}{x_i}\right).$$

Hence, we can rearrange the previous equation and get

$$s = \frac{kN_A}{\mu}\ln\left(T^{3/2}\rho^{-1}\right) + \frac{4}{3}\frac{aT^3}{\rho} + s_0, \tag{3.26}$$

where

$$s_0 = \frac{kN_A}{\mu}\left[\frac{5}{2} + \ln\left(\frac{k}{2\pi N_A^{5/3}\hbar^2}\right)^{3/2}\right] + \frac{kN_A}{\mu_e}\ln\left[2(m_e N_A)^{3/2}\mu_e\right] + kN_A\sum_i \frac{x_i}{A_i}\ln\left(\frac{A_i^{5/2}}{x_i}\right).$$

Therefore, the entropy of the *i*th particle can be written as follows:

$$S_i = \frac{kN_A m_i}{\mu}\ln\left(T^{3/2}\rho^{-1}\right) + \frac{4}{3}\frac{m_i aT^3}{\rho} + S_{0,i}, \tag{3.27}$$

where

$$S_{0,i} \equiv m_i s_{0,i} = \frac{kN_A m_i}{\mu}\left[\frac{5}{2} + \ln\left(\frac{k}{2\pi N_A^{5/3}\hbar^2}\right)^{3/2}\right] + \frac{kN_A m_i}{\mu_e}\ln\left[2(m_e N_A)^{3/2}\mu_e\right] + kN_A m_i\sum_j \frac{x_j}{A_j}\ln\left(\frac{A_j^{5/2}}{x_j}\right). \tag{3.28}$$

Here we used $g_{ii} = 1$.

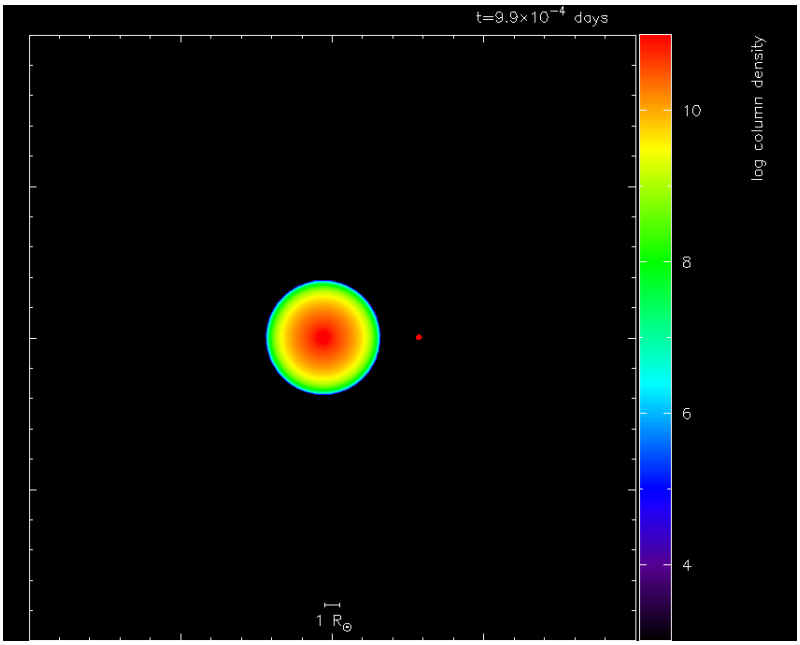

Figure 3.24: Column density animation showing the merger of a non-synchronized binary containing a $M = 1.52\,M_{\odot}$, $R = 3.51\,R_{\odot}$ giant and a $M = 0.16\,M_{\odot}$ degenerate companion with an initial orbital period of 1.42 days (simulation pn351). This animation is available only online.

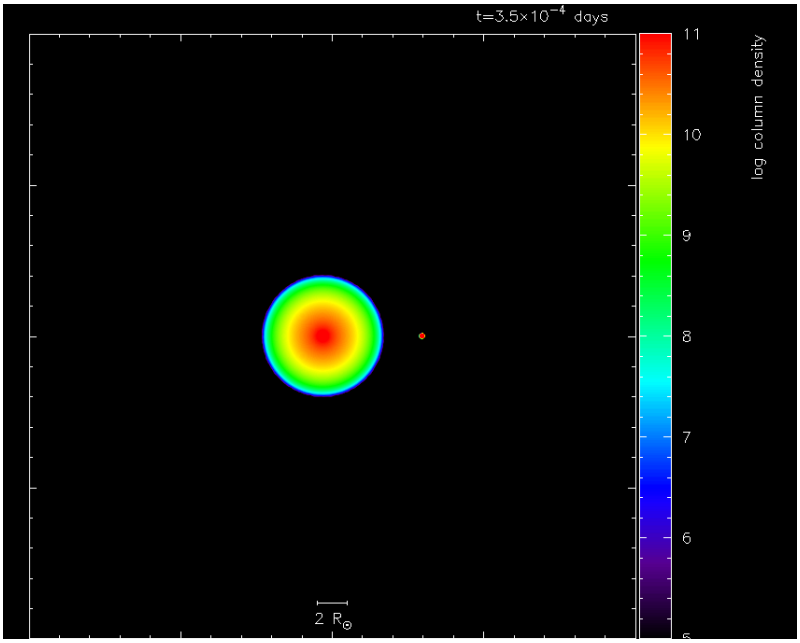

Figure 3.25: Column density animation showing the merger of a synchronized binary containing a $M = 1.52\,M_{\odot}$, $R = 3.76\,R_{\odot}$ giant and a $M = 0.16\,M_{\odot}$ main-sequence companion with an initial orbital period of 1.50 days (simulation ms376). This animation is available only online.

Chapter 4

Recombination energy in double white dwarf formation

J. L. A. Nandez[1,*], N. Ivanova[1], and J. C. Lombardi Jr.[2]

[1]Department of Physics, University of Alberta, Edmonton, AB, T6G 2E7, Canada
[2]Department of Physics, Allegheny College, Meadville, PA 16335, USA
Email: avendaon@ualberta.ca

Published 9 April 2015, *Monthly Notices Letters of the Royal Astronomical Society* **450**, L39 - L45 (2015)
DOI:10.1093/mnrasl/slv043

ABSTRACT

In this Letter, we investigate the role of recombination energy during a common envelope event. We confirm that taking this energy into account helps to avoid the formation of the circumbinary envelope commonly found in previous studies. For the first time, we can model a complete common envelope event, with a clean compact double white dwarf binary system formed at the end. The resulting binary orbit is almost perfectly circular. In addition to considering recombination energy, we also show that between 1/4 and 1/2 of the released orbital energy is taken away by the ejected material. We apply this new method to the case of the double white dwarf system WD 1101+364, and we find that the progenitor system at the start of the common envelope event consisted of an $\sim 1.5 M_{\odot}$ red giant star in an ~ 30 d orbit with a white dwarf companion.

Key words: equation of state – hydrodynamic – binaries: close – white dwarfs.

4.1 Introduction

The formation of a compact binary system composed of two white dwarfs (WDs) is widely accepted to include a common envelope event (CEE), at least during the last episode of mass exchange between the first-formed WD and a low-mass red giant (RG). Low-mass RGs have a well-defined relation between their core masses and radii, providing for DWDs the best-defined state of a progenitor binary system at the onset of the CEE among all known types of post-common envelope (CE) systems. As a result, DWD systems have served extensively as test-sites for attempts to understand the physics of CEEs, using both population synthesis approaches and hydrodynamical methods.

Previous attempts to model a CEE between a low-mass RG and a WD did not succeed to eject the entire CE during three-dimensional (3D) hydrodynamical simulations (for most recent studies, see Passy et al., 2012; Ricker & Taam, 2012). The final state of these simulations is that a significant fraction of the expanded envelope remains bound to the formed binary, forming a so-called circumbinary envelope. Then almost no energy transfer can take place from the binary orbit to that circumbinary envelope. Observationally, no circumbinary disc in a post-CE system has been found so far.

It has been proposed long ago that recombination energy of hydrogen and helium should play a role during a CEE (Lucy, 1967; Roxburgh, 1967; Paczyński & Ziółkowski, 1968; Han et al., 1994, 2002). However, until now, this energy was not yet taken into account in 3D modelling. While the initially available recombination energy can be easily comparable to the binding energy of the remaining bound envelope (e.g. Passy et al., 2012), the important question is *when and where* the energy is released – to be useful, recombination energy should not be released too early in the CEE nor in material already ejected, but instead in the circumbinary envelope at a time when the recombination energy is comparable to the binding energy of the not-yet ejected material. In this Letter, we investigate if the inclusion of recombination energy can help to remove the circumbinary envelope. We apply the new approach to the system WD 1101+364, a well-measured DWD that has $P_{\rm orb} = 0.145$ d and a mass ratio of $q = M_1/M_2 = 0.87 \pm 0.03$, where $M_1 \simeq 0.31\,M_\odot$ and $M_2 \simeq 0.36\,M_\odot$ are the masses of the younger and older WDs, respectively (Marsh, 1995).

4.2 Initial set up and definitions

We anticipate that the progenitor of WD 1101+364 was a low-mass RG that had a degenerate core of $0.31\,M_\odot$. We consider the range of masses for the RG donor, $M_{\rm d,\,1}$, from 1.0 to $1.8\,M_\odot$. To evolve

Table 4.1: Initial conditions

Model	$M_{\rm d,1}$	$M_{\rm env,1}$	$M_{\rm c,1}$	$R_{\rm rlof}$	$a_{\rm orb,ini}$	$P_{\rm orb,ini}$	$N_{\rm p}$	η	$E_{\rm bind}$	$E_{\rm rec}$	$E_{\rm orb,ini}$	$E_{\rm tot,ini}$	λ
1.0RG0N	0.985	0.668	0.317	28.21	60.11	46.57	99955	0.00	-8.454	2.059	-1.118	-7.513	1.047
1.0RG1N	0.985	0.668	0.317	29.78	63.51	50.57	99955	1.00	-8.454	2.059	-1.058	-7.453	0.992
1.0RG2N	0.985	0.668	0.317	31.35	66.81	54.57	99955	2.00	-8.454	2.059	-1.006	-7.401	0.942
1.2RG2N	1.195	0.877	0.318	29.48	60.74	44.00	99955	2.00	-12.328	2.725	-1.345	-10.945	1.093
1.4RG2N	1.397	1.079	0.319	27.73	55.59	36.24	99955	2.00	-16.947	3.369	-1.715	-15.293	1.217
1.5RG2N	1.498	1.179	0.319	25.66	50.82	30.81	99955	1.65	-20.636	4.038	-2.015	-18.609	1.267
1.5RG2NP	1.498	1.179	0.318	25.66	50.82	30.81	200221	1.65	-20.345	3.697	-2.011	-18.659	1.285
1.6RG2N	1.598	1.275	0.323	25.80	50.54	29.76	99955	2.00	-22.837	4.009	-2.157	-20.985	1.312
1.6RG0S	1.598	1.275	0.323	31.25	48.61	27.97	99955	0.00	-22.358	3.997	-2.241	-20.602	1.106
1.7RG2N	1.699	1.376	0.323	22.83	44.25	23.78	99955	2.00	-28.638	4.338	-2.619	-26.918	1.356
1.7RG0S	1.699	1.376	0.323	27.58	42.97	22.67	99955	0.00	-28.003	4.326	-2.694	-26.371	1.148
1.8RG2N	1.799	1.481	0.318	16.34	31.37	13.86	99955	2.00	-44.167	4.676	-3.912	-43.404	1.401

The models names are composed as following: two digits representing the RG mass are followed by 'RG', η value is the outermost smoothing length; then 'N' stands for non-synchronized and 'S' for synchronized ('S') cases. 'P' denotes the model with about twice larger number of particles than in all the other models. $M_{\rm d,1}$, $M_{\rm env,1}$ and $M_{\rm c,1}$ are the total, envelope and core mass of the RG, in $M_\odot$. $R_{\rm rlof}$ is the radius of the donor Roche lobe, in $R_\odot$, and η describes the adopted donor's radius definition (see section 4.2). $a_{\rm orb,ini}$ is the initial orbital separation in $R_\odot$, $P_{\rm orb,ini}$ is the initial orbital period in days. $N_{\rm p}$ is the total number of SPH particles that represent the RG. $E_{\rm bind}$, $E_{\rm rec}$, $E_{\rm orb,ini}$ and $E_{\rm tot,ini}$ are the binding energy of the RG envelope without recombination energy, the total recombination energy of the RG envelope, initial orbital energy and initial total energy, defined as the sum of the binding, recombination and initial orbital energies, respectively, in the units of 10^{46} erg. λ is a star structure parameter (see equation 4.3).

the RG and find the initial one-dimensional (1D) stellar profile, we use `TWIN/STAR` stellar code (recent updates described in Glebbeek et al., 2008). The stars are evolved until their degenerate He cores have grown close to $0.31\,M_\odot$.

For 3D simulations, we use `STARSMASHER` (Gaburov et al., 2010; Lombardi et al., 2011), a Smoothed Particle Hydrodynamics (SPH) code. Technical details on using this code to treat CE events can be found in Nandez et al. (2014). A 1D stellar profile is imported to `STARSMASHER`, where an initial stellar model represented by a certain number of particles $N_{\rm p}$ is generated via a *relaxation* process. The core of a RG is modelled as a point mass – a special particle in SPH that interacts only gravitationally with other particles. Because the centre of the giant is not fully resolved, the core mass, $M_{\rm c,1}$, is slightly more than in the 1D code (see Table 4.1 for this and other initial values). This ensures a proper matching of stellar profiles of 3D envelopes with 1D stellar profiles. The envelope mass in a 3D star is $M_{\rm env,1} = M_{\rm d,1} - M_{\rm c,1}$.

In a 3D star, the radius of the star, $R_{\rm SPH}$, cannot be defined as uniquely as the photospheric radius of the 1D star (for a thorough discussion, see Nandez et al., 2014). The stellar radius can be parameterized as $R_{\rm SPH} = R_{\rm out} + \eta h_{\rm out}$, where $R_{\rm out}$ is the position of the outermost particle and $h_{\rm out}$ is the smoothing length of that particle. The parameter η can range between 0 (in this case, some mass will be found above $R_{\rm SPH}$) to 2 (with all mass contained within $R_{\rm SPH}$). In addition, we note that

a synchronized giant is expected to attain a larger radius after relaxation than a non-synchronized giant.

The initial orbital separation, $a_{\rm orb,ini}$, for the non-synchronized cases, is found from the assumption that $R_{\rm SPH}$ is equal to the Roche lobe (RL) overflow radius, $R_{\rm rlof}$, and using the approximation by Eggleton (1983). The initial orbital period, $P_{\rm orb,ini}$ is found assuming a Keplerian orbit. For the synchronized cases, the orbital period and separation are found at the moment when the RG overflows its RL (see section 2.3 of Lombardi et al., 2011).

Equations of state (EOSs). The standard EOS (SEOS) in `STARSMASHER` is analytical and includes radiation pressure and ideal gas contributions. To take into account recombination energy, we need another prescription for the EOS. Because we evolve the specific internal energy u_i and density ρ_i for each particle (among other variables), we prefer an EOS that uses u_i and ρ_i as independent variables. However, such an analytical expression does not exist in simple form when we consider recombination/ionization of atoms. Therefore, we are bound to use a tabulated EOS (TEOS) which uses u_i and ρ_i to provide the gas pressure $P_{{\rm gas},i}$, temperature T_i, specific entropy s_i, etc.

We use the MESA-EOS module to calculate such tables (see section 4.2 of Paxton et al., 2011). The core of a RG is modelled as a point mass, and the rest of the star has uniform composition. Hence, only one table with a single set of composition for H, He, and metals needs to be generated for each RG. The tables that we generate operate in $9.84 \leq \log u[{\rm erg\ g^{-1}}] \leq 19.0$ and $-14 \leq \log \rho[{\rm g\ cm^{-3}}] \leq 3.8$. When a particle has a density or specific internal energy outside the limits of our tables, we switch to the SEOS.

Energy formalism. The energy formalism compares the donor's envelope binding energy $E_{\rm bind}$ with the orbital energy before, $E_{\rm orb,ini}$, and after the CEE, $E_{\rm orb,fin}$ (Webbink, 1984; Livio & Soker, 1988):

$$E_{\rm bind} = \alpha_{\rm bind}(E_{\rm orb,fin} - E_{\rm orb,ini}) \equiv \alpha_{\rm bind}\Delta E_{\rm orb}\ . \tag{4.1}$$

Here $\alpha_{\rm bind}$ is the fraction of the released orbital energy used to expel the CE, $0 \leq \alpha_{\rm bind} \leq 1$. The binding energy of the donor's envelope, in its standard definition, is

$$E_{\rm bind} = \sum_i m_i \left(\phi_i + \frac{3}{2}\frac{kT_i}{\mu_i m_{\rm H}} + \frac{aT_i^4}{\rho_i} \right), \tag{4.2}$$

where m_i, T_i, ρ_i, ϕ_i and μ_i are the mass, temperature, density, specific gravitational potential energy and mean molecular mass, respectively, for each particle i. The constants k, a, and $m_{\rm H}$ are the Boltzmann constant, radiation constant, and hydrogen atom mass, respectively, while ϕ_i is calculated as in Hernquist & Katz (1989). Note that $E_{\rm bind}$ in its standard definition does not include recombination energy.

The binding energy of the donor's envelope is frequently parametrized using a parameter λ, defined as (de Kool, 1990)

$$\lambda \equiv -\frac{GM_{\rm d,1}M_{\rm env,1}}{E_{\rm bind}R_{\rm rlof}}. \tag{4.3}$$

Here G is the gravitational constant. For low-mass giants, λ is known to have a value close to one, and we obtain similar results.

We find the orbital energy of the binary system according to

$$E_{\rm orb} = \frac{1}{2}\mu|V_{12}|^2 + \sum_i \frac{1}{2}m_i\phi_i - \sum_j \frac{1}{2}m_j\phi_j^{\rm RL_1} - \sum_k \frac{1}{2}m_k\phi_k^{\rm RL_2}, \tag{4.4}$$

where $\mu = M_1M_2/(M_1+M_2)$ is the reduced mass, and $\mathbf{V}_{12} = \mathbf{V}_1 - \mathbf{V}_2$ is the relative velocity of the two stars. The first term gives the orbital kinetic energy. The second term is the total gravitational energy of the binary, with the sum being over all particles i in the binary. The third and fourth terms correspond to the removal of the self-gravitational energy of the donor (the sum being over particles j in star 1) and of the WD (the sum being over particles k in star 2, initially only the WD), respectively: the remaining gravitational energy is then just the orbital contribution.

Recombination energy. In our treatment, the internal energy provided by the TEOS includes contributions from ideal gas, radiation, and the recombination energy for H, He, C, O, N, Ne, and Mg (see section 4.2 of Paxton et al., 2011). The recombination energy can be extracted as

$$E_{\rm rec} = \sum_i m_i \left(u_i - \frac{3}{2}\frac{kT_i}{\mu_i m_{\rm H}} - \frac{aT_i^4}{\rho_i} \right) \equiv \alpha_{\rm rec}\Delta E_{\rm orb}, \tag{4.5}$$

where u_i is the SPH specific internal energy of particle i. Values of $E_{\rm rec}$, as expected, scale well with the mass of the envelope. Note that here we introduce important new parameter, $\alpha_{\rm rec}$ – the ratio between the recombination energy and the released orbital energy.

Total energy. The initial total available energy, $E_{\rm tot,ini}$, is

$$E_{\rm tot,ini} = E_{\rm orb,ini} + E_{\rm bind} + E_{\rm rec}. \tag{4.6}$$

This quantity is conserved during the evolution of all our models.

Bound and unbound material. For each particle, its total energy is defined as $E_{{\rm tot},i} \equiv 0.5m_iv_i^2 + m_i\phi_i + m_iu_i$, where the first, second and third terms are the kinetic, potential, and internal energies, respectively. If the particle has negative total energy, it is bound to the binary. In this case, if the particle is located outside of either RL, the particle is in the circumbinary region. Accordingly, we classify the particles to be in (i) the *ejecta*, $m_{\rm unb}$ – the particles with positive energy, (ii) the *circumbinary*, $m_{\rm cir}$ – the matter bound to the binary but outside of the two RLs and (iii) *binary*, $m_{\rm bin}$ – the particles are inside either of the two RLs.

The total energy of the unbound material at infinity is computed when the unbound mass is in a steady state after the CEE:

$$E^{\infty}_{\rm tot,unb} = \sum_i E^{\rm unb}_{\rm tot,i} = -\alpha^{\infty}_{\rm unb}\Delta E_{\rm orb} \ . \tag{4.7}$$

Here we introduce $\alpha^{\infty}_{\rm unb}$ – the energy taken away by the unbound material in units of the released orbital energy. Note that in the standard energy formalism this quantity is always assumed to be zero.

Angular momentum budget. We calculate the orbital angular momentum

$$\mathbf{J}_{\rm orb} \equiv \mu \mathbf{R}_{12} \times \mathbf{V}_{12}, \tag{4.8}$$

where $\mathbf{R}_{12} = \mathbf{R}_1 - \mathbf{R}_2$ is the displacement from star 2 to star 1. We note that the magnitude $J_{\rm orb} = |J_{\rm orb,z}|$, where the z-direction is perpendicular to the orbital plane. An outcome of a CEE can be characterized by how much orbital angular momentum is lost. We provide the γ-parameter (Nelemans et al., 2000; Nelemans & Tout, 2005) as a way of quantifying angular momentum loss in our simulations:

$$\gamma = \frac{M_1 + M_2}{M_{\rm unb}} \frac{J_{\rm orb,\,ini} - J_{\rm orb,\,fin}}{J_{\rm orb,\,ini}}. \tag{4.9}$$

4.3 Formation of a DWD through a CEE

Comparison between the two EOSs. We compare the results of simulations with our two different EOSs using the model 1.5RG2N. In both cases, the initial relaxed stars have SPH profiles that match very well the 1D stellar profiles for pressure, density, and gravitational potential. However, this is not the case for the specific internal energy u (see Fig. 4.1): clearly only the TEOS model matches the desired 1D stellar profile. As expected, the mismatch between the relaxed profile with SEOS and the stellar one is indeed due to neglecting recombination energy.

We find that the SEOS fails to unbind the envelope in our CE simulations. Only about 50 percent of the envelope becomes unbound: the circumbinary matter does not interact with the formed binary at all, making it impossible to eject the entire envelope. This result is consistent with the findings of previous studies (Passy et al., 2012; Ricker & Taam, 2012). On the other hand, the TEOS simulation clearly makes use of the recombination energy and ejects the envelope entirely. For all other models presented in the Letter, we use the TEOS.

Masses. At the end of the simulations, we form a binary consisting of M_1 and M_2 (see Table 4.2 for all the outcomes). The unbound material $M_{\rm unb}$ is at least 99.8 percent of the initial envelope. A few, usually less than 10, SPH gas particles remain bound to the newly formed binary, been bound to either the newly formed WD, or the old WD. This explains why M_1 can be slightly larger than

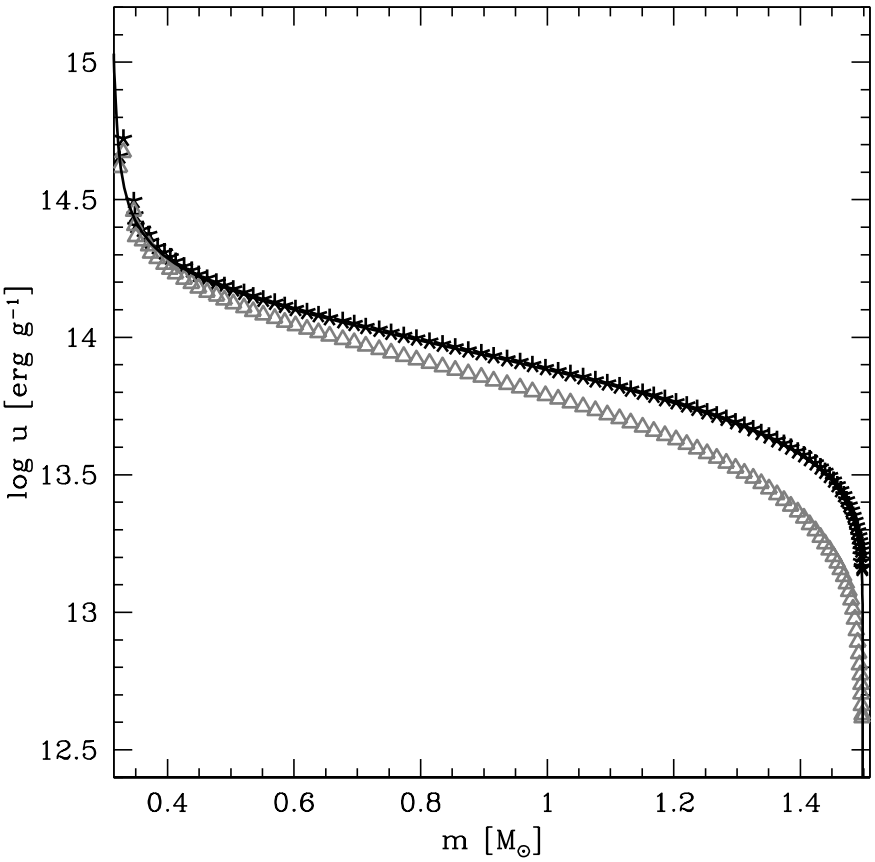

Figure 4.1: Specific internal energy u profiles for the model 1.5RG2N. The black asterisks and gray triangles correspond to relaxed u profiles for TEOS and SEOS, respectively. The black solid line corresponds to the u profile from the stellar code.

$M_{\mathrm{c},1}$, and similarly why M_2 can exceed slightly $0.36 M_\odot$. There is no circumbinary envelope left in all simulations with the TEOS. In all our simulations, the final mass ratio q ranges between 0.88 and 0.90, consistent with the observational error for WD 1101+364.

Energies. The total energy at the end of the simulation is distributed in the 'binding' energy of the gas bound to the binary, E_{bound}, the final orbital energy of the binary, $E_{\mathrm{orb,\,fin}}$, and the total energy of the unbound material at infinity, $E^{\infty}_{\mathrm{tot,unb}}$:

$$E_{\mathrm{tot,\,fin}} = E_{\mathrm{orb,\,fin}} + E_{\mathrm{bound}} + E^{\infty}_{\mathrm{tot,\,unb}}. \tag{4.10}$$

We have compared the initial and the final total energies and found that the error is less than 0.11 percent in all our simulations.

$E^{\infty}_{\mathrm{tot,unb}}$ is composed of $E^{\infty}_{\mathrm{kin,unb}}$, $E^{\infty}_{\mathrm{int,unb}}$, $E^{\infty}_{\mathrm{pot,unb}}$ – the kinetic, internal and potential energies of the unbound material, respectively. We note that $E^{\infty}_{\mathrm{kin,unb}}$ is the dominant energy in the unbound

Table 4.2: Energies and masses

Model	$M_{\rm unb}$	M_1	M_2	$E^{\infty}_{\rm kin,unb}$	$E^{\infty}_{\rm int,unb}$	$E^{\infty}_{\rm pot,unb}$	$E^{\infty}_{\rm tot,unb}$	$E_{\rm orb,fin}$	$E_{\rm bound}$	$E_{\rm tot,fin}$	$\Delta E_{\rm orb}$
1.0RG0N	0.663	0.322	0.360	3.645	0.473	-0.025	4.093	-10.992	-0.615	-7.514	-9.874
1.0RG1N	0.663	0.322	0.360	4.123	0.295	-0.015	4.403	-11.278	-0.582	-7.457	-10.220
1.0RG2N	0.663	0.322	0.360	4.081	0.543	-0.024	4.600	-11.469	-0.531	-7.400	-10.490
1.2RG2N	0.872	0.323	0.360	4.604	0.629	-0.041	5.192	-15.504	-0.639	-10.951	-14.159
1.4RG2N	1.079	0.319	0.360	6.790	0.907	-0.094	7.603	-22.911	-0.005	-15.313	-21.196
1.5RG2N	1.178	0.319	0.361	6.089	0.917	-0.096	6.910	-25.484	-0.026	-18.600	-23.469
1.5RG2NP	1.178	0.320	0.360	7.415	1.407	-0.159	8.663	-26.969	-0.366	-18.665	-24.958
1.6RG2N	1.274	0.323	0.362	5.623	1.812	-0.440	6.995	-27.741	-0.244	-20.990	-25.584
1.6RG0S	1.274	0.323	0.362	5.603	1.692	-0.381	6.914	-27.228	-0.309	-20.623	-24.987
1.7RG2N	1.370	0.323	0.366	5.854	2.042	-0.417	7.479	-33.692	-0.715	-26.928	-31.073
1.7RG0S	1.373	0.323	0.363	5.032	2.061	-0.610	6.483	-32.417	-0.466	-26.400	-29.723
1.8RG2N	1.478	0.318	0.362	8.333	1.675	-0.371	9.637	-52.873	-0.171	-43.407	-48.961

$M_{\rm unb}$, M_1, and M_2 are the unbound, stripped RG core and old WD, in $M_\odot$. $E^{\infty}_{\rm kin,unb} = \sum_i m_i^{\rm unb} v_i^2/2$, $E^{\infty}_{\rm int,unb} = \sum_i m_i^{\rm unb} u_i$, $E^{\infty}_{\rm pot,unb} = \sum_i m_i^{\rm unb} \phi_i$, and $E^{\infty}_{\rm tot,unb}$ are kinetic, internal, potential and total energies, respectively, for the unbound material. $E_{\rm orb,fin}$ is the orbital energy after the CEE. $E_{\rm bound}$ is the total energy of the particles that remained bound to the binary. $E_{\rm tot,fin}$ is the total energy of all the particles. All energies are in 10^{46} erg.

material, though the internal energy of the unbound material at the end of the simulations is also non-negligible (see Table 4.2).

We present $E_{\rm bound}$ for completeness, but the fate – accretion or ejection – of the several particles that remain bound to the binary cannot be resolved by the numerical method we use; on the timescale of our simulation they stay in an orbit within the RL of their stars. This energy includes the kinetic, internal, potential and recombination energies for these several SPH gas.

We should clarify that $E_{\rm orb,fin}$ does not have to match with the two-body approximation, namely $E_{\rm orb} = -GM_1M_2/(2a_{\rm orb})$. In the latter, the potential assumes a form $\phi \propto 1/r$, while our code includes the softened form as described in the appendix of Hernquist & Katz (1989). When the separation between the two SPH special particles is more than two smoothing lengths, the potential reduces to the Keplerian form. However, this separation is less than two smoothing lengths for the point particles after the CEE, and the potential is softened accordingly. The difference in orbital energy between the two methods varies from about 3 percent (for 1.0RG0N) to 14 percent (for 1.8RG2N), with the Keplerian values being closer to zero. The initial orbital energy, given by equation (4.4), is the same as in the two-body approximation.

Because energy is well conserved, we can equate equations (4.6) and (4.10). For that, we also use equations (4.1), (4.5), and (4.7). If we neglect $E_{\rm bound}$, we can re-write the conservation of energy in fractions of the change in the orbital energy:

$$\alpha_{\rm bind} + \alpha_{\rm rec} + \alpha^{\infty}_{\rm unb} \approx 1. \tag{4.11}$$

We find that this is indeed the case in our simulations (see Table 4.3), and that the deviation from 1 is due to $E_{\rm bound}$: the maximum deviation occurs in 1.0RG0N (~ 7.8 percent) and the minimum in 1.4RG2N (~ 0.03 percent). Note that if $\alpha_{\rm rec} = \alpha^{\infty}_{\rm unb} = 0$, the previous equation reduces to the standard energy formalism. However, values of both $\alpha_{\rm rec}$ and $\alpha^{\infty}_{\rm unb}$ are non-negligible and comparable to $\alpha_{\rm bind}$. We emphasize that previously it had been anticipated only that $\alpha_{\rm bind}$ is somewhat less than 1, and we provide new improved constraints. Unfortunately, this is not yet a final solution of the problem as $\alpha^{\infty}_{\rm unb}$ cannot be easily predicted for any system – a subject of our future studies.

Orbital angular momenta. We find that the ejected material takes away more than 90 percent of the initial angular momentum of the binary. Values of γ vary between 1.42 and 1.87. This large range of values unfortunately does not allow the obtained values of γ to be useful for predicting the final parameters in a population synthesis for all possible DWD systems (for details, see Ivanova et al., 2013b).

Final orbital parameters. We find the final orbital separation as $a_{\rm orb,fin} = (r_{\rm a} + r_{\rm p})/2$, where $r_{\rm p}$ is the periastron and $r_{\rm a}$ is the apastron. We ensure that these two quantities, $r_{\rm p}$ and $r_{\rm a}$, do not change with time at the moment when we extract them from the simulations. We calculate the final orbital period $P_{\rm orb,\,fin}$ of the binary from Kepler's third law and the eccentricity of the post-CE orbit as $e = (r_{\rm a} - r_{\rm p})/(2a_{\rm orb,\,fin})$. The latter is small in all the models, showing that post-CE orbits are almost circular (in previous studies, where the ejection of the CE was incomplete, the final eccentricity was larger, 0.08 or more, e.g. Ricker & Taam, 2012).

Figure 4.2 shows the final orbital periods plotted versus initial RG. We see that, as expected, the more massive the star is, the tighter the orbit gets. We find also that the final orbital period for the non-synchronized and synchronized cases are very similar (for the final state of the binary system, the only change due to synchronization was observed for the final eccentricity, albeit final eccentricity is small in all the cases). We conclude that our best progenitor for WD 1101+364 is a $1.4 - 1.5 M_{\odot}$ RG.

4.4 Conclusions

To understand the energy budget during a CEE leading to a DWD formation, we perform non- and synchronized 3D hydrodynamic simulations with two EOSs. We confirm that taking into account recombination energy leads to a full ejection of the RG's envelope and the formation of a non-eccentric binary system, whilst if we do not take recombination energy into account, we obtain result similar to previous studies and only half of the RG's envelope is ejected. The most important consideration appears not to be the value of the available recombination energy, but where and

Table 4.3: Orbital parameters

Model	$J_{\rm orb,ini}$	$J_{\rm orb,fin}$	γ	$r_{\rm p}$	$r_{\rm a}$	$a_{\rm orb,fin}$	$P_{\rm orb,fin}$	e	$\alpha_{\rm bind}$	$\alpha_{\rm rec}$	$\alpha_{\rm unb}^{\infty}$
1.0RG0N	14.340	1.188	1.861	2.015	2.115	2.065	0.416	0.024	0.855	-0.208	0.431
1.0RG1N	14.741	1.168	1.868	1.965	2.074	2.020	0.403	0.027	0.827	-0.201	0.431
1.0RG2N	15.119	1.157	1.873	1.947	2.036	2.000	0.397	0.022	0.808	-0.197	0.440
1.2RG2N	16.262	0.987	1.670	1.520	1.532	1.526	0.264	0.004	0.871	-0.192	0.367
1.4RG2N	17.116	0.759	1.557	1.070	1.089	1.080	0.158	0.009	0.800	-0.159	0.359
1.5RG2N	17.062	0.709	1.512	0.953	1.003	0.978	0.134	0.026	0.879	-0.172	0.294
1.5RG2NP	17.062	0.719	1.511	0.891	0.924	0.908	0.122	0.018	0.815	-0.148	0.347
1.6RG2N	17.685	0.678	1.479	0.880	0.948	0.914	0.122	0.037	0.893	-0.157	0.273
1.6RG0S	17.392	0.690	1.477	0.912	0.947	0.930	0.126	0.019	0.895	-0.160	0.277
1.7RG2N	17.151	0.610	1.449	0.746	0.771	0.758	0.092	0.016	0.922	-0.140	0.241
1.7RG0S	16.953	0.624	1.444	0.776	0.791	0.784	0.097	0.009	0.942	-0.146	0.218
1.8RG2N	14.932	0.446	1.417	0.464	0.493	0.479	0.047	0.030	0.902	-0.096	0.197

The orbital angular momentum $J_{\rm orb,ini}$ and $J_{\rm orb,fin}$ for the initial and final binary, respectively, in units of 10^{51} g cm^2 s^{-1}. The parameter γ is defined in equation 4.9. The closest and farthest orbital separations are $r_{\rm p}$ and $r_{\rm a}$, respectively, while $a_{\rm orb,fin}$ is the semimajor axis (all in $R_\odot$). The orbital period $P_{\rm orb,fin}$ is given in days, and e is the eccentricity of the orbit. The energy fractions $\alpha_{\rm bind}$, $\alpha_{\rm rec}$, and $\alpha_{\rm unb}^{\infty}$ are defined in equation (4.1), equation (4.5), and (4.7), respectively.

when this energy is released. Indeed, ionized material forms the circumbinary envelope initially. Recombination then takes places there, while the circumbinary envelope continues to expand. This results in the ejection of the circumbinary envelope and effectively of all the CE material. If instead the recombination energy had been released too early, the simulations would have ended up with unexpelled circumbinary envelope as in previous studies. In addition, we find that considering a complete synchronization versus non-synchronized case does not change noticeably the final results.

We introduce a modification of the standard energy formalism (Webbink, 1984; Livio & Soker, 1988), with the parameters describing the use of the recombination energy and the unbound material energy. The first one can be found from initial stellar models, but the latter requires 3D simulations. For our set of models, $\alpha_{\rm unb}^{\infty}$ has values from about 0.2 to about 0.44. However to generalize the result and make it useful for population synthesis one needs to make a thorough parameter study; this is the subject of our future studies.

As expected, we find that the more massive the parent RG star is, the tighter the final orbit gets. We do not find that the initial synchronization affects the final period but instead only changes the energy and angular momentum carried away by the ejecta, presumably shaping the post-CE nebula. We also find that our binaries end up with an eccentricity smaller than 0.04 – a result that has been expected theoretically but not yet produced in simulations.

We applied our method to the case of WD 1101+364, a well-known DWD (see Marsh, 1995).

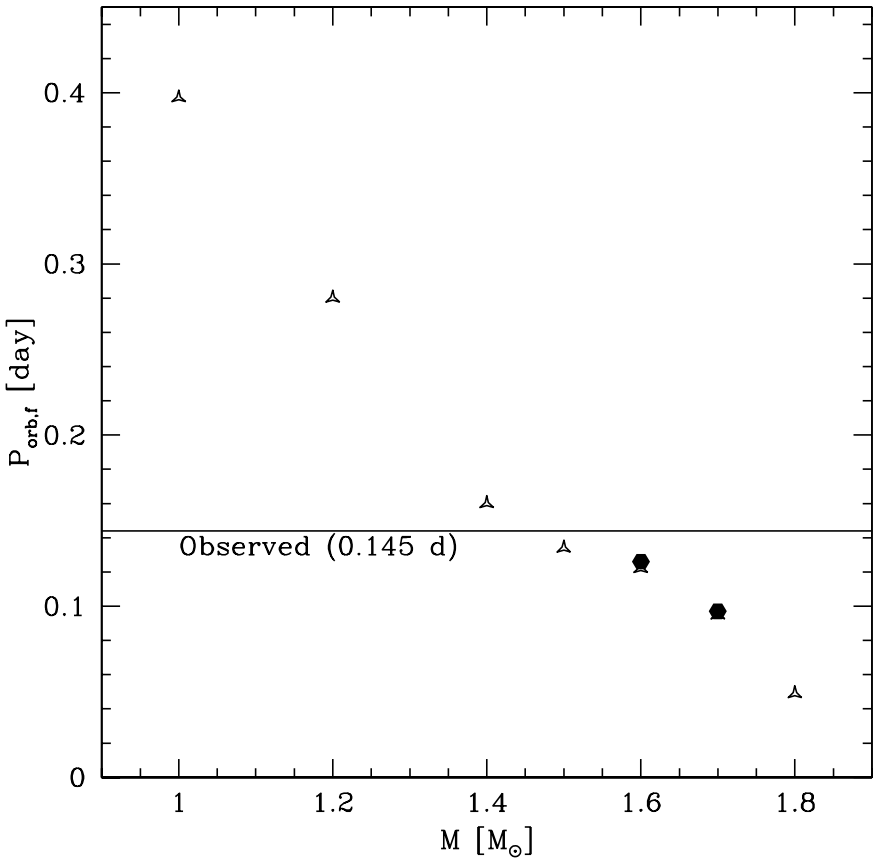

Figure 4.2: Final orbital periods versus initial mass of a RG. Triangles represent non-synchronized RGs, and circles represent synchronized RGs. Note: to compare alike cases, we show only the $\eta = 2$ cases with our standard resolution. Different η's give similar outcomes (see Table 4.3).

We inferred that its progenitor binary could have been composed of a $1.4-1.5 M_\odot$ RG and a $0.36 M_\odot$ WD companion, with $P_{\rm orb,\,ini} \approx 31-33$ days.

Acknowledgements

JLAN acknowledges CONACyT for its support. NI thanks NSERC Discovery and Canada Research Chairs Program. JCL is supported by National Science Foundation (NSF) grant number AST-1313091. This research has been enabled by the use of computing resources provided by WestGrid and Compute/Calcul Canada.

Chapter 5

Conclusions

In this PhD thesis we investigated dynamical cases of common envelope events (CEEs) with low-mass donors. We have considered both kinds of outcomes: a merger and a compact binary formation.

We analyzed the observations from the so called Luminous Red Novae (LRNe), namely M85 OT2006-1, V1309 Sco, M31 RV and V838 Mon, and linked them to the CEEs. We have made detailed CEE analysis of the V1309 Sco outburst — this outburst is unique, as this is the only known astronomical object for which there are observations for the binary before the outburst, as well as the light-curve of the object during and after the outburst. Finally, we investigated the energy and angular momentum budget in a CEE for a double white dwarf binary, where for the first time we included recombination energy in the gas.

We carried out our studies by means of hydrodynamics simulations. We used the `Starsmasher` numerical code. This code is based on smoothed particle hydrodynamics (SPH) method. To analyze the evolution of the common envelope and outcomes, we have developed a set of numerical tools for `StarSmasher`. For instance, we have determined that the volume equivalent radius is the best way to estimate the radius of a star in `StarSmasher`. Also, we proposed a new way to classify the masses (ejected mass, binary, and circumbinary) in the system, based on the kinetic and potential energy of each particle and its density. The orbital period was calculated in two different ways, Keplerian and geometrically. The latter uses the geometry of the binary in order to estimate the orbital period.

For our most recent study, we also upgraded the code to include the recombination energy, which had never been used in a hydrodynamic simulation of CEE. We integrated the recombination energy in our SPH code through a tabulated equation of state (TEOS). Out TEOS includes contributions from ideal gas, radiation and recombination energy for seven atoms (H, He, C, N, O, Ne, and Mg), and uses the density and specific internal energy as independent variables instead

of the classic way (density and temperature). We also made use of the standard equation of state (SEOS) that only includes ideal gas and radiation.

In our study related to LRNe, we were the first to propose that the recombination of the ejected material shapes the light-curve of the CEE and hence will produce their observational signature. The light-curve in this case is produced mainly by the recombination of the Hydrogen and Helium of the material that has been ejected from the binary and keeps expanding. Note the difference with the previous expectations where a CEE was expected to be observed as only a puffed up star with an increased radius and luminosity. In the case of the wavefront of cooling and recombination in a CEE, we expect a brighter peak luminosity, plateau phase, red spectra that is characteristic for Hydrogen recombination, and that velocities derived from the spectral lines (related to the motion of the material) will greatly exceed the apparent velocity of the photosphere. A similar approach with recombination had been used for Type IIP supernovae, where the light curve of the event has a plateau phase as well. By assuming that the kinetic energy of the material ejected by the CEE scales with the gravitational potential at the surface of the primary star, we can predict the luminosity and duration of the plateau phase for any CEE. We tested our model with the well-known LRNe, M85 OT2006-1, V1309 Sco, M31 RV, and V838 Mon. We found that our model agrees with their observational luminosities and duration.

Furthermore, we were able to recreate analytically the light curve of the plateau phase for V1309 Sco. We showed that to match the observations, at least two episodes of mass ejecta were necessary. It is remarkable that hydrodynamic simulations have shown that at least two mass ejecta have to occur in a binary similar to the binary observed before V1309 Sco outburst, and that the luminosities and duration match quite well for this phase.

We analyzed the outburst of V1309 Sco in more detail to find constraints on the progenitor binary. We adopted observationally-derived constraints that the pre-outburst binary consisted of a $1.52\,M_{\odot}$ giant and a $0.16\,M_{\odot}$ companion, with a 1.44 d orbital period. We then modeled the binary using two types of companions: a degenerate star and a main sequence star. We also considered different levels of synchronization, ranging from fully synchronized to non-synchronized.

We found, in general, that the particular configuration given above resulted in the merger of the two stars, regardless of the nature of the companion star. The time-scales for the mergers varied from 20 to 283 days depending on the companion. We found that the longest merger time-scale was for the degenerate companion, and the shortest for the main sequence companion.

Thereafter, we compared the initial orbital angular momenta to the critical angular momenta determined from the spin of the stars. We showed that all our simulations are genuinely affected by the Darwin instability. We caution that our SPH code uses an artificial viscosity, which is not a

real physical quantity, and can not be unambiguously compared to real physical viscosity present in convective stars. Hence, the timescale of the orbital decay we observe in our simulations can not be directly linked to the orbital decay in V1309 Sco binary in reality, even though the orbital decay there is also most likely driven by Darwin instability.

The ejection of the material during the CEE occurred in up to 3 individual mass outbursts: (i) before, (ii) during the merger, and (iii) after the merger was completed. We note that each outburst takes away from ~ 0.005 to $0.05\,M_{\odot}$ and lasts from one to a few days. All models with non-synchronized donor and a degenerate companion showed three mass outbursts, whilst models with a main sequence companion showed two episodes of mass outburst. We previously noted that the theoretical light curve for V1309 Sco was done with two mass outburst, making the latter case the most promising for the initial progenitor.

Since our simulated orbital decay time-scale does not match the observed orbital decay, we could only compared the shapes of the decays. We found that the shape of the orbital decay can be matched with a synchronized binary with a main sequence companion or with a non-synchronized binary with a degenerate companion.

We found that the specific angular momentum of the ejected material is significantly larger than the specific angular momentum of the material in the initial binary, by 5.9 to 8.1 times. The ejected material from all our synchronized binaries formed an outer torus and a less visible inner torus. The reason for this was the mass loss through L_2. On the other hand, ejecta in all our non-synchronized binaries formed an expanding bubble.

We have ultimately concluded that our best prediction for the progenitor of V1309 Sco, based on the ejected mass, radius of the merged object, and the shape of the orbital period decay before the merger, is a synchronized binary with a main sequence companion.

We studied how the energy budget during a CEE can lead to a double white dwarf (DWD) formation. Using the updated SPH code, we performed non- and synchronized 3D hydrodynamic simulations with the TEOS. We have confirmed that taking into account recombination energy leads to a full ejection of the envelope of the red giant star and the formation of a non-eccentric binary system, whilst if we do not take recombination energy into account, we obtain result similar to previous studies, and only half of the envelope of the red giant star is ejected. Despite this finding, the most important consideration appears not to be the value of the available recombination energy, but where and when this energy is released. Indeed, initially the ionized material forms a circumbinary envelope. Recombination then takes places there, while the circumbinary envelope continues to expand. This results in the ejection of the circumbinary envelope and effectively of all the common envelope material. If instead the recombination energy had been released too early, the

simulations would have ended up with unexpelled circumbinary envelope, as in previous studies. In addition, we find that considering a complete synchronization versus non-synchronized case does not noticeably change the final results.

We have introduced a modification of the standard energy formalism where we added the parameters describing the use of the recombination energy and the energy carried away by the unbound material. The first one can be found from initial stellar models, but the latter requires 3D simulations. For our set of models, $\alpha_{\rm unb}^{\infty}$ has values from about 0.2 to about 0.44. However to generalize the result and make it useful for population synthesis one would need to make a thorough parameter study.

As expected, we find that the more massive the parent red giant star is, the tighter the final orbit gets. We do not find that the initial synchronization affects the final period, but instead only changes the energy and angular momentum carried away by the ejecta, presumably shaping the post-CE nebula. We also find that our binaries end up with an eccentricity smaller than 0.04 – this result had been expected theoretically but had not yet been produced in simulations.

We also applied our method to the case of WD 1101+364, the double white dwarf with well-determined properties. We inferred that its progenitor binary could have been composed of a $1.4-1.5 M_{\odot}$ RG and a $0.36 M_{\odot}$ WD companion, with $P_{\rm orb,ini} = 31-33$ days.

Based on our analytical models and simulations, we conclude that the recombination energy and the kinetic energy of the ejecta are very significant for studies of the CEEs. These two quantities must be included in the standard energy formalism, in order to give a more strict link between the progenitor binary and the formed binary.

We have noted that the simulation of V1309 Sco did not include recombination in their equation of state. It would be very interesting to repeat the most favorable models in order to better match the observations. It is also possible to try to create a simulated light-curve from the expansion of the material by looking at the wavefront of cooling and recombination in the simulations. This could be done by defining the surface of the material when the optical depth, $\tau \sim 1$.

In order to have a better understanding of the kinetic energy of the ejecta after the CEE, it is necessary to create and analyze a more general parameter space. It is possible to define a grid for the initial red giant star mass and the companion star mass. Such a grid could help us to predict and estimate the kinetic energy at infinity for a low-mass giant interacting with a compact companion. Furthermore, we could change the nature of the companion, e.g., a main-sequence star, and compare the results with the compact companion ones. Doing so, we could have a better estimate of the total energy of the ejecta at infinity for a post-common envelope.

Appendix A

Smoothed Particle Hydrodynamics and `StarSmasher`

In this appendix, we present a brief description of the numerical method, `StarSmasher`, that we used along this project. We also show the numerical algorithms used to analyse the results obtained from `StarSmasher`. Note that the post-analysis subroutines are not linked with `StarSmasher` in anyway, they are separate programs used to extract useful information for each particular case.

`StarSmasher` is a modified version of the smoothed particle hydrodynamics (SPH) code originally developed by Rasio (1991) that has been updated by Gaburov et al. (2010) and Lombardi et al. (2011). SPH is a particle-Lagrangian method where the fluid is represented by a finite number of fluid elements, called *particles*. Unlike the particle in a cell method, SPH does not need a grid to calculate spatial derivatives. Instead, they are found by analytical differentiation of interpolation formulae. The equations of momentum and energy become sets of ordinary differential equations that are easy to understand in mechanical and thermodynamics terms.

A.1 Equations of hydrodynamics

In contrast to grid-based (Eulerian) methods, SPH is purely Lagrangian. In the Eulerian description, derivatives are calculated at a fixed point in space while in the Lagrangian description, they are evaluated in a coordinate system attached to a moving fluid element. Thus in the Lagrangian description we follow individual fish rather than stare at the pond and watch the school of fish pass by. The Lagrangian time derivative, also called substantial derivative, d/dt, is related to the Eulerian time derivative, $\partial/\partial t$, as follows:

$$\frac{d}{dt} = \frac{dx^i}{dt}\frac{\partial}{\partial x^i} + \frac{\partial}{\partial t} = \mathbf{v}\cdot\nabla + \frac{\partial}{\partial t}. \tag{A.1}$$

If we apply the last equation to the *Eulerian continuity equation*,

$$\frac{\partial \rho}{\partial t} + \nabla \cdot (\rho \mathbf{v}) = 0, \tag{A.2}$$

we find the Lagrangian form,

$$\frac{d\rho}{dt} = -\rho \nabla \cdot \mathbf{v}. \tag{A.3}$$

The *conservation of momentum* equation for a non-viscous fluid, the so-called Euler equation, reads in Lagrangian form

$$\frac{d\mathbf{v}}{dt} = -\frac{\nabla P}{\rho} + \mathbf{f}_{ext}, \tag{A.4}$$

i.e., apart from body forces such as gravity or magnetic fields included in the quantity $\mathbf{f}_{ext}$, the fluid is accelerated by gradients of the pressure P.

The first law of thermodynamics, $dU = dQ - PdV$, is the *conserved energy* equation. In adiabatic processes, $dQ = 0$. If we write every term of the equation per mass, the energy U becomes u ("energy per mass") and the volume, V, becomes v ("volume per mass"), i.e. $v = 1/\rho$, then $dv = d(1/\rho) = -1/\rho^2 d\rho$. For the case without entropy generation the first law of thermodynamics reads

$$du = \frac{P}{\rho^2} d\rho, \tag{A.5}$$

if we multiply the last equation by $1/dt$, we get

$$\frac{du}{dt} = \frac{P}{\rho^2}\frac{d\rho}{dt} = -\frac{P}{\rho}\nabla \cdot \mathbf{v}. \tag{A.6}$$

The set of equations (A.3), (A.4) and (A.6) must be closed by an equation of state (EOS). The EOS can include contributions from ideal gas and radiation. However, it can also be as complex as we want; the only problem in SPH is that the EOS should be easy to solve for a given density and specific internal energy, which are the main variables evolved by SPH.

A.2 Fundamentals of SPH

At the heart of SPH is an interpolation method that allows any function to be approximated by

$$f_I(\mathbf{r}) = \int f(\mathbf{r}') W(\mathbf{r} - \mathbf{r}', h) d\mathbf{r}', \tag{A.7}$$

where the integration is over the entire space, and W is called the smoothing kernel and h is the smoothing length that determines the local spatial *resolution* and is used in the calculation of fluid properties. If we want to recover the original function, this is possible in the limit of an infinitely small smoothing region and therefore the kernel should fulfill

$$\lim_{h\to 0} f_I(\mathbf{r}) = f(\mathbf{r}), \quad \int W(\mathbf{r} - \mathbf{r}', h) d\mathbf{r}' = 1, \quad \text{and} \quad \lim_{h\to 0} W(\mathbf{r} - \mathbf{r}', h) = \delta(\mathbf{r} - \mathbf{r}', h), \tag{A.8}$$

where the limit is interpreted as the limit of the corresponding integral interpolants. To get the discrete approximation, we can write the integral as

$$f_I(\mathbf{r}) = \int \frac{f(\mathbf{r}')}{\rho(\mathbf{r}')} W(\mathbf{r}-\mathbf{r}', h)\rho(\mathbf{r}')d\mathbf{r}', \tag{A.9}$$

where ρ is the mass density and subsequently we can replace the integral by a sum over the set of interpolation particles with masses $m(\mathbf{r}_i)$ resulting from the $\rho(\mathbf{r}')d\mathbf{r}'$ term,

$$f_I(\mathbf{r}) = \sum_i \frac{m(\mathbf{r}_i)}{\rho(\mathbf{r}_i)} f(\mathbf{r}_i) W(\mathbf{r}-\mathbf{r}_i, h), \tag{A.10}$$

Using the notation $g(\mathbf{r}_i) \equiv g_i$, we can re-write the last equation as

$$f_I(\mathbf{r}) = \sum_i \frac{m_i}{\rho_i} f_b W(\mathbf{r}-\mathbf{r}_i, h). \tag{A.11}$$

The essential point is that we can construct a differentiable interpolant of a function from its values at the particles by using a kernel that is differential. Derivatives of this interpolant can be obtained by ordinary differentiation. For example, if we want $\nabla\phi$, we can use

$$\nabla\phi(\mathbf{r}) = \sum_i \frac{m_i}{\rho_i} \phi_i \nabla W(\mathbf{r}-\mathbf{r}_i, h). \tag{A.12}$$

The divergence can be also calculated in a similar manner,

$$\nabla\cdot\mathbf{v} = \sum_i \frac{m_i}{\rho_i} \mathbf{v}_i \cdot \nabla W(\mathbf{r}-\mathbf{r}_i, h). \tag{A.13}$$

A.3 `StarSmasher`

The equations of motion for `StarSmasher` are derived from the variational principle. Hence, its equations vary from the classical SPH method (see e.g. Rosswog, 2009). The formulation of the basic equations are described below. The Lagrangian of a perfect fluid in a gravitational field is given by

$$L = \int \rho \left[\frac{v^2}{2} - u(\rho) - \phi\right] dV, \tag{A.14}$$

where ρ is the mass density, v the fluid velocity, ϕ is the specific gravitational potential, u is the specific internal energy, which can depend on the specific entropy, s. This equation can be discretized as

$$L_{\mathrm{SPH}} = \sum_i m_i \left[\frac{v_i^2}{2} - u_i(\rho_i) - \frac{\phi_i}{2}\right]. \tag{A.15}$$

The definition of ϕ_i is as follows,

$$\phi_i = \sum_l m_l g(|\mathbf{r}_i - \mathbf{r}_l|, h_i), \tag{A.16}$$

where $g(x,h)$ is the gravitational potential between two SPH particles of unit mass defined by Hernquist & Katz (1989),

$$g(x,h) = \begin{cases} -[(1/3)u^2 - (3/20)u^4 + (1/20)u^5]/h + 7/5h, & 0 \le u \le 1, \\ -1/15x - [(4/3)u^2 - u^3 + (3/10)u^4 - (1/30)u^5]/h + 8/5h, & 1 \le u \le 2, \\ 1/x, & u \ge 2, \end{cases} \tag{A.17}$$

where $u = x/h$.

Equations of motion. Now we can obtain the equations of motion by using the Euler-Lagrange equations,

$$\frac{d}{dt}\left(\frac{\partial L}{\partial \dot{\mathbf{r}}_k}\right) = \frac{\partial L}{\partial \mathbf{r}_k}, \tag{A.18}$$

where $\mathbf{r}_k$ and $\dot{\mathbf{r}}_k$ refer to the position and velocity of the particle k. Thus, we have

$$\frac{\partial L_{\rm SPH}}{\partial \dot{\mathbf{r}}_k} = \frac{\partial}{\partial \dot{\mathbf{r}}_k}\left\{\sum_i m_i \left[\frac{v_i^2}{2} - u_i(\rho_i)\right]\right\} = \sum_i m_i \mathbf{v}_i \cdot \frac{d\mathbf{v}_i}{d\mathbf{v}_k} = \sum_i m_i \mathbf{v}_i \delta_{ik} = m_k \mathbf{v}_k, \tag{A.19}$$

and therefore, this yields to

$$\frac{d}{dt}(m_k \mathbf{v}_k) = m_k \frac{d\mathbf{v}_k}{dt}. \tag{A.20}$$

The right side of the equation (A.18) becomes

$$\frac{\partial L_{\rm SPH}}{\partial \mathbf{r}_k} = -\sum_i m_i \left[\left(\frac{\partial u_i}{\partial \rho_i}\right)_s \frac{\partial \rho_i}{\partial \mathbf{r}_k} + \frac{1}{2}\frac{\partial \phi_i}{\partial \mathbf{r}_k}\right] \tag{A.21}$$

By using equation (A.5) in the last equation, now we can write the momentum equation as

$$m_k \frac{d\mathbf{v}_k}{dt} = -\sum_i m_i \left(\frac{P_i}{\rho_i^2}\frac{\partial \rho_i}{\partial \mathbf{r}_k} + \frac{1}{2}\frac{\partial \phi_i}{\partial \mathbf{r}_k}\right). \tag{A.22}$$

The density in `StarSmasher` is calculated by

$$\rho_i = \sum_l m_l W(r_{il}, h_i). \tag{A.23}$$

Here, $r_{il} = |\mathbf{r}_i - \mathbf{r}_l|$ and $W(r_{il}, h_i)$ is an SPH smoothing kernel with a compact support of $2h$. The previous equation is equivalent to the *continuity equation*. The gradient of the density can be found

by using the previous equation,

$$\begin{aligned}\frac{\partial \rho_i}{\partial \mathbf{r}_k} &= \frac{\partial}{\partial \mathbf{r}_k}\left[\sum_l m_l W_{il}(h_i)\right] \\ &= \sum_l m_l \left[\nabla_i W_{il}(h_i)(\delta_{ik}-\delta_{lk}) + \frac{\partial W_{il}(h_i)}{\partial h_i}\frac{dh_i}{d\mathbf{r}_k}\right].\end{aligned}$$

where we have used $W(r_{ij}, h_i) = W_{ij}(h_i)$, and δ_{ik} is the Kronecker delta. Gaburov et al. (2010) defined the number of neighbours of a given particle k as,

$$N_i = \sum_l G(r_{il}, h_i), \tag{A.24}$$

where $G(x,h) \equiv V(4h-4|x-h|,h)$ for $0 \leq x \leq 2h$, otherwise $G(x,h) = 0$. Lastly,

$$V(x,h) \equiv 4\pi \int_0^x x^2 W(x,h) dx.$$

The gradient for h_i can be found by taking the derivative of equation (A.24) with respect to $\mathbf{r}_k$ assuming N_i constant. After some algebraic manipulation we find,

$$\frac{dh_i}{d\mathbf{r}_k} = -\frac{1}{\chi_i}\left(\sum_l \nabla_i G_{il}(h_i)(\delta_{ik}-\delta_{lk})\right), \tag{A.25}$$

where

$$\chi_i \equiv \sum_l \frac{\partial G_{il}(h_i)}{\partial h_i}.$$

With these equations, the acceleration of a particle k can be computed with equation (A.22),

$$\frac{d\mathbf{v}_k}{dt} = -\sum_i m_i \frac{P_k}{\rho_k^2}\left[\nabla_k W_{ki}(h_k) - \frac{\omega_k}{\chi_k m_i}\nabla_k G_{ki}(h_k)\right] - \sum_i m_i \frac{P_i}{\rho_i^2}\left[\nabla_k W_{ik}(h_i) - \frac{\omega_i}{\chi_i m_k}\nabla_k G_{ik}(h_i)\right] - \sum_i \frac{m_i}{2m_k}\frac{\partial \phi_i}{\partial \mathbf{r}_k}, \tag{A.26}$$

Note that the previous equation is the *conservation of momentum* equation. Finally, the *conservation of energy* equation can be found by using equation (A.6),

$$\frac{du_k}{dt} = \frac{P_k}{\rho_k^2}\frac{d\rho_k}{dt}. \tag{A.27}$$

The time derivative of the density can be found as follows,

$$\begin{aligned}\frac{\partial \rho_k}{dt} &= \frac{d}{dt}\left[\sum_l m_l W_{kl}(h_k)\right] \\ &= \sum_l m_l \left[\frac{\partial W_{kl}(h_k)}{\partial r_{kl}}\frac{dr_{kl}}{dt} + \frac{\partial W_{kl}(h_k)}{\partial h_k}\frac{dh_k}{dt}\right] \\ &= \sum_l m_l \left[\nabla_k W_{kl}(h_k)\cdot(\mathbf{v}_k - \mathbf{v}_l) + \frac{\partial W_{kl}(h_k)}{\partial h_k}\frac{dh_k}{dt}\right].\end{aligned}$$

The time derivative of h_i can be found by taking the derivative of equation (A.24) with respect to t assuming N_i constant,

$$\frac{dh_k}{dt} = -\frac{1}{\chi_k}\sum_l \nabla_k G_{kl}(h_k)\cdot(\mathbf{v}_k - \mathbf{v}_l),$$

hence, the energy equation can be calculated as

$$\frac{du_k}{dt} = \frac{P_k}{\rho_k^2}\sum_l m_l(\mathbf{v}_k - \mathbf{v}_l)\cdot\left[\nabla_k W_{kl}(h_k) - \frac{\omega_k}{\chi_k m_l}\nabla_k G_{kl}(h_k)\right], \tag{A.28}$$

where we have defined

$$\omega_k \equiv \sum_l m_l \frac{\partial W_{kl}(h_k)}{\partial h_k}. \tag{A.29}$$

Equations (A.23), (A.24), (A.26), and (A.28) are the main constituents of `StarSmasher`. They increase the accuracy of SPH and the conservation properties in the presence of varying smoothing length.

Equation of State. The standard equation of state in `StarSmasher` is,

$$P_k = \frac{k}{\mu_k m_H}\rho_k T_k + \frac{a}{3}T_k^4, \tag{A.30}$$

where m_H is the Hydrogen mass, k is the Boltzmann constant, μ_k is the mean molecular mass, and T_k is the temperature.

Smoothing Kernel. Many kernels can be devised, however, `StarSmasher` used a kernel based on spline functions (Monaghan & Lattanzio, 1985) with its three-dimensional form being

$$W(|\mathbf{r}-\mathbf{r}'|,h) = \frac{1}{\pi h^3}\begin{cases} 1-\frac{3}{2}q^2+\frac{3}{4}q^3 & \text{for } 0\le q\le 1 \\ \frac{1}{4}(2-q)^3 & \text{for } 1<q\le 2, \\ 0 & \text{for } q>2 \end{cases} \tag{A.31}$$

where $q = |\mathbf{r}-\mathbf{r}'|/h$.

Artificial Viscosity. The term *artificial* often refers to something that it is not real, which in this case the artificial viscosity may have not much to do with physical viscosity. Artificial viscosity has viscous-like effects, but the amount of artificial viscosity is chosen on a purely numerical basis. We note that artificial viscosity is not meant to substitute physical viscosity, it is instead a method to resolve small-scale effects that cannot be resolved numerically. Let's explain a bit more, the physical viscosity smooths the solutions of length scales comparable to the gas mean free path, however, on macroscopic scales steep gradients appear in the solutions. These steep gradients

are called shocks or discontinous solutions, and they are always present in the common envelope evolution. `StarSmasher` (Gaburov et al., 2010) uses a modified version of Balsara (1995) and Monaghan (1997),

$$\Pi_{ij} = \left(\frac{p_i}{\rho_i^2} + \frac{p_j}{\rho_j^2}\right)\left(-\alpha\mu_{ij} + \beta\mu_{ij}^2\right), \tag{A.32}$$

where $\alpha = 1$, and $\beta = 2$. Gaburov et al. (2010) used,

$$\mu_{ij} = \frac{\mathbf{v}_{ij}\cdot\mathbf{r}_{ij}}{r_{ij}}\frac{f_i + f_j}{c_i + c_j}, \tag{A.33}$$

for $\mathbf{v}_{ij}\cdot\mathbf{r}_{ij} < 0$, and $\mu_{ij} = 0$ otherwise. Here, $\mathbf{v}_{ij} = \mathbf{v}_i - \mathbf{v}_j$, and f_i is defined (Lombardi et al., 2006)

$$f_i = \frac{|\nabla\cdot\mathbf{v}|_i}{|\nabla\cdot\mathbf{v}|_i + |\nabla\times\mathbf{v}|_i + \eta c_i/h_i}, \tag{A.34}$$

with $\eta = 10^{-5}$, and the divergence is calculated as follows,

$$(\nabla\cdot\mathbf{v})_i = \frac{1}{\rho_i}\sum_k m_k\mathbf{v}_{ki}\cdot\nabla_i W_{ik}(h_i). \tag{A.35}$$

Whilst the curl is computed as

$$(\nabla\times\mathbf{v}_i) = \frac{1}{\rho_i}\sum_k m_k\mathbf{v}_{ik}\times\nabla_i W_{ik}(h_i). \tag{A.36}$$

Note that c_i is the sound velocity of particle i. (Lombardi et al., 2006) found that f_i acts as a switch, approaching unity in regions of strong compression, $|\nabla\cdot\mathbf{v}|_i \gg |\nabla\times\mathbf{v}|_i$, while vanishing in regions of large vorticity, $|\nabla\cdot\mathbf{v}|_i \ll |\nabla\times\mathbf{v}|_i$. We note that Π_{ij} is added into the momentum and energy equation, so that the conservation of energy and angular momentum is preserved.

Note about the initial conditions. Our three-dimensional model are set by means of a one-dimensional profile resolved by a stellar code. Currently, we have only tested the `TWIN/STARS` stellar code. We evolve a single star from zero-age main sequence (ZAMS) to the desired evolutionary stage. This one-dimensional profile is imported in `StarSmasher` where the density profile is distributed in N SPH particles initially placed on a hexagonal close packed lattice (see Section 2.2 of Lombardi et al., 2011). For a red giant, we model the stellar core as a point mass that only interacts gravitationally with the gas SPH particles. After the initial (desired) stellar profile has been distributed along all the SPH particles, we relax the SPH particles into hydrostatic equilibrium. We note that the relaxation process is affected by including artificial viscosity contribution in the equations of motion, typically, the Euler equation (see Section 2.2 of Lombardi et al., 2011).

A.4 Subroutines for analyzing `StarSmasher`'s outcomes

Variables found. The variables computed by `StarSmasher` for each particle are mass m_k, position $\mathbf{r}_k$, velocity $\mathbf{v}_k$, acceleration $\mathbf{a}_k$, density ρ_k, specific internal energy u_k, smoothing length h_k, gravitational potential ϕ_k, and divergence of the velocity field, $\nabla \cdot \mathbf{v}$. These variables can be used to calculate quantities such as temperature T_k, pressure P_k [equation (A.30)], etc.

We want to emphasize that `StarSmasher` uses two types of SPH particles

- Point mass particles: SPH particles that only interact gravitationally, but not hydrodynamically, hence, their $u_k = 0$, $P_k = 0$, $T_k = 0$, and a fixed density $\rho_k = \text{const}$;
- Gas particles: SPH particles that interact gravitationally and hydrodynamically, they change each time step during the evolution of the simulation.

Calculation of thermodynamics variables. SPH does not evolve the temperature of each particle. Instead, we can assume that the specific internal energy for the $k-$particle is given by

$$u_k = \frac{3}{2}\frac{kT_k}{\mu_k m_H} + \frac{aT_k^4}{\rho_k}. \tag{A.37}$$

Note that the previous equation is a 4th degree polynomial equation for the temperature. We can write the previous equation as follows,

$$T_k^4 + c_k T_k + d_k = 0, \tag{A.38}$$

where

$$\begin{aligned} c_k &= \frac{3}{2}\frac{k\rho_k}{\mu_k m_u a}, \\ d_k &= -\frac{\rho_k u_k}{a}. \end{aligned}$$

Recall that a 4th degree polynomial equation has an analytic solution. We solve this equation as in the general for a quartic equation. Once, we have the temperature for each particle, we can compute the pressure, P_k, with the equation (A.30) and entropy, s_k, with equation (3.27) for each particle.

Calculation of dynamical variables. The dynamical variables such as the kinetic, potential and internal energy, as well as the angular momentum can be computed using the calculated variables by SPH. First of all, we can calculate the kinetic, potential, and internal energies for a $k-$particle as

follows,

$$E_{\text{kin},k} = 0.5m_k(v_{x,k}^2 + v_{y,k}^2 + v_{z,k}^2), \tag{A.39}$$

$$E_{\text{pot},k} = m_k\phi_k, \tag{A.40}$$

$$E_{\text{int},k} = m_k u_k, \tag{A.41}$$

respectively. Furthermore, the total energy of the system is calculated as

$$E_{\text{tot}} = \sum_k^N (E_{\text{kin},k} + 0.5E_{\text{pot},k} + E_{\text{int},k}), \tag{A.42}$$

where N is the total number of particles in the system. Note that the contribution of the total potential energy to total energy must be $1/2$ because we are summing over all contributions with the particles, otherwise, we are over estimating the total potential energy adding terms that are already considered.

Now, the angular momentum of a particle k in SPH is computed by,

$$\mathbf{L}_k = \mathbf{r}_k \times (m_k\mathbf{v}_k) = L_{x,k}\hat{x} + L_{y,k}\hat{y} + L_{z,k}\hat{z}, \tag{A.43}$$

where the components of the angular momentum for x, y, and z are given by

$$\begin{aligned} L_{x,k} &= m_k(y_k v_{z,k} - z_k v_{y,k}), \\ L_{y,k} &= m_k(z_k v_{x,k} - x_k v_{z,k}), \\ L_{z,k} &= m_k(x_k v_{y,k} - y_k v_{x,k}), \end{aligned}$$

respectively. Furthermore, the total angular momentum for the system is,

$$\mathbf{L} = \sum_k^N \mathbf{L}_k, \tag{A.44}$$

and its magnitude is just

$$L = |\mathbf{L}| = \sqrt{L_x^2 + L_y^2 + L_z^2}, \tag{A.45}$$

where

$$\begin{aligned} L_x &= \sum_k^N m_k(y_k v_{z,k} - z_k v_{y,k}), \\ L_y &= \sum_k^N m_k(z_k v_{x,k} - x_k v_{z,k}), \\ L_z &= \sum_k^N m_k(x_k v_{y,k} - y_k v_{x,k}). \end{aligned}$$

The *moment of inertia* can also be derived by setting up the simulation such that the binary rotates along the z–axis, hence,

$$I = \sum_{k}^{N} m_k (x_k^2 + y_k^2). \tag{A.46}$$

We note that the equations (A.42), (A.45), and (A.46) are for simulations in the inertial frame. However, these equations would not change in a non-inertial frame, only the velocity would do so.

Effects of the corotation frame. `StarSmasher` can model binary systems in the corotation frame. The way to do it is to place the two stars far enough apart that the tidal effects between the two stars are not really important. The rule of thumb is that the initial separation in the *scan* process should be more than about 3 times the radius of the donor star. Once, the scan process starts the two stars relax with this initial orbital separation (which defines the initial orbital period and angular velocity, ω). Once a relaxation is achieved, the two stars can be slowly brought together in order to find the right time-step that we want to model, which, in general, is when the donor star fills its Roche lobe. We point out that in the scan process only the centrifugal force is taken into account. Once we have a Roche-lobe-overflowing binary we start the dynamical case, which adds up the Coriolis force to the particles in the system. At this moment the angular velocity is keep constant along the dynamical evolution of the binary.

Furthermore, the velocity for a fixed observer of the k–particle , $\mathbf{v}_k$, must change as follows,

$$\mathbf{v}_k = \mathbf{v}_{\mathrm{rot},k} + \Omega_k \times \mathbf{r}_k, \tag{A.47}$$

where $\Omega_k = \omega \hat{z}$. We can give the component for the velocity measured by the fixed observer,

$$v_{x,k} = (v_{x,k})_{\mathrm{rot}} - \omega y, \tag{A.48}$$

$$v_{y,k} = (v_{y,k})_{\mathrm{rot}} + \omega x, \tag{A.49}$$

$$v_{z,k} = (v_{z,k})_{\mathrm{rot}}. \tag{A.50}$$

Hence, the x and y components of the velocity in the equations (A.42), (A.45), and (A.46) have to be replaced by the previous ones.

Note about the orbital energy and orbital angular momentum in the corotation frame. The orbital energy can be calculated by using equation (4.4). However, we point out that the total kinetic energy is split in two contributions, $E_{\mathrm{kin}} = E_{\mathrm{kin,orb}} + E_{\mathrm{kin,spin}}$, where $E_{\mathrm{kin,orb}} = 0.5\mu|\mathbf{V}_{12}|$ is the orbital kinetic energy [see equation (4.4)] and $E_{\mathrm{kin,spin}} = 0.5\omega(I_1 + I_2)$ is the spin kinetic energy, where I_1 and I_2 are the moments of inertia for the star 1 and star 2. The spin kinetic energy is a kind of

internal energy, therefore, we add this energy to the internal energy. We note that the calculation in the inertial frame has $E_{\rm kin,spin} = 0$ and $E_{\rm kin} = E_{\rm kin,orb}$.

Furthermore, the total angular momentum is split into the orbital angular momentum and spin angular momentum of the stars, $\mathbf{L} = \mathbf{J}_{\rm orb} + \mathbf{J}_{\rm spin}$, where $\mathbf{J}_{\rm orb}$ is calculated with equation (4.8), and $\mathbf{J}_{\rm spin} = \omega(I_1 + I_2)\hat{z}$. We note that the x and y components of all angular momenta are zero. We emphasize that $\mathbf{J}_{\rm spin} = 0$ in the calculations in the inertial frame, hence, $\mathbf{L} = \mathbf{J}_{\rm orb}$. Moreover, the z component is the only one that contributes giving $J_{\rm orb} = L_z$ in the inertial frame, and $J_{\rm orb} = L_z - \omega(I_1 + I_2)$, which is equivalent to equation (4.8).

A.4.1 Subroutine for classifying regions of mass

In this Thesis only we used the total energy of each particle (see Equations 3.1, and 3.2), as a way to classify the SPH gas particles in bound or unbound material. Furthermore, we defined three regions:

1. *Ejecta*—the unbound mass of the system, where $E_{{\rm tot},k} \geq 0$.

2. *Circumbinary*—the bound mass to the binary, where $E_{{\rm tot},k} < 0$, but the SPH gas particles are outside of the Roche lobe equipotential.

3. *Binary*—the bound mass to the binary, where $E_{{\rm tot},k} < 0$, but the SPH gas particles are within the Roche lobe equipotential.

As noted before, `StarSmasher` solves for some dynamical quantities, hence, it is straightforward to find the total energy for each particle (see Equations 3.1, and 3.2). However, the problem lies in how to find, or at least estimate, the Roche lobe since we need to know the mass for each star, and once the dynamical calculation starts we cannot longer use the initial classification for star 1 and star 2, but at the beginning of the simulation we can assume that the mass does not change to much, and since the red giant core mass is comparable with the companion mass, for all our simulated cases, we follow the below algorithm:

1. Use the energy criterion, Equation 3.1 or 3.2, in order to test if a particle belongs to unbound mass or bound mass, and tag it as *ejecta*, or *binary*, respectively.

2. Find the core of the two stars, $m_{\rm c,1}$ and $m_{\rm c,2}$; for a main-sequence star companion, we assume that the star does not change its structure until it mergers with the red giant core.

3. Calculate the centre of mass of the bound mass by using $\mathbf{r}_{\rm b} = (\sum_{\rm bound} m_k \mathbf{r}_k)/m_{\rm b}$, where $m_{\rm b} = \sum_{\rm bound} m_k$.

4. Assume that the core of the two stars are the physical location of the centres of mass for the corresponding star, and find the orbital separation using $a_{\rm orb} = |\mathbf{r}_1 - \mathbf{r}_2|$, where $\mathbf{r}_1$ and $\mathbf{r}_2$ are the centre of mass of star 1 and star 2, respectively.

5. Test if $|\mathbf{r}_k - \mathbf{r}_{\rm b}| < a_{\rm orb}$ for the particles in the *binary* region. Otherwise, these particles are tagged as *circumbinary*.

6. Find the distance between the core of each star with respect to each particle $r_{1,k} = |\mathbf{r}_k - \mathbf{r}_1|$, and $r_{2,k} = |\mathbf{r}_k - \mathbf{r}_1|$; Compare the potential energy for each particle with respect to each star core, if $m_{{\rm c},1}/r_{1,k} > m_{{\rm c},2}/r_{2,k}$, then the particle belongs to *star 1*, otherwise, to *star 2*. Note that *binary* region has been split in 2: (i) *star 1*, and (ii) *star 2*. Therefore, we end up with four tags: (1) *star 1*—m_1, (2) *star 2*—m_2, (3) *circumbinary*—$m_{\rm circ}$, and (4) *ejecta*—$m_{\rm unb}$.

7. Use the estimated masses, m_1 and m_2, along with $a_{\rm orb}$ to find L_1 and Roche lobe potential, $\Phi_{\rm rl}$. Use L_1 to estimate a perfect sphere for each star, and reclassify the regions, use the energy criterion, Equation 3.1 or 3.2, to get the unbound material. Check that the total mechanical energy, Equation 3.2, of each particle in *star 1* and *star 2* be less than $\Phi_{\rm rl}$, otherwise, it belongs to *circumbinary*.

A.4.2 Subroutine to get orbital parameters

Once we have the particles that belong to *star 1* and *star 2*, we can estimate the orbital parameters such as, eccentricity e, orbital period $P_{\rm orb}$, orbital energy $E_{\rm orb}$, and orbital angular momentum $J_{\rm orb}$.

The orbital period is calculated with Kepler's third law,

$$P_{\rm orb} = \sqrt{\frac{4\pi^2 a_{\rm orb}^3}{GM}}, \tag{A.51}$$

where $M = m_1 + m_2$, and G is the gravitational constant. The orbital angular momentum is calculated as follows (see Equation 4.8):

$$\mathbf{J}_{\rm orb} \equiv \mu \mathbf{R}_{12} \times \mathbf{V}_{12}, \tag{A.52}$$

where $\mu = m_1 m_2/M$, $\mathbf{R}_{12} = \mathbf{r}_1 - \mathbf{r}_2$, and $\mathbf{V}_{12} = \mathbf{V}_1 - \mathbf{V}_2$, where $\mathbf{V}_1$, and $\mathbf{V}_2$ are the velocity of core of star 1 and star 2, respectively.

The orbital energy can be estimated as follows:

1. Calculate the self-potential energy, separately, for all the particles in star 1 Φ_1, and star 2 Φ_2 by using Equation (A.16).

2. Calculate the total potential energy for all the particles in star 1 and star 2 together—$\Phi_{\rm tot}$ by means of Equation (A.16).

3. Get the orbital potential energy, $E_{\rm orb,pot} = \Phi_{\rm tot} - \Phi_1 - \Phi_2$.

4. Estimate the orbital kinetic energy, $E_{\rm orb,kin} = 0.5\mu|\mathbf{V}_{12}|^2$.

5. Sum the orbital potential and kinetic energies, $E_{\rm orb} = E_{\rm orb,kin} + E_{\rm orb,pot}$.

The eccentricity at the end of the simulation, if any, of the binary is estimated with the periastron r_p (shortest orbital separation) and apastron r_a (longest orbital separation), hence,

$$e = \frac{r_a - r_p}{r_a + r_p}. \tag{A.53}$$

A.5 Animation of binary interactions

Once we have defined the initial conditions, we can start our dynamical calculation by placing the two desired stars in a binary configuration (see Chapter 3 and 4, or Section 2.3 of Lombardi et al., 2011).

Animations for the dynamical evolution of Chapter 2 can be found in:

1. Column densities in simulation ps334, as viewed perpendicular to the orbital plane and at times after the merger. The merger causes an outflow of material, with the field of ejecta dropping to lower and lower densities and column densities as it expands. At late times in the simulation, while the ejecta continues streaming outward, the bound merger product in the center of the system gradually reaches larger column densities as more material falls back to its surface. Visualizations generated using SPLASH (Price, 2007). Link for animation

2. Temperature cross section in the orbital plane. Like visualization S1, the scenario depicted is for simulation ps334, again viewed perpendicular to the orbital plane at times after the merger. Only temperatures between 4000 K and 5000 K are shown, corresponding roughly to the recombination temperature and hence roughly to the location of the photosphere. Note that between $\sim$165 and 185 days, lines of sight from an observer looking along the orbital plane do not fully penetrate down to the innermost closed 4500 K surface: this enlarged photosphere is the main cause of the a plateau phase. Near $\sim$185 days, the shroud dissipates and the inner bound merger product would be revealed, corresponding to the decline stage after the plateau. Visualizations generated using SPLASH (Price, 2007). Link for animation

Animations for the dynamical interaction between a red subgiant star and a main-sequence or degenerate companion star can be found in:

1. Column density animation showing the merger of a non-synchronized binary containing a $M = 1.52 M_\odot$, $R = 3.51 R_\odot$ giant and a $M = 0.16 M_\odot$ degenerate companion with an initial orbital period of 1.42 days. Link for simulation pn351

2. Column density animation showing the merger of a synchronized binary containing a $M = 1.52 M_\odot$, $R = 3.76 R_\odot$ giant and a $M = 0.16 M_\odot$ main-sequence companion with an initial orbital period of 1.50 days. Link for simulation ms376.

Animations for the dynamical interaction between a red giant star and a white dwarf star can be found in:

1. This simulation models the formation of WD 1101+364, assuming that the progenitor binary was composed of a $1.6 M_\odot$ RG and a $0.36 M_\odot$ WD with an initial orbital period of 29.76 days, and the stars were not synchronized with the orbit. The newly formed binary is composed of 0.32 $M_\odot$ WD and 0.36 $M_\odot$ WD with an orbital period of 0.122 days. This movies shows a cross-sectional slice at $z = 0$ in the equatorial plane. The colours are for density, the whiter the denser, and the redder the less dense. Link for animation

2. This simulation models the formation of WD 1101+364, assuming that the progenitor binary was composed of a $1.6 M_\odot$ RG and a $0.36 M_\odot$ WD with an initial orbital period of 29.76 days, and the stars were not synchronized with the orbit. The newly formed binary is composed of 0.32 $M_\odot$ WD and 0.36 $M_\odot$ WD with an orbital period of 0.122 days. This movies shows a cross-sectional slice at $z = 0$ in the equatorial plane for the expanding circumbinary region. The colours are for density, the whiter the denser, and the redder the less dense. Link for animation

3. This simulation models the formation of WD 1101+364, assuming that the progenitor binary was composed of a $1.6 M_\odot$ RG and a $0.36 M_\odot$ WD with an initial orbital period of 27.97 days, and the stars were synchronized with the orbit. The newly formed binary is composed of 0.32 $M_\odot$ WD and 0.36 $M_\odot$ WD with an orbital period of 0.122 days. This movies shows a cross-sectional slice at $z = 0$. The colours are for density, the whiter the denser, and the redder the less dense. Link for animation

4. This simulation models the formation of WD 1101+364, assuming that the progenitor binary was composed of a $1.6 M_\odot$ RG and a $0.36 M_\odot$ WD with an initial orbital period of 27.97

days, and the stars were synchronized with the orbit. The newly formed binary is composed of 0.32 $M_\odot$ WD and 0.36 $M_\odot$ WD with an orbital period of 0.122 days. This movies shows a cross-sectional slice at $y = 0$ in the xz plane. The colours are for density, the whiter the denser, and the redder the less dense. Link for animation

5. This simulation models the formation of WD 1101+364, assuming that the progenitor binary was composed of a $1.6 M_\odot$ RG and a $0.36 M_\odot$ WD with an initial orbital period of 27.97 days, and the stars were synchronized with the orbit. The newly formed binary is composed of 0.32 $M_\odot$ WD and 0.36 $M_\odot$ WD with an orbital period of 0.122 days. This movies shows a cross-sectional slice at $y = 0$ in the xz plane for the expanding circumbinary region. The colours are for density, the whiter the denser, and the redder the less dense. Link for animation

References

Alexander, M. E. 1973, Ap&SS, 23, 459

Antonini, F., Lombardi, Jr., J. C., & Merritt, D. 2011, ApJ, 731, 128

Balsara, D. S. 1995, Journal of Computational Physics, 121, 357

Bear, E., Kashi, A., & Soker, N. 2011, MNRAS, 416, 1965

Berger, E., Soderberg, A. M., Chevalier, R. A., Fransson, C., Foley, R. J., Leonard, D. C., Debes, J. H., Diamond-Stanic, A. M., Dupree, A. K., Ivans, I. I., Simmerer, J., Thompson, I. B., & Tremonti, C. A. 2009, ApJ, 699, 1850

Bethe, H. 1964, Los Alamos Report, 44

Bisnovatyi-Kogan, G. S. 2001, Stellar physics. Vol.1: Fundamental concepts and stellar equilibrium (Springer)

Bond, H. E. 2011, ApJ, 737, 17

Bond, H. E., Bedin, L. R., Bonanos, A. Z., Humphreys, R. M., Monard, L. A. G. B., Prieto, J. L., & Walter, F. M. 2009, ApJ, 695, L154

Bond, H. E., Henden, A., Levay, Z. G., Panagia, N., Sparks, W. B., Starrfield, S., Wagner, R. M., Corradi, R. L. M., & Munari, U. 2003, Nature, 422, 405

Bond, H. E., Humphreys, R. M., Bedin, L. R., Bonanos, A., Davidson, K., Monard, B., Prieto, J., & Walter, F. 2012, in American Astronomical Society Meeting Abstracts, Vol. 219, American Astronomical Society Meeting Abstracts, 436.09

Boschi, F. & Munari, U. 2004, A&A, 418, 869

Boyarchuk, A. A., Bisikalo, D. V., Kuznetsov, O. A., & Chechetkin, V. M. 2002, Mass transfer in close binary stars

Chiavassa, A., Pasquato, E., Jorissen, A., Sacuto, S., Babusiaux, C., Freytag, B., Ludwig, H.-G., Cruzalèbes, P., Rabbia, Y., Spang, A., & Chesneau, O. 2011, A&A, 528, A120

Chomiuk, L. & Povich, M. S. 2011, AJ, 142, 197

Chugai, N. N. 1991, Soviet Astronomy Letters, 17, 210

Crause, L. A., Lawson, W. A., Kilkenny, D., van Wyk, F., Marang, F., & Jones, A. F. 2003, MNRAS, 341, 785

Darwin, G. H. 1879, Royal Society of London Proceedings Series I, 29, 168

de Kool, M. 1990, ApJ, 358, 189

Duquennoy, A. & Mayor, M. 1991, A&A, 248, 485

Eastman, R. G., Woosley, S. E., Weaver, T. A., & Pinto, P. A. 1994, ApJ, 430, 300

Eggleton, P. 2006, Evolutionary Processes in Binary and Multiple Stars

Eggleton, P. P. 1971, MNRAS, 151, 351

—. 1972, MNRAS, 156, 361

—. 1973, MNRAS, 163, 279

—. 1983, ApJ, 268, 368

—. 2012, Journal of Astronomy and Space Sciences, 29, 145

Eggleton, P. P., Faulkner, J., & Flannery, B. P. 1973, A&A, 23, 325

Eggleton, P. P. & Kiseleva-Eggleton, L. 2001, ApJ, 562, 1012

Gaburov, E., Lombardi, Jr., J. C., & Portegies Zwart, S. 2010, MNRAS, 402, 105

Gingold, R. A. & Monaghan, J. J. 1977, MNRAS, 181, 375

Glebbeek, E., Pols, O. R., & Hurley, J. R. 2008, A&A, 488, 1007

Grasberg, E. K. & Nadezhin, D. K. 1976, Ap&SS, 44, 409

Grassberg, E. K., Imshennik, V. S., & Nadyozhin, D. K. 1971, Ap&SS, 10, 28

Han, Z., Podsiadlowski, P., & Eggleton, P. P. 1994, MNRAS, 270, 121

Han, Z., Podsiadlowski, P., Maxted, P. F. L., Marsh, T. R., & Ivanova, N. 2002, MNRAS, 336, 449

Heger, A., Langer, N., & Woosley, S. E. 2000, ApJ, 528, 368

Hernquist, L. & Katz, N. 1989, ApJS, 70, 419

Herschel, W. 1802, Philosophical Transactions of the Royal Society of London, 92, 477

Hurley, J. R., Pols, O. R., & Tout, C. A. 2000, MNRAS, 315, 543

Hut, P. 1980, A&A, 92, 167

—. 1981, A&A, 99, 126

Iben, Jr., I. & Livio, M. 1993, PASP, 105, 1373

Iben, Jr., I. & Tutukov, A. V. 1992, ApJ, 389, 369

Imshenik, V. S. & Nadezhin, D. K. 1965, Soviet Ast., 8, 664

Ivanova, N. 2011, in Astron. Soc. Pac. Conf. Ser., Vol. 447, Evolution of Compact Binaries, ed. L. Schmidtobreick, M. R. Schreiber, & C. Tappert, 91

Ivanova, N., Justham, S., Avendano Nandez, J. L., & Lombardi, J. C. 2013a, Science, 339, 433

Ivanova, N., Justham, S., Chen, X., De Marco, O., Fryer, C. L., Gaburov, E., Ge, H., Glebbeek, E., Han, Z., Li, X.-D., Lu, G., Marsh, T., Podsiadlowski, P., Potter, A., Soker, N., Taam, R., Tauris, T. M., van den Heuvel, E. P. J., & Webbink, R. F. 2013b, A&A Rev., 21, 59

Ivanova, N. & Podsiadlowski, P. 2002, in Astronomical Society of the Pacific Conference Series, Vol. 279, Exotic Stars as Challenges to Evolution, ed. C. A. Tout & W. van Hamme, 245

Ivanova, N., Rasio, F. A., Lombardi, Jr., J. C., Dooley, K. L., & Proulx, Z. F. 2005, ApJ, 621, L109

Kasen, D. & Ramirez-Ruiz, E. 2010, ApJ, 714, 155

Kasen, D. & Woosley, S. E. 2009, ApJ, 703, 2205

Kasliwal, M. M., Kulkarni, S. R., Arcavi, I., Quimby, R. M., Ofek, E. O., Nugent, P., Jacobsen, J., Gal-Yam, A., Green, Y., Yaron, O., Fox, D. B., Howell, J. L., Cenko, S. B., Kleiser, I., Bloom, J. S., Miller, A., Li, W., Filippenko, A. V., Starr, D., Poznanski, D., Law, N. M., Helou, G., Frail, D. A., Neill, J. D., Forster, K., Martin, D. C., Tendulkar, S. P., Gehrels, N., Kennea, J., Sullivan, M., Bildsten, L., Dekany, R., Rahmer, G., Hale, D., Smith, R., Zolkower, J., Velur, V., Walters, R., Henning, J., Bui, K., McKenna, D., & Blake, C. 2011, ApJ, 730, 134

Kimeswenger, S., Lederle, C., Schmeja, S., & Armsdorfer, B. 2002, MNRAS, 336, L43

Kippenhahn, R. 1969, A&A, 2, 309

Kochanek, C. S. 2011, ApJ, 741, 37

Kochanek, C. S., Szczygieł, D. M., & Stanek, K. Z. 2012, ApJ, 758, 142

Kopal, Z. 1955, Annales d'Astrophysique, 18, 379

Kroupa, P. 2002, Science, 295, 82

Kuiper, G. P. 1941, ApJ, 93, 133

Kulkarni, S. R., Ofek, E. O., Rau, A., Cenko, S. B., Soderberg, A. M., Fox, D. B., Gal-Yam, A., Capak, P. L., Moon, D. S., Li, W., Filippenko, A. V., Egami, E., Kartaltepe, J., & Sanders, D. B. 2007, Nature, 447, 458

Lai, D., Rasio, F. A., & Shapiro, S. L. 1993, ApJS, 88, 205

Litvinova, I. Y. & Nadezhin, D. K. 1985, Soviet Astronomy Letters, 11, 145

Livio, M. & Soker, N. 1988, ApJ, 329, 764

Lombardi, J. C., Sills, A., Rasio, F. A., & Shapiro, S. L. 1999, Journal of Computational Physics, 152, 687

Lombardi, Jr., J. C., Holtzman, W., Dooley, K. L., Gearity, K., Kalogera, V., & Rasio, F. A. 2011, ApJ, 737, 49

Lombardi, Jr., J. C., Proulx, Z. F., Dooley, K. L., Theriault, E. M., Ivanova, N., & Rasio, F. A. 2006, ApJ, 640, 441

Loveridge, A. J., van der Sluys, M. V., & Kalogera, V. 2011, ApJ, 743, 49

Lucy, L. B. 1967, AJ, 72, 813

—. 1977, ApJ, 82, 1013

Marsh, T. R. 1995, MNRAS, 275, L1

Martin, E. L., Spruit, H. C., & Tata, R. 2011, A&A, 535, A50

Martini, P., Wagner, R. M., Tomaney, A., Rich, R. M., della Valle, M., & Hauschildt, P. H. 1999, AJ, 118, 1034

Mason, E., Diaz, M., Williams, R. E., Preston, G., & Bensby, T. 2010, A&A, 516, A108

Meyer, F. & Meyer-Hofmeister, E. 1979, A&A, 78, 167

Monaghan, J. J. 1992, ARA&A, 30, 543

—. 1997, Journal of Computational Physics, 136, 298

Monaghan, J. J. & Lattanzio, J. C. 1985, A&A, 149, 135

Mould, J., Cohen, J., Graham, J. R., Hamilton, D., Matthews, K., Picard, A., Reid, N., Schmidt, M., Soifer, T., Wilson, C., Rich, R. M., & Gunn, J. 1990, ApJ, 353, L35

Munari, U., Corradi, R. L. M., Henden, A., Navasardyan, H., Valentini, M., Greimel, R., Leisy, P., Augusteijn, T., Djupvik, A. A., Glowienka, L., Somero, A., de La Rosa, I. G., Vazdekis, A., Kolka, I., & Liimets, T. 2007, A&A, 474, 585

Nandez, J. L. A., Ivanova, N., & J. C. Lombardi, J. 2014, The Astrophysical Journal, 786, 39

Nelemans, G. & Tout, C. A. 2005, MNRAS, 356, 753

Nelemans, G., Verbunt, F., Yungelson, L. R., & Portegies Zwart, S. F. 2000, A&A, 360, 1011

Nicholls, C. P., Melis, C., Soszyński, I., Udalski, A., Szymański, M. K., Kubiak, M., Pietrzyński, G., Poleski, R., Ulaczyk, K., Wyrzykowski, Ł., Kozłowski, S., & Pietrukowicz, P. 2013, MNRAS, 431, L33

Ofek, E. O., Kulkarni, S. R., Rau, A., Cenko, S. B., Peng, E. W., Blakeslee, J. P., Côté, P., Ferrarese, L., Jordán, A., Mei, S., Puzia, T., Bradley, L. D., Magee, D., & Bouwens, R. 2008, ApJ, 674, 447

Paczynski, B. 1976, in IAU Symposium, Vol. 73, Structure and Evolution of Close Binary Systems, ed. P. Eggleton, S. Mitton, & J. Whelan, 75

Paczyński, B. & Ziółkowski, J. 1967, Acta Astron., 17, 7

—. 1968, Acta Astron., 18, 255

Passy, J.-C., De Marco, O., Fryer, C. L., Herwig, F., Diehl, S., Oishi, J. S., Mac Low, M.-M., Bryan, G. L., & Rockefeller, G. 2012, ApJ, 744, 52

Pastorello, A., Della Valle, M., Smartt, S. J., Zampieri, L., Benetti, S., Cappellaro, E., Mazzali, P. A., Patat, F., Spiro, S., Turatto, M., & Valenti, S. 2007, Nature, 449, 1

Paxton, B., Bildsten, L., Dotter, A., Herwig, F., Lesaffre, P., & Timmes, F. 2011, ApJS, 192, 3

Pejcha, O. 2013, ArXiv e-prints

Podsiadlowski, P. 2001, in Astronomical Society of the Pacific Conference Series, Vol. 229, Evolution of Binary and Multiple Star Systems, ed. P. Podsiadlowski, S. Rappaport, A. R. King, F. D'Antona, & L. Burderi, 239

Podsiadlowski, P. 2010, NewAR, 54, 39

Politano, M., van der Sluys, M., Taam, R. E., & Willems, B. 2010, ApJ, 720, 1752

Pols, O. R., Tout, C. A., Eggleton, P. P., & Han, Z. 1995, MNRAS, 274, 964

Popov, D. V. 1993, ApJ, 414, 712

Price, D. J. 2007, Publ. Astron. Soc. Aust., 24, 159

Prieto, J. L., Kistler, M. D., Thompson, T. A., Yüksel, H., Kochanek, C. S., Stanek, K. Z., Beacom, J. F., Martini, P., Pasquali, A., & Bechtold, J. 2008, ApJ, 681, L9

Rasio, F. A. 1991, PhD Thesis, Cornell University

Rau, A., Kulkarni, S. R., Law, N. M., Bloom, J. S., Ciardi, D., Djorgovski, G. S., Fox, D. B., Gal-Yam, A., Grillmair, C. C., Kasliwal, M. M., Nugent, P. E., Ofek, E. O., Quimby, R. M., Reach, W. T., Shara, M., Bildsten, L., Cenko, S. B., Drake, A. J., Filippenko, A. V., Helfand, D. J., Helou, G., Howell, D. A., Poznanski, D., & Sullivan, M. 2009, PASP, 121, 1334

Rau, A., Kulkarni, S. R., Ofek, E. O., & Yan, L. 2007, ApJ, 659, 1536

Renvoizé, V., Baraffe, I., Kolb, U., & Ritter, H. 2002, A&A, 389, 485

Rest, A., Prieto, J. L., Walborn, N. R., Smith, N., Bianco, F. B., Chornock, R., Welch, D. L., Howell, D. A., Huber, M. E., Foley, R. J., Fong, W., Sinnott, B., Bond, H. E., Smith, R. C., Toledo, I., Minniti, D., & Mandel, K. 2012, Nature, 482, 375

Retter, A. & Marom, A. 2003, MNRAS, 345, L25

Ricker, P. M. & Taam, R. E. 2012, ApJ, 746, 74

Rosswog, S. 2009, NewAR, 53, 78

Roxburgh, I. W. 1967, Nature, 215, 838

Sana, H., de Mink, S. E., de Koter, A., Langer, N., Evans, C. J., Gieles, M., Gosset, E., Izzard, R. G., Le Bouquin, J.-B., & Schneider, F. R. N. 2012, Science, 337, 444

Siegel, M. H. & Bond, H. E. 2007, in Astronomical Society of the Pacific Conference Series, Vol. 363, The Nature of V838 Mon and its Light Echo, ed. R. L. M. Corradi & U. Munari, 189

Smith, N., Ganeshalingam, M., Chornock, R., Filippenko, A. V., Li, W., Silverman, J. M., Steele, T. N., Griffith, C. V., Joubert, N., Lee, N. Y., Lowe, T. B., Mobberley, M. P., & Winslow, D. M. 2009, ApJ, 697, L49

Soberman, G. E., Phinney, E. S., & van den Heuvel, E. P. J. 1997, A&A, 327, 620

Soker, N. & Kashi, A. 2012, ApJ, 746, 100

Soker, N. & Tylenda, R. 2003, ApJ, 582, L105

—. 2006, MNRAS, 373, 733

—. 2007, MNRAS, 375, 909

Stępień, K. 2011, A&A, 531, A18

Thompson, T. A., Prieto, J. L., Stanek, K. Z., Kistler, M. D., Beacom, J. F., & Kochanek, C. S. 2009, ApJ, 705, 1364

Tylenda, R. 2005, A&A, 436, 1009

Tylenda, R., Crause, L. A., Górny, S. K., & Schmidt, M. R. 2005a, A&A, 439, 651

Tylenda, R., Hajduk, M., Kamiński, T., Udalski, A., Soszyński, I., Szymański, M. K., Kubiak, M., Pietrzyński, G., Poleski, R., Wyrzykowski, Ł., & Ulaczyk, K. 2011, A&A, 528, A114

Tylenda, R. & Soker, N. 2006, A&A, 451, 223

Tylenda, R., Soker, N., & Szczerba, R. 2005b, A&A, 441, 1099

Udalski, A. 2003, Acta Astron., 53, 291

Webbink, R. F. 1975, PhD thesis, University of Cambridge

—. 1976, ApJ, 209, 829

—. 1977, ApJ, 211, 881

—. 1984, ApJ, 277, 355

Webbink, R. F. 2008, in Astrophysics and Space Science Library, Vol. 352, Astrophysics and Space Science Library, ed. E. F. Milone, D. A. Leahy, & D. W. Hobill, 233

Wisniewski, J. P., Morrison, N. D., Bjorkman, K. S., Miroshnichenko, A. S., Gault, A. C., Hoffman, J. L., Meade, M. R., & Nett, J. M. 2003, ApJ, 588, 486

Woods, T. E., Ivanova, N., van der Sluys, M., & Chaichenets, S. 2011, in Astronomical Society of the Pacific Conference Series, Vol. 447, Evolution of Compact Binaries, ed. L. Schmidtobreick, M. R. Schreiber, & C. Tappert, 127

Zahn, J.-P. 1977, A&A, 57, 383

Zel'Dovich, Y. B., Kompaneets, Y. B., & Raizer, Y. P. 1958a, JETP, 7, 882

—. 1958b, JETP, 7, 1001